Beam-spin asymmetry of deeply virtual Compton scattering off the proton at 10.6 GeV with CLAS12 at Jefferson Laboratory

Guillaume Christiaens

Submitted in fulfilment of the requirements for the
Degree of Doctor of Philosophy

School of Physics and Astronomy
College of Science and Engineering
University of Glasgow

February 2021

Abstract

This thesis presents the measurements of beam-spin asymmetry (BSA) of deeply virtual Compton scattering (DVCS) off the proton at 10.6 GeV with the CLAS12 spectrometer at Jefferson Laboratory. This data will provide, in the valence region, high energy DVCS measurements, to help constrain nucleon structure physics models.

The data used in this thesis was taken at Jefferson Laboratory (Virginia, USA). The CLAS12 spectrometer, installed in the experimental hall B, receives a longitudinally polarized electron beam accelerated to up to 10.6 GeV. CLAS12 provides the identification and reconstruction of the particles obtained from the interaction of the electron beam with a fixed liquid hydrogen target.

Micromegas detectors were used to improve the tracking resolution within the CLAS12 spectrometer. This thesis provides a description of the assembly, integration and operation of Micromegas detectors. The integration of the Micromegas detectors with the other CLAS12 subsystems, the integration of the gas and software systems as well as tests and studies performed during the commissioning are detailed.

In this thesis, the DVCS process was extracted from the data collected by CLAS12 and the BSA was computed. The emphasis was put on the exclusive selection of DVCS signal and the estimation of the π^0 electroproduction background. The DVCS exclusivity variables and the positions of the exclusivity cuts were optimised to reduce the π^0 electroproduction background and the remaining contamination was estimated from a Monte-Carlo simulation. The BSA was extracted for 240 kinematic bins with: ten ϕ bins, four t bins, three x_B bins and two Q^2 bins.

Contents

List of Tables

List of Figures

Acknowledgements

First and foremost, I would like to express my gratitude to my supervisors, Daria Sokhan and Maxime Defurne. I cannot thank them enough for their constant encouragement, their valuable advice and their extraordinary patience. It has been a sincere pleasure to spend time with them over the last few years.

I would like to give a special thank to Franck Sabatié and Dave Ireland, for making this thesis possible, as well as for their unconditional trust and support. They both deserve my profound gratitude.

I am obliged to all the physicists, engineers and technicians from CEA Saclay, the University of Glasgow, Jefferson Laboratory and the CLAS collaboration, who have expressed their support. A particular thanks goes to Francesco Bossú, his sharp advice was precious, and to Derek Glazier, Bryan McKinnon, Ken Livingston and Hervé Moutarde. I am obliged to all the CEA Saclay Micromegas team, they taught me so much about detectors and so many other things.

I would also like to thank all the other students, from the University of Glasgow, CEA Saclay and the students I met at Jefferson Laboratory. Noëlie Cherrier deserves a special acknowledgement, I would have liked to be able to go further in our collaboration during this thesis.

I acknowledge CEA Saclay and the University of Glasgow for funding this research and all the non-scientist support staff, from all the institutions, who made this work possible.

Finally, I would like to thank my family and friends who have consistently been there, over the years, when I needed them.

To everyone who has been willing to help, thank you.

Declaration

I declare that, except where explicit reference is made to the contribution of others, the material presented in this thesis is the result of my own work. No part of this thesis has been submitted for any other degree at the University of Glasgow or any other institution.

Introduction

The standard model of particle physics has been very successfully describing the electromagnetic, weak and strong interactions. The Higgs boson, discovered in 2012, was one of the last missing pieces of the standard model to explain the generation of mass. Despite its success, the standard model, in its current form, is not able to describe all physical phenomena (for instance gravity) and, even inside the standard model, some of the elements, such as the theory of quantum chromodynamics (QCD), are not fully understood yet.

QCD is the field theory that describes the strong interactions of quarks and gluons within the standard model. The fundamental parameter of QCD is the strong coupling constant α_S, and its behaviour is perhaps the most striking difference between QCD and the other field theories of the standard model. At high energy, the strong coupling constant is small, the quarks tend to behave like free particles and QCD becomes perturbative: this property is called "asymptotic freedom". On the contrary, at low energy, the strong coupling constant is large, QCD becomes non-perturbative and the quarks are confined into colourless hadrons. While the mass of the quarks (a few $\mathrm{MeV/c^2}$) is generated by the Higgs boson, the mass of the proton ($938\,\mathrm{MeV/c^2}$) is largely due to the interactions of the quarks and gluons, confined inside the nucleon.

The existence of the proton was proved by Rutherford in 1919 [1]. Following experiments showed that the proton could not be a pointlike particle but was a composite object, its constituents being called partons. The study of these partons, now identified as the quarks and gluons of QCD, and how the properties of the proton emerge from its constituents have been important topics of research in the last sixty years and are still among the great questions of modern nuclear and particle physics.

Lepton scattering experiments provide a unique tool to study the structure of protons. In particular, the analysis of deep exclusive processes, such as deeply virtual Compton scattering (DVCS), have given access to a new kind of distributions called generalized parton distributions (GPDs). GPDs encapsulate the non-perturbative QCD part of the DVCS reaction and describe the correlations between longitudinal momentum and transverse position of the quarks and gluons confined in the nucleon. GPDs provide access to a three-dimensional tomographic reconstruction of the proton structure and can also be used to extract the contribution of quark orbital angular momentum to the proton spin

This thesis is organised as follows:

- Chapter 1 provides an overview of the study of nucleon structure. The theoretical framework of GPDs is explained and the use of the DVCS reaction to study GPDs is described.
- Chapter 2 focuses on the experimental setup used in this thesis. The hall B and CLAS12 spectrometer at Jefferson Laboratory are detailed, with the emphasis given to the detectors that are used in the data analysis: drift chambers, silicon and Micromegas detectors, Cherenkov detectors, time-of-flight detectors and calorimeters.
- Chapter 3 is dedicated to the description of the Micromegas detectors, which were part of the CLAS12 spectrometer for the experiment analysed in this thesis. The integration, commissioning and operation of Micromegas detectors are detailed.
- Chapter 4 provides the details about the analysis of the DVCS reaction and the extraction of the beam-spin asymmetry observable.

The work done during this thesis is described in chapters 3 and 4 with roughly the first half of the work dedicated to the Micromegas detectors (mainly under supervision of CEA Saclay, France) and the second half dedicated to DVCS data analysis (under joint supervision of CEA Saclay and the University of Glasgow, United Kingdom).

Chapter 1

Theoretical motivations

In this chapter, the study of the structure of nucleons using electron scattering is explained. The roles of elastic and inelastic scattering are introduced from a historical point of view. The relevance of generalized parton distributions to further explore the structure of nucleons is highlighted. The deeply virtual Compton scattering process is then defined and its connections to generalized parton distributions are illustrated. Finally the current status of deeply virtual Compton scattering experiments is shown. Unless specified otherwise, this chapter does not describe work done by the author of this thesis.

The notations and conventions used in this thesis are specified in the appendix A.1.

1.1 Nucleon structure from electron scattering experiments

The general idea of performing scattering experiments to study the structure of matter is not new. Rutherford, in 1911, used α particles scattering on a gold foil to understand the structure of atoms, leading to the development of his model of the atom [2]: a dense and tiny nucleus surrounded by a cloud of electrons. The electromagnetic interaction being the best understood, physicists have often used electrons to probe nucleons. This chapter describes how the structure of nucleons is accessed through electron-proton scattering.

The general electron-proton scattering reaction is:

$$e^- + p \rightarrow e^- + X \tag{1.1}$$

where X is any possible final state (including several particles) as shown on figure 1.1. In this reaction, the interaction between the electron and the proton is mainly electromagnetic and to a first approximation, in the kinematic range of this work, the interaction is provided by the exchange of a virtual photon. The following variables are used:

- M_p, mass of the proton
- $l = (E, \vec{l})$, four-momentum of the incident electron in the laboratory frame

- $l' = (E', \vec{l'})$, four-momentum of the scattered electron in the laboratory frame
- $p = (E_p, \vec{p})$, four-momentum of the target proton in the laboratory frame
- θ_e, scattering angle (angle between the incident and scattered electrons in the laboratory frame)
- $q = l - l'$, four-momentum of the virtual photon in the laboratory frame
- $Q^2 = -q^2 = -(l - l')^2$, virtuality of the virtual photon
- $x_B = \frac{Q^2}{2p \cdot q}$, Bjorken variable
- $W^2 = (p + q)^2$, invariant mass squared of the final hadronic system

If the final state X contains a proton (of four-momentum p') the additional variable t is defined as:

- $t = (p - p')^2$

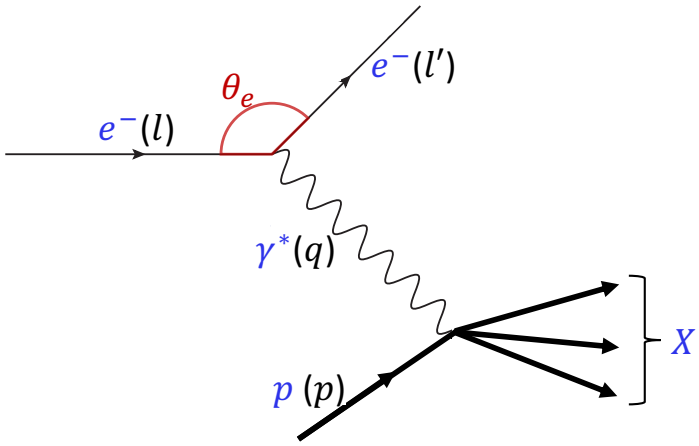

Figure 1.1: General schematic of electron scattering off a proton (with the particles in blue and their four-momenta in black between parentheses).

1.1.1 Elastic scattering and form factors

The study of nucleon structure essentially started in the 1950's at Standford University, with the research group led by Robert Hofstadter. They performed elastic electron scattering experiments on nuclei and then nucleons [3] [4] [5]. Hofstadter was awarded the Nobel Prize of Physics in 1961 for this work.

An electron scatters elastically on a proton if the final state is only composed of the electron and the proton (X is a proton) as shown on figure 1.2.

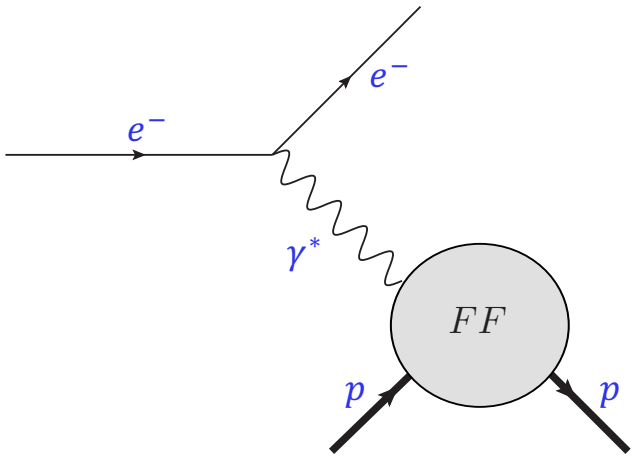

Figure 1.2: Schematic of elastic scattering of an electron off a proton, in the single photon exchange approximation. The structure of the proton is encoded in the form factors (FF).

The differential cross-section in the laboratory frame for elastic scattering, derived by Marshall Rosenbluth in 1950 [6] and sometimes called the Rosenbluth formula, is:

$$\frac{d\sigma}{d\Omega} = \sigma_{Mott}\frac{E}{E'}\left(F_1^2(Q^2) + \tau F_2(Q^2) + \tau\left[F_1(Q^2) + F_2(Q^2)\right]^2 \tan\left(\theta_e/2\right)\right) \tag{1.2}$$

where $\tau = Q^2/4M_p$ and $F_1(Q^2)$ and $F_2(Q^2)$ are the proton electromagnetic form factors (FFs) which encode the effects of proton structure on the elastic scattering process. σ_{Mott} is the Mott differential cross-section, named after Nevill Francis Mott who derived it in 1929, and corresponds to the relativistic scattering of a lepton on an infinitely heavy, pointlike proton:

$$\sigma_{Mott} = \frac{\alpha\cos^2\left(\theta_e/2\right)}{4E^2\sin^4\left(\theta_e/2\right)} \tag{1.3}$$

where α is the electromagnetic fine-structure constant. The form factors F_1 and F_2 are called the Pauli and Dirac form factors to distinguish them from an alternative form factor convention, the Sachs electric and magnetic form factors defined as:

$$G_E = F_1 - \tau F_2 \tag{1.4}$$

$$G_M = F_1 + F_2 \tag{1.5}$$

With the Sachs form factors, equation 1.2 becomes:

$$\frac{d\sigma}{d\Omega} = \sigma_{Mott}\frac{E}{E'}\left(\frac{G_E^2(Q^2) + \tau G_M^2(Q^2)}{1+\tau} + 2\tau G_M^2(Q^2)\tan\left(\theta_e/2\right)\right) \tag{1.6}$$

The form-factors are traditionally obtained with the Rosenbluth separation method, by performing cross-section measurements at different beam energies but a constant value of Q^2. The first cross-section measurements from Hofstadter (with 100 MeV to 550 MeV electron beam) were one of the first indication that the proton does not behave like a pointlike particle, but has a finite size, as shown on figure 1.3, with a charge radius of about 0.7 fm.

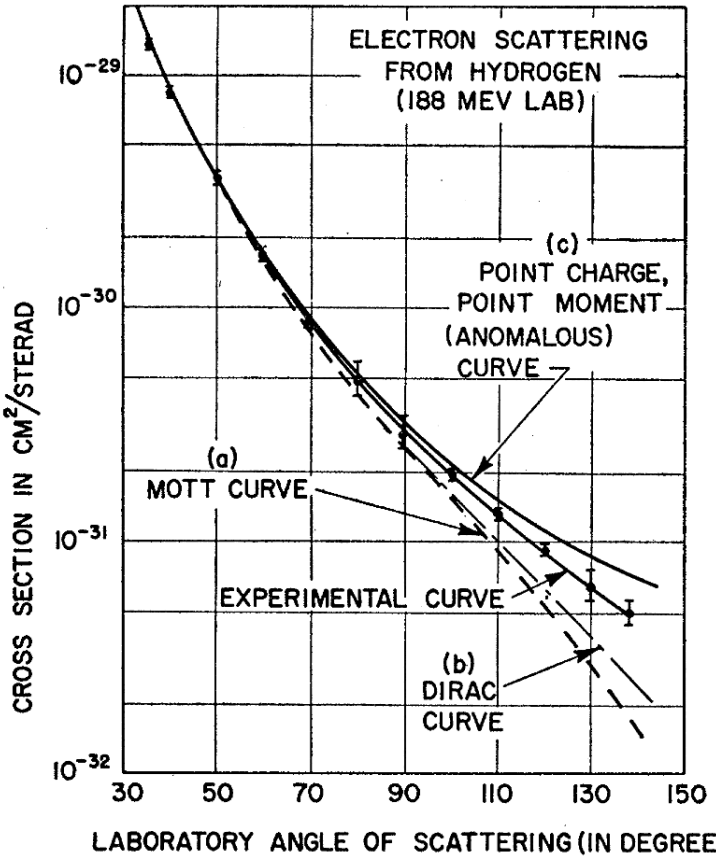

FIG. 5. Curve (a) shows the theoretical Mott curve for a spinless point proton. Curve (b) shows the theoretical curve for a point proton with the Dirac magnetic moment, curve (c) the theoretical curve for a point proton having the anomalous contribution in addition to the Dirac value of magnetic moment. The theoretical curves (b) and (c) are due to Rosenbluth.[8] The experimental curve falls between curves (b) and (c). This deviation from the theoretical curves represents the effect of a form factor for the proton and indicates structure within the proton, or alternatively, a breakdown of the Coulomb law. The best fit indicates a size of 0.70×10^{-13} cm.

Figure 1.3: Original comparison of elastic scattering cross-section data with theoretical calculations [4].

The proton form factors are related to the size of the proton (with relativistic limitations that are briefly discussed in the next paragraph), the proton charge root-mean-square radius is

defined as the slope of the form factors G_E at $Q^2 = 0$:

$$\langle r_e^2 \rangle = -\frac{6}{G_E(0)} \frac{dG_E(Q^2)}{dQ^2}\Big|_{Q^2=0} \tag{1.7}$$

Recent measurements of the proton charge radius from precise electron scattering experiments give $\langle r_e^2 \rangle = 0.831 \pm 0.007_{stat} \pm 0.012_{syst}$ fm [7].

The Breit frame is the frame in which the initial and final proton have the same momentum, but are antiparallel (in this frame there is no energy transfered to the proton). In the Breit frame, the form factors G_E and G_M have a non-relativistic interpretation as the three-dimensional Fourier transform of the electric and magnetic charge distribution, respectively. However, when the probing wavelengh is at least comparable to $1/M_p$, the momentum transfer to the proton is not negligible. In that case, the form factors are not only determined by the internal structure of the nucleon but also contain the dynamics of the recoil, leading to relativistic corrections. In this relativistic case, the proton charge radius defined with the Pauli form factor F_1 and the proton charge radius defined from G_E lead to different results.

Mathias Burkardt showed [8] that relativistic corrections disappear when working in the transverse dimensions of an infinite momentum frame (a frame in which the proton momentum is such that $p_z \to \infty$ and $p_\perp \to 0$). In such frames, the proton has an infinitely large effective mass and no recoil corrections are needed in the transverse plane: the non-relativistic interpretation holds. In an infinite momentum frame, the Dirac form factor F_1 is therefore the two-dimensional Fourier transform of the charge distribution in the transverse plane. The non-relativistic three-dimensional Fourier transform thus becomes a two-dimensional Fourier transform in the transverse plane which includes the relativistic corrections. The connection between the interpretation of the different form factors in different frames is discussed in [9].

1.1.2 Deep inelastic scattering and parton distribution functions

The Stanford Linear Accelerator Center (SLAC) was initially built to extend the study of elastic scattering and quasi-elastic scattering (production of proton resonances), with a beam energy able to reach up to 20 GeV. This new facility made possible the first inelastic scattering experiments, in which the proton may not remain intact in the final state: $ep \to eX$ for any X.

The cross-section for inelastic scattering can be parametrized by inelastic form factors, called structure functions, $W_1(x_B, Q^2)$ and $W_2(x_B, Q^2)$:

$$\frac{d^2\sigma}{d\Omega dE'} = \sigma_{Mott}\left(W_2(x_B, Q^2) + 2W_1(x_B, Q^2)\tan^2(\theta_e/2) \right) \tag{1.8}$$

The first results [10] [11], published in 1969 by a team including Jerome Friedman, Henry Kendall and Richard Taylor, confirmed the expected decrease of the elastic cross-section at large Q^2. Indeed, when the momentum transferred to the proton increases, the probability that

all the energy is absorbed in the proton and it does not break is expected to decrease. The behavior of the inelastic scattering cross-section (see figure 1.4) was found to be very different and did not seem to be vanishing for large Q^2. The deep inelastic region, for large Q^2 and $W \gtrsim 2\,\mathrm{GeV/c^2}$, therefore outside of the proton resonance region, became of interest for both theorists and experimentalists. The inelastic scattering process is called deep inelastic scattering (DIS) when studied in the deep inelastic regime.

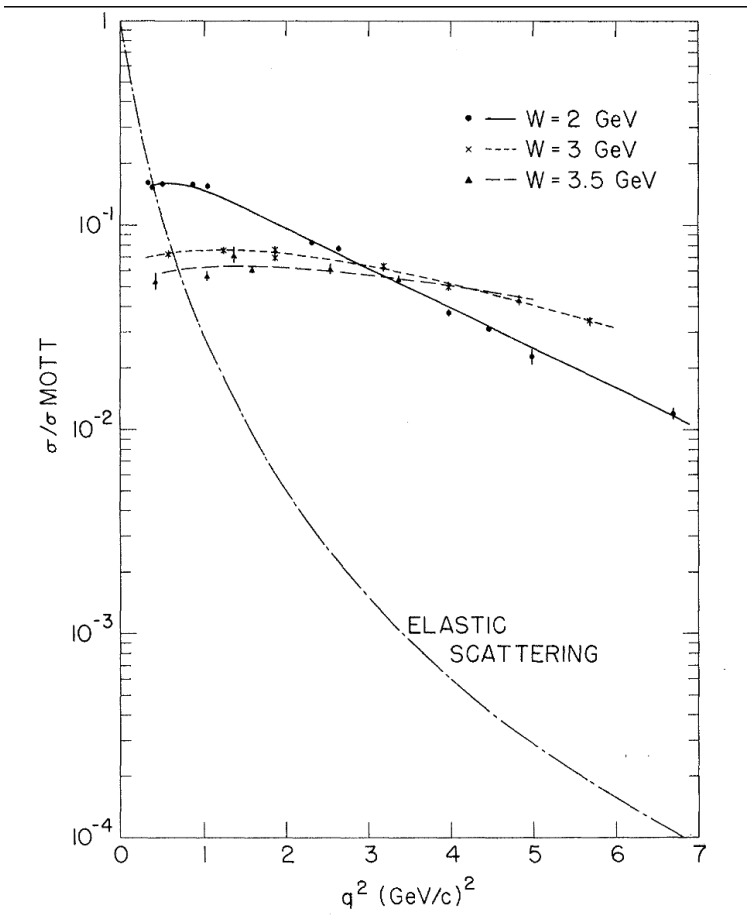

FIG. 1. $(d^2\sigma/d\Omega dE')/\sigma_{\mathrm{Mott}}$, in GeV^{-1}, vs q^2 for W = 2, 3, and 3.5 GeV. The lines drawn through the data are meant to guide the eye. Also shown is the cross section for elastic e-p scattering divided by σ_{Mott}, $(d\sigma/d\Omega)/\sigma_{\mathrm{Mott}}$, calculated for $\theta = 10°$, using the dipole form factor. The relatively slow variation with q^2 of the inelastic cross section compared with the elastic cross section is clearly shown.

Figure 1.4: Original cross-section data from the first inelastic scattering compared to the elastic scattering measurements [11].

James Bjorken had already suggested [12] the possibility, now called "Bjorken scaling", that the DIS structure functions could approach non-zero functions of x_B in the limit $Q^2 \to \infty$ (called the "Bjorken limit"):

$$\lim_{Q^2\to\infty,\ fixed\, x_B} M_P W_1(x_B, Q^2) \to \mathcal{F}_1(x) \tag{1.9}$$

$$\lim_{Q^2 \to \infty,\ fixed\, x_B} W_2(x_B, Q^2) \to \mathcal{F}_2(x) \tag{1.10}$$

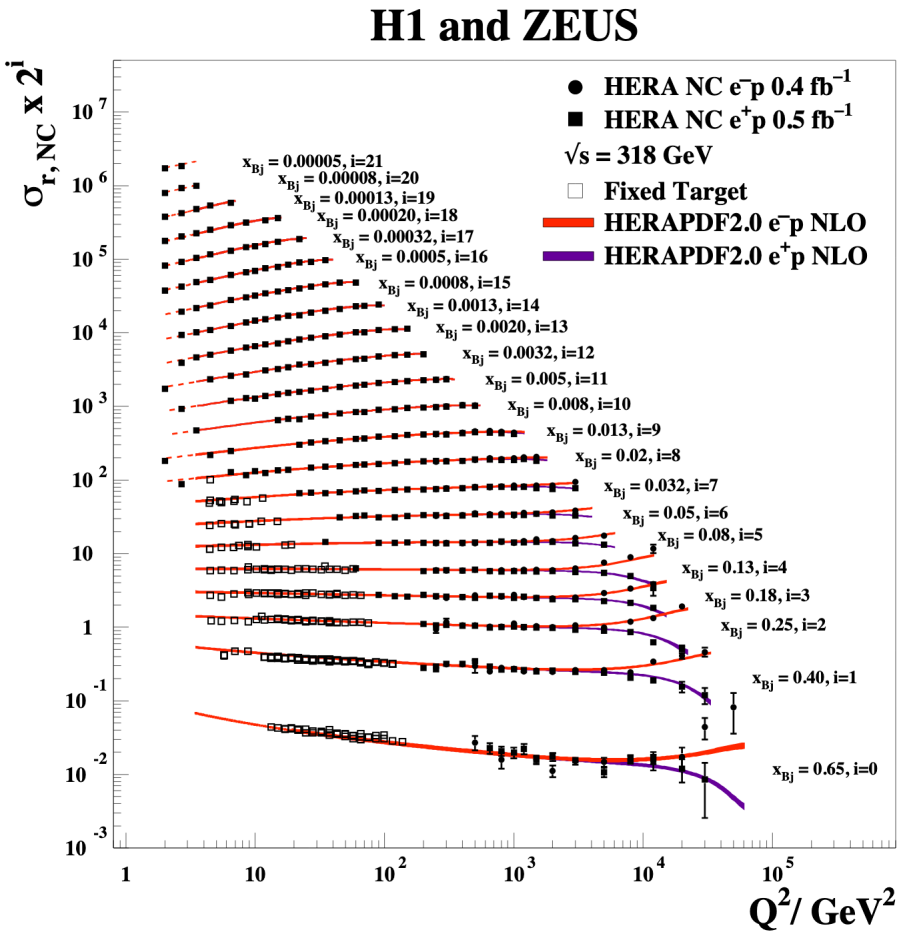

Figure 1.5: Combined DIS cross-section measurements [13] from HERA and fixed target experiments (from the BCDMS and the NMC collaborations) compared to theoretical predictions.

Even if it is now known that this scaling is violated and that the limit does go to 0, this vanishing behavior of DIS is very slow compared to elastic scattering (see figure 1.5) and an approximate scaling was observed at SLAC . This behavior was interpreted as the possible existence of pointlike charged structures in the nucleon. Measurements also showed that the DIS structure functions follow the Callan-Gross relation [14], suggesting that these possible pointlike constituents behave like fermions:

$$W_2(x_B, Q^2) = 2x_B \frac{E - E'}{M_p} W_1(x_B, Q^2) \tag{1.11}$$

Richard Feynman, in 1969, developed the model of partons [15] providing an interpretation of DIS in the Bjorken limit, in an infinite momentum frame. In the parton model and under such conditions, DIS can be interpreted as the scattering off free pointlike constituents called partons

(gradually identified as the quarks and gluons). In this case, the DIS cross-section is written as:

$$\frac{d\sigma_{ep\to eX}}{dx_B dQ^2} = \sum_f e_f^2\, q_f(x)\, \frac{d\sigma_{eq\to eq}}{dx_B dQ^2}\, \delta(x - x_B) \tag{1.12}$$

where $\frac{d\sigma_{eq\to eq}}{dx_B dQ^2}$ is the elastic cross-section between the parton and the lepton and $q_f(x)$ is a parton distribution function (PDF) defined as the probability density for finding a parton of flavor f, electric charge e_f and carrying the proton longitudinal momentum fraction x. The term $\delta(x - x_B)$ implies that only partons that are carrying a longitudinal momentum fraction of x_B contribute. DIS, interpreted in the model of partons, corresponds to the scattering off a free parton, with the nucleon structure encapsulated in the PDFs, these PDFs providing the probability to find this parton in the proton, as represented on figure 1.6. In the parton model, the structure functions can be written:

$$W_1(x_B) = \frac{1}{2} \sum_f e_f^2\, q_f(x_B) \tag{1.13}$$

$$W_2(x_B) = x_B\, \frac{E - E'}{M_P} \sum_f e_f^2\, q_f(x_B) \tag{1.14}$$

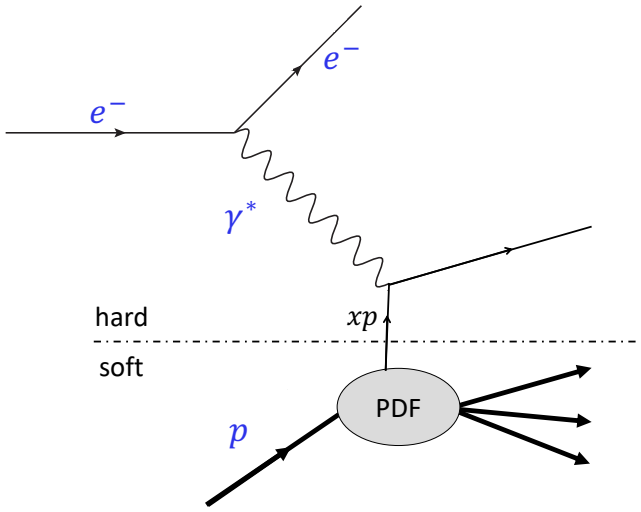

Figure 1.6: Schematic of inelastic scattering as interpreted in the model of partons. The virtual photon scatters elastically off a free quark carrying the longitudinal momentum fraction of the proton, x. Interpreted with QCD, the line separates a hard scattering part (calculable perturbatively) and a soft part parametrized by the PDFs.

In the parton model, the PDFs do not depend on Q^2. The violation of this scaling by gluonic radiation from quarks is encapsulated in the so-called "DGLAP" equations [16] [17] [18] (named after their authors Dokshitzer, Gribov, Lipatov, Altarelli and Parisi), which provide the Q^2-evolution of PDFs, this evidence finally showing that the partons from the parton model can be identified with the quarks and gluons from the quark model.

The quark model, developed at the beginning of 1960's by George Zweig [19] and Murray Gell-Mann [20] (Nobel Prize 1969) had some success in describing the static properties of mesons and baryons but was only slowly associated with the DIS results. In this model, the basic constituents in this model are called quarks and exist with three different flavors (to describe the lightest baryons) interacting via bosons called gluons. The quark model is now encapsulated in the theory of the strong interaction, quantum chromodynamics (QCD).

From the point of view of QCD, the DIS reaction can be factorized in a hard scattering part and a soft part parametrized by the PDFs. Unlike the soft part, this first hard scattering part corresponds to high-energy interactions, for which the strong coupling constant α_S becomes small (property called the asymptotic freedom). The hard scattering part therefore corresponds to the interaction with an quasi-free quark and can be computed perturbatively in QCD.

1.2 Generalized parton distributions

In section 1.1, the two historical approaches that led to the actual understanding of nucleon structure in terms of quarks and gluons have been discussed. In an infinite momentum frame, the FFs provide position information in the transverse plane while the PDFs describe the longitudinal momentum densities of partons. This section explains how the generalized parton distributions (GPDs) emerge from the concept of Wigner distributions and encapsulate the two approaches.

1.2.1 Wigner distributions and their projection

Wigner distributions were introducted in 1932 by Eugene Wigner [21] and have been used is various contexts before nucleon structure. Wigner distributions contain the complete single-particle description of a system with both spatial and momentum information. For a wave function $\psi(\chi)$ with position χ and momentum p, the Wigner distribution is defined as:

$$W(\chi,p) = \int dz\, e^{ipz}\, \psi^*(\chi - z/2)\, \psi(\chi + z/2) \tag{1.15}$$

with z corresponding to a spatial displacement of the wave function ψ. The Wigner distribution is generally not positive definite but reduces to positive definite momentum density $|\psi(p)|^2$ and position density $|\psi(\chi)|^2$ after integration.

The generalization of Wigner distributions to quantum fields [22] [23] [24] [25] is provided by the Wigner operator defined as:

$$\mathcal{W}_\Gamma(\vec{r},k) = \int d^4z\, e^{ik\cdot z}\, \bar{\Psi}(r - z/2)\, \Gamma \Psi(r + z/2) \tag{1.16}$$

with $\vec{r}$ the quark position vector, k the four-momentum conjugated to the spacetime separation z (k corresponds to the average parton momentum) and Γ a Dirac operator to define the nature of

the obtained densities. The Wigner distributions in the proton are obtained by integrating over the momentum transfer to the proton:

$$W_\Gamma(\vec{r},k) = \frac{1}{2M_p}\int \frac{d^3q}{(2\pi)^3}\langle \vec{q}/2|\mathcal{W}_\Gamma(\vec{r},k)|-\vec{q}/2\rangle \tag{1.17}$$

In nucleon structure experiments, the high-energy processes provide a poor measurement of the light-cone energy $k^- = (k^t - k^z)/\sqrt{2}$ (see appendix A.1 for definition of the notations k^+, k^- and $k^\perp$) where z is the axis along the direction of the probe. The "mother distribution" is therefore obtained after integration over k^-:

$$W_\Gamma(\vec{r},\vec{k}) = \int \frac{dk^-}{(2\pi)^2} W_\Gamma(\vec{r},k) \tag{1.18}$$

Unfortunately, there is no known experiment capable of measuring this 6-dimensional distribution but further integrations lead to measurable objects. After integration over the transverse momentum $\vec{k_\perp}$, the 4-dimensional distribution obtained is:

$$\begin{aligned} f_\Gamma(\vec{r},k^+) &= \int \frac{d^{\vec{2}}k_\perp}{(2\pi)^2} W_\Gamma(\vec{r},\vec{k}) \\ &= \frac{1}{2M_p}\int \frac{d^3q}{(2\pi)^3}\, e^{-i\vec{q}\cdot\vec{r}} \int \frac{dz^-}{2\pi}\, e^{iz^-k^+}\, \langle \vec{q}/2|\bar{\Psi}(-z^-/2)\Gamma\Psi(z^-/2)|-\vec{q}/2\rangle \end{aligned} \tag{1.19}$$

which is the Fourier transform of the matrix element corresponding to the so called generalized parton distribution (GPD) $F_\Gamma(x,\xi,t)$:

$$f_\Gamma(\vec{r},x) = \frac{1}{2M_p}\int \frac{d^3q}{(2\pi)^3}\, e^{-i\vec{q}\cdot\vec{r}}\, F_\Gamma(x,\xi,t) \tag{1.20}$$

with the variables (see figure 1.7) defined as follows:

- x is the average longitudinal momentum fraction of the proton carried by the active quark: $x = k^+/p^+$ with $p^+ = E_q/\sqrt{2} = \sqrt{\vec{q}^2/4 + M_p^2}/\sqrt{2}$
- -2ξ is the longitudinal momentum transfer: $\xi = q^z/(2E_q)$
- t is the squared four-momentum transfer to the proton

The transverse momentum distributions (TMDs), can be obtained from the "mother distribution" after integration over the transverse position. TMDs are analogs of GPDs, TMDs carrying the transverse momentum dependence instead of the transverse position dependence carried by the GPDs. TMDs being outside of the scope of this thesis, they are not further described.

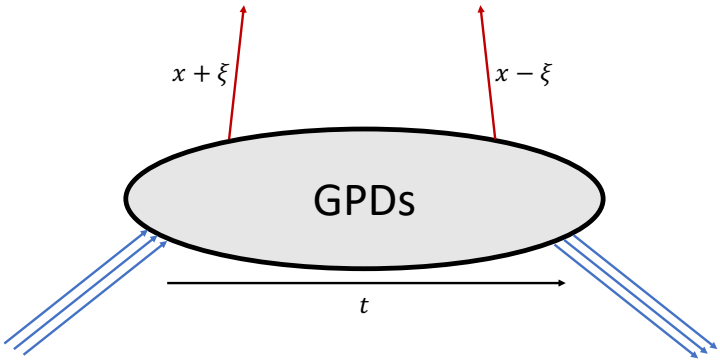

Figure 1.7: Diagram associated with the GPD $F_\Gamma(x,\xi,t)$

1.2.2 Generalized parton distributions

Depending on the choice of Dirac operator Γ, several GPDs are derived from $F_\Gamma(x,\xi,t)$ (see appendix A.1 for notations):

- $\Gamma = \gamma^+$ leads to two vector GPDs, H and E
- $\Gamma = \gamma^+\gamma_5$ corresponds to the axial vector GPDs, $\widetilde{H}$ and $\widetilde{E}$
- $\Gamma = \sigma^{+\perp}\gamma_5$ provides four additional tensor GPDs, H_T, E_T, $\widetilde{H_T}$ and $\widetilde{E_T}$, called transversity GPDs, which will not be detailed here

The unpolarized GPDs H and E do not depend on the parton helicity while the polarized GPDs $\widetilde{H}$ and $\widetilde{E}$ do. Unlike E and $\widetilde{E}$, that correpond to a nucleon helicity flip, GPDs H and $\widetilde{H}$ conserve the nucleon helicity. Finally GPDs H, $\widetilde{H}$, E and $\widetilde{E}$ describe processes that conserve the parton helicity while transversity GPDs correspond to parton helicity flip processes.

The matrix element $F_\Gamma(x,\xi,t)$, shown on figure 1.7, corresponds to the process of emission and reabsorption of a quark or antiquark in the nucleon for $x < -\xi$ or $x > \xi$ (called the "DGLAP" region) and the emission of a quark-antiquark pair in the case $-\xi < x < \xi$ (called the "ERBL" region). Each region follows different Q^2 evolution equations: the "DGLAP" evolution equations [16] [17] [18] in the first region and in the "ERBL" evolution equations [26] [27] in the second region.

1.2.3 Physical content of GPDs

GPDs are generalizations of both PDFs and FFs. The "forward limit" of GPDs (for $t \to 0$ and $\xi = 0$) leads to PDFs:

$$H(x,0,0) = q(x) \tag{1.21}$$

GPDs also follow sum rules that connect them to form factors, for instance:

$$\int_{-1}^{1} dx\, H(x,\xi,t) = F_1(t) \quad \forall \xi \tag{1.22}$$

$$\int_{-1}^{1} dx\, E(x,\xi,t) = F_2(t) \quad \forall \xi \tag{1.23}$$

The physical interpretation of GPDs also shows this encapsulation of FFs and PDFs. Burkardt showed [8] that, for $\xi = 0$, GPDs have a density interpretation in terms of a distribution of longitudinal momentum and transverse position in an infinite momentum frame. The impact parameter dependent parton distribution function is the Fourier transform of GPD H:

$$q(x,\vec{b_\perp}) = \int \frac{d^2\Delta_\perp}{2\pi} e^{i\vec{b_\perp}\cdot\vec{q}_\perp} H(x,0,-\vec{q}_\perp^{\,2}) \tag{1.24}$$

where $\vec{b_\perp}$ is the parton position in the transverse plane (impact parameter). This property of the GPDs leads to a tomographic picture of the nucleon with a decomposition of the transverse position along the longitudinal momentum. The generalization in the case $\xi \neq 0$ is discussed in [28].

Finally, GPDs provide access to the total angular momentum of the quarks J, via the Ji relation [29] [30]:

$$J = \frac{1}{2}\int_{-1}^{1} dx\, x\Big[H(x,\xi,t=0) + E(x,\xi,t=0)\Big] \tag{1.25}$$

1.3 Deeply virtual Compton scattering

1.3.1 Deeply virtual Compton scattering

Generally considered as the cleanest channel to access GPDs, deeply virtual Compton scattering (DVCS) is defined by the reaction $\gamma^* p \to \gamma p$. In the Bjorken regime and under the condition that $|t|/Q^2 \ll 1$, the reaction can be considered to happen at the parton level and can be factorized [31] into a convolution of a hard scattering part (calculable perturbatively in QCD) and a soft part parametrized by GPDs (see figure 1.8).

The DVCS amplitude is parametrized by Compton form factors (CFFs) which are complex integrals of GPDs with a kernel, integrated over x, and, at leading order, only made of quark propagators, such as:

$$\mathcal{H}(\xi,t) = \int_{1}^{1} dx\, H(x,\xi,t)\, \left(\frac{1}{\xi - x - 0i} - \frac{1}{\xi - x + 0i}\right) \tag{1.26}$$

CFFs can be decomposed into a real and an imaginary part as follows:

$$\Re\mathrm{e}\mathcal{H}(\xi,t) = \mathcal{P}\int_0^1 \Big[H(x,\xi,t) - H(-x,\xi,t)\Big]\Big(\frac{1}{x-\xi} + \frac{1}{x+\xi}\Big)dx \tag{1.27}$$

$$\Im\mathrm{m}\mathcal{H}(\xi,t) = \pi\Big(H(\xi,\xi,t) - H(-\xi,\xi,t)\Big) \tag{1.28}$$

where $\mathcal{P}$ is Cauchy's principal value integral. It is interesting to note here that, at leading order, the real part of CFFs provides GPD information integrated over x while the imaginary part of CFFs provides access to the GPDs at the points $x = \xi$ and $x = -\xi$.

GPDs are universal and are also accessible by the study of deeply virtual meson production (DVMP) reactions, for instance, such as π^0 electroproduction $ep \to ep\pi^0$. Results from all these measurements can be combined to provide the most accurate description of nucleon structure.

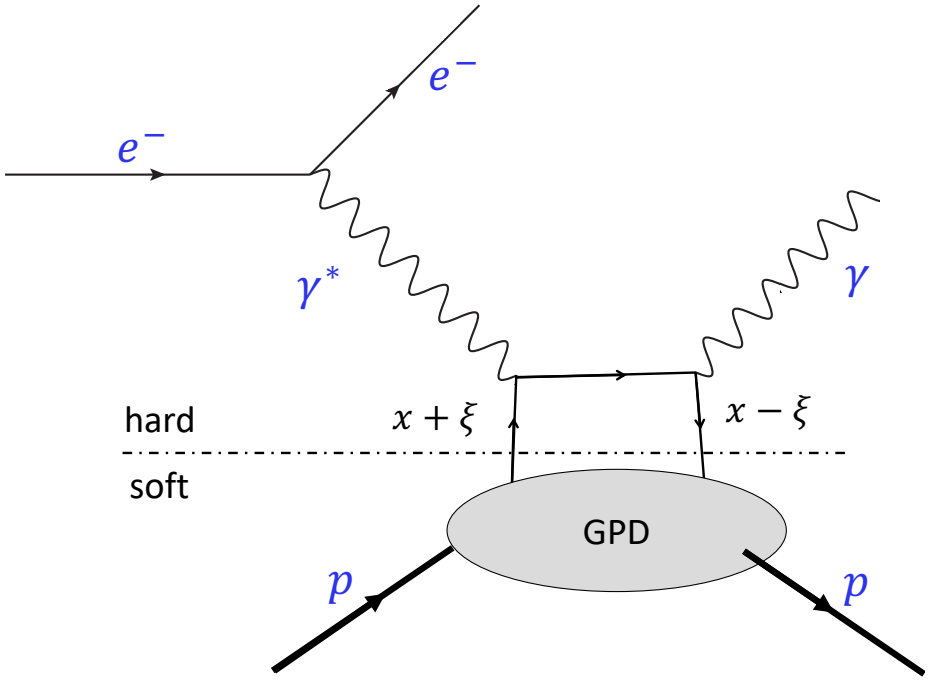

Figure 1.8: "Handbag" diagram for the DVCS process, representing the reaction at leading order and highlighting the factorization of the process

The DVCS amplitude depends on the characteristic angle ϕ, the angle between the leptonic plane (defined by the incoming and scattered electron) and the hadronic plane (defined by the virtual photon and the recoil proton) as shown on figure 1.9 (following the Trento convention [32]).

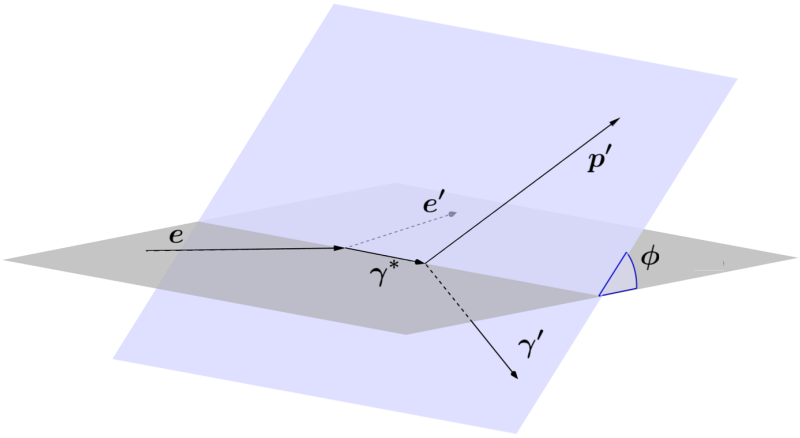

Figure 1.9: Definition of the angle ϕ: angle between the leptonic and hadronic planes.

1.3.2 The reaction $ep \to ep\gamma$

Experimentally, the virtual photon in the DVCS process is produced from the interactions between a lepton from a beam (electrons or muons) with proton. In this thesis, photon electroproduction $ep \to ep\gamma$ is used to study DVCS. However, in the photon electroproduction, it is not possible to distinguish the two processes that interfere: DVCS and the Bethe-Heitler (BH) process, which is elastic scattering of the electron on the proton with a high-energy photon radiated by either the incoming or the outgoing electron (see figure 1.10). Bethe-Heitler is a very well-known process, parametrized by the form factors of the proton, which have been widely studied (see section 1.1.1).

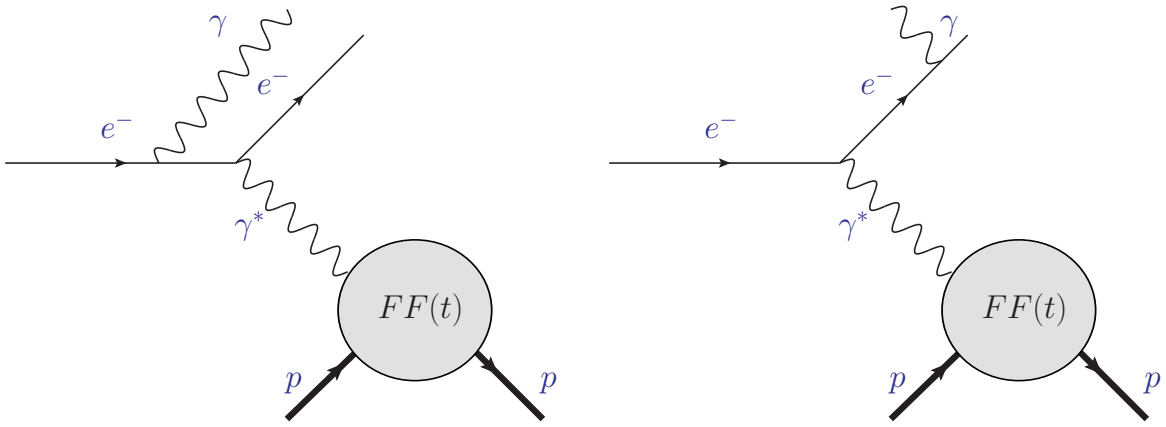

Figure 1.10: The Bethe-Heitler (BH) process, parametrized by the form factors (FFs). Left: the photon is radiated by the incoming electron. Right: the photon is radiated by the outgoing electron.

The differential cross section for electron photonproduction can be written as follows:

$$\frac{d^4\sigma_{ep\to ep\gamma}}{dx_B dQ^2 dt d\phi} = \frac{x_B e^6}{32(2\pi)^4 Q^4 \sqrt{1+\varepsilon^2}} |\mathcal{T}|^2 \tag{1.29}$$

with $\varepsilon = 2x_B\frac{M_p}{Q}$ and $\mathcal{T}$ the photon electroproduction amplitude which can be decomposed in terms of the DVCS and the BH amplitudes:

$$\begin{aligned} |\mathcal{T}|^2 &= |\mathcal{T}_{DVCS}|^2 + |\mathcal{T}_{BH}|^2 + \mathcal{I} \\ &= |\mathcal{T}_{DVCS}|^2 + |\mathcal{T}_{BH}|^2 + \mathcal{T}_{DVCS}\mathcal{T}^*_{BH} + \mathcal{T}^*_{DVCS}\mathcal{T}_{BH} \end{aligned} \tag{1.30}$$

where $\mathcal{T}_{DVCS}$, $\mathcal{T}_{BH}$ and $\mathcal{I}$ are the DVCS, BH and interference contributions. These amplitudes are traditionally written as an harmonic expansion with respect to the ϕ angle. For the case of an unpolarized target, the dominant terms of the expansion are:

$$|\mathcal{T}_{BH}|^2 = \frac{1}{x_B^4 t^2 (1+\varepsilon^2)^2 \mathcal{P}_1(\phi)\mathcal{P}_2(\phi)} \left\{ \sum_{n=0}^{n=2} \left[c_n^{BH} cos(n\phi) \right] + s_1^{BH} sin(\phi) \right\} \tag{1.31}$$

$$|\mathcal{T}_{DVCS}|^2 = \frac{1}{Q^2} \left\{ c_0^{DVCS} + \sum_{n=1}^{n=2} \left[c_n^{DVCS} cos(n\phi) + \lambda s_n^{DVCS} sin(n\phi) \right] \right\} \tag{1.32}$$

$$\mathcal{I} = \frac{1}{x_B y t \mathcal{P}_1(\phi)\mathcal{P}_2(\phi)} \left\{ c_0^I + \sum_{n=1}^{n=3} \left[c_n^I cos(n\phi) + \lambda s_n^I sin(n\phi) \right] \right\} \tag{1.33}$$

where λ is the beam helicity and all the coefficients c_n^{BH}, s_n^{BH}, c_n^{DVCS}, s_n^{DVCS}, c_n^I and s_n^I and the BH propagators $\mathcal{P}_1(\phi)$ and $\mathcal{P}_2(\phi)$ can be found in [33]. The BH coefficients c_n^{BH} and s_n^{BH} are connected to nucleon structure by the elastic FFs. The DVCS coefficients c_n^{DVCS} and s_n^{DVCS} are formed of bilinear combinations of Compton form factors (CFFs). Finally the interference coefficients c_n^I and s_n^I are functions of both elastic FFs and CFFs. Tote that the coefficients s_3^I, s_2^{DVCS} and s_1^{BH} are null for unpolarized targets.

1.3.3 Beam-spin asymmetry to access generalized parton distributions

The analysis in this thesis makes use of the longitudinaly polarized electron beam from the CEBAF accelerator (see section 2.1) to measure photon electroproduction beam-spin asymmetry (BSA). The BSA is defined by:

$$A_{LU} = \frac{d\sigma^{\uparrow} - d\sigma^{\downarrow}}{d\sigma^{\uparrow} + d\sigma^{\downarrow}} \tag{1.34}$$

where $d\sigma^{\uparrow}$ and $d\sigma^{\downarrow}$ are the photon electroproduction differential cross-sections for positive and negative electron beam helicity (for simplicity, $d\sigma^{\uparrow}$ and $d\sigma^{\downarrow}$ are used instead of the notation of equation 1.29). Asymmetries are generally easier to measure than cross-sections since the ratio of cross-sections leads to the simplification of the normalization factors. In particular, from an experimental point of view, the main advantage of the BSA is that this observable can be computed from raw yields. In the case of an unpolarized target, because of the helicity coefficient in front of the "s"-coefficients in the DVCS and interference expansions, only the coefficients s_1^I, s_2^I and s_1^{DVCS} remain at the numerator of the BSA. In the kinematic range of this analysis,

the dominant contribution is expected to come from s_1^I. On the contrary, the denominator is formed of the BH, DVCS and interference "c"-coefficients, with the dominant contributions expected to come from the BH coefficients c_0^{BH}, c_1^{BH} and the interference coefficients c_0^I and c_1^I. The harmonic coefficients of main interest for the study of GPDs are therefore c_1^I and s_1^I. These coefficients can be written as follows [33]:

$$c_1^I \propto \mathfrak{Re}\left[F_1\mathcal{H} + \xi(F_1+F_2)\widetilde{\mathcal{H}} - \frac{t}{4M_p^2}\mathcal{E}\right] \tag{1.35}$$

$$s_1^I \propto \mathfrak{Im}\left[F_1\mathcal{H} + \xi(F_1+F_2)\widetilde{\mathcal{H}} - \frac{t}{4M_p^2}\mathcal{E}\right] \tag{1.36}$$

Since $F_1 > F_2$ and t and ξ are relatively small, BSA measurements on an unpolarized proton target are expected to be mainly sensitive to $\mathfrak{Re}\mathcal{H}$ and $\mathfrak{Im}\mathcal{H}$.

Under the assumptions that the dominant terms are: s_1^I, c_0^{BH}, c_1^{BH}, c_0^I and c_1^I, the BSA can be reduced to the following form:

$$A_{LU} = \frac{A\sin(\phi)}{1+B\cos(\phi)} \tag{1.37}$$

where

$$\begin{aligned} A &= \frac{s_1^I}{\kappa c_0^{BH} + c_0^I} \\ B &= \frac{\kappa c_1^{BH} + c_1^I}{\kappa c_0^{BH} + c_0^I} \\ \text{and} \quad \kappa &= \frac{y}{x_B(1+\varepsilon^2)^2} \\ y &= \frac{q\cdot p}{k\cdot p} \end{aligned} \tag{1.38}$$

This simple form of the asymmetry will be used later in the analysis (section 4) to fit the BSA, but tests of the validity of these assumptions or fits including more coefficients would be important in the future.

1.4 Experimental status

As mentioned above, DVCS is one of the cleanest channel to access GPDs. However, since the cross-section is relatively low (on the order of 1-100 $\mathrm{pb/GeV^4}$ in the kinematic region of interest here), a high luminosity is necessary. In addition, it is important to combined measurements with polarized beams, beams of different charges and polarized targets since they provide access to different CFFs with different sensitivities [34]. The use of neutron targets and the study of deeply virtual meson production (DVMP) is also complementary to the study of proton DVCS, providing access to flavor separation and probing different GPDs. A recent status of DVMP experiments can be found in [35].

Experimental programs have been developed over a large kinematic range mainly classified in three categories: the low x_B, the medium x_B and the high x_B experiments, as shown on figure 1.11.

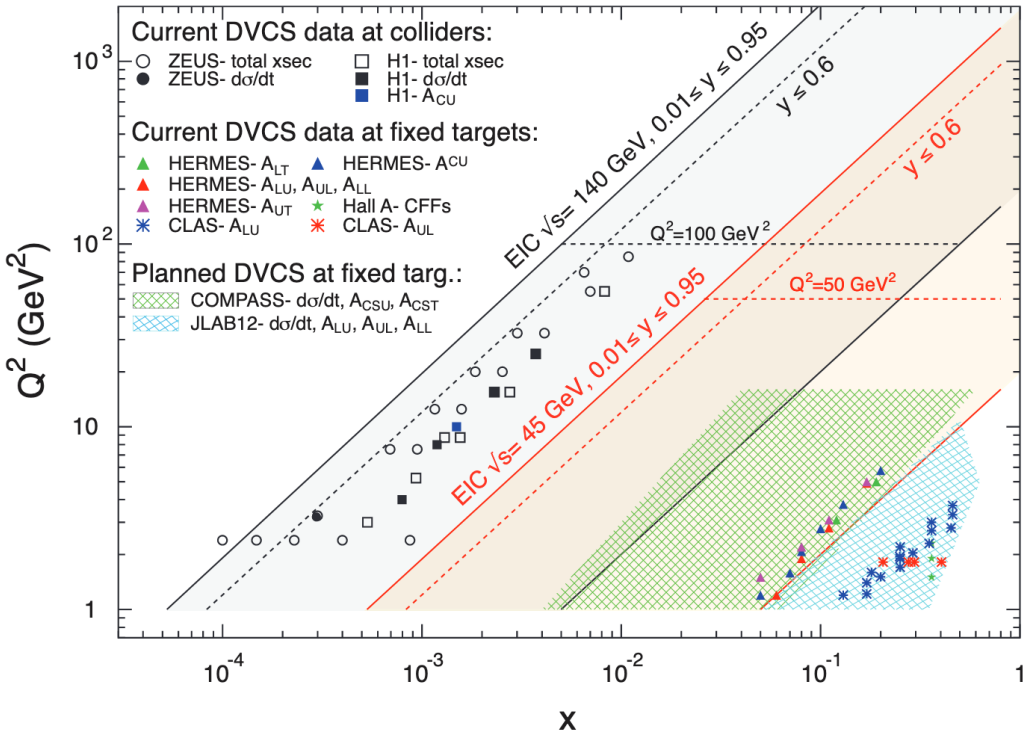

Figure 1.11: Overview of the Q^2 and x_B coverage of DVCS experiments in 2016 (figure from [36]).

1.4.1 Measurements in the low x_B region

DVCS measurements at low x_B were done with the H1 and ZEUS detectors at DESY (Deutsches Elektronen-Synchrotron) with the HERA (Hadron-Elektron-Ring-Anlage) accelerator in Hamburg, Germany. HERA was able to provide up to 27 GeV electron/positron beams and 920 GeV proton beams to collide for the H1 and ZEUS experiments, leading to very high Q^2, up to $100\,\mathrm{GeV}^2/\mathrm{c}^4$. At such high virtuality, the BH contribution is very small, so H1 and ZEUS provided quasi-pure DVCS measurements and were able to extract cross-sections [37] [38] and beam-charge asymmetries [39]. The contribution of sea quarks and the importance of gluon exchange at very low $x_B \simeq 10^{-3}$ was shown by these experiments.

The EIC (Electron-Ion Collider) [36] that will be built in the coming years at BNL (Brookhaven National Laboratory) will provide very intense and high-energy polarized electron and proton beams. The EIC will cover an unprecedented phase-space in the low and medium x_B regions with a luminosity roughly a thousand times larger compared to the DESY experiments.

1.4.2 Measurements in the medium x_B region

The HERMES experiment was a fixed-target experiment also taking place at DESY between 1995 and 2007. HERMES was dedicated to the "quark gluon study of matter". HERMES collected data at $x_B \simeq 10^{-1}$ and Q^2 from 1 to 6 $\mathrm{GeV}^2/\mathrm{c}^4$ and provided a very large set of asymmetries with polarized electron and positron beams sent onto fixed polarized targets (longitudinally and transversely) (see, for instance, [40]). Hence HERMES results have given important constraints on the CFFs and significantly contributed to the parametrization of GPD models.

The COMPASS (Common Muon and Proton Apparatus for Structure and Spectroscopy) experiment at CERN [41] has recently taken DVCS data with a 160 GeV muon beam. COMPASS makes use of the SPS (Super Proton Synchrotron) proton beam to form polarized muon beams of both charges. A recoil detector has been installed to detect the recoil proton and ensure a full exclusivity of the DVCS measurements (with all the particles detected in the final state). COMPASS will provides access to the region between $x_B \simeq 10^{-2}$ and $x_B \simeq 5 \cdot 10^{-1}$, which has not yet been explored.

1.4.3 Measurements in the high x_B region

Several DVCS experiments have been carried out at Jefferson Lab, USA, in the experimental Hall B with CLAS (CEBAF large acceptance spectrometer), and in Hall A. CLAS measurements cover a wide range of Q^2 and x_B, mainly in the valence region. Polarized electron beam from the CEBAF accelerator and the use of polarized targets made possible the measurement of beam, target and double-spin asymmetries [42] [43] [44] [45] [46]. Hall A experiments have a smaller acceptance but can run at a much higher luminosity and have measured DVCS cross-sections with very high precision for given Q^2 and x_B values [47] [48].

CLAS was recently upgraded to CLAS12 to operate at higher luminosity and higher beam energy (up to roughly 11 GeV). CLAS12 also benefits from the CEBAF polarized electron beam and will use several polarized targets to measure beam, target and double-spin asymmetries and cross-sections. A neutron detector will also allow the exclusive measurement of neutron DVCS. The CLAS12 experiment is described in more detail in section 2. A letter of intent was recently submitted to study the possibility to upgrade CEBAF and deliver a polarized positron beam [49]. CLAS12 will therefore provide a nearly exhaustive set of measurements over a large kinematic range and with a high precision. By combining all these measurements, the contribution from the different CFFs will be identified and CLAS12 will provide precise constraints for GPD models.

Chapter 2

Experimental setup: the CLAS12 spectrometer

Thomas Jefferson National Accelerator Facility (Jefferson Lab or JLab) is a US Department of Energy facility founded in 1984 and located in Virginia. The Jefferson Lab main accelerator, called CEBAF (Continuous Electron Beam Accelerator Facility), delivers a continuous and longitudinally polarized electron beam to four experimental halls labeled from A to D. CEBAF delivered its first electron beam in 1994 and started its physics program in 1995. The Jefferson Lab physics program [50] is mainly dedicated to the understanding of nucleon structure, the study of hadrons in nuclei, hadron spectroscopy and the search for new physics.

In this chapter, after a brief presentation of the CEBAF accelerator, the hall B beamline instrumentation and target system are characterized. Finally, CLAS12 (CEBAF Large Acceptance Spectrometer), the main spectrometer in the experimental hall B, is described. Unless specified otherwise, this chapter does not describe work done by the author of this thesis.

2.1 CEBAF

The CEBAF accelerator is a multipass superconducting radiofrequency (RF) linear accelerator (linac) in which the electron beam makes up to 5.5 passes, reaching up to 12 GeV, before being sent to the experimental halls (see figure 2.1). More specifically, it is based on two anti-parallel linacs connected to each other by five vertically stacked recirculation arcs forming a 1400 m long race-track.

With the CEBAF 12 GeV upgrade [51], five 100 MV cryomodules were added to each of the two linacs, to reach about 1.1 GeV/linac. A new experimental hall (hall D) was also built and added to the original halls A, B and C. The upgrade results in a maximum energy of about 11 GeV delivered to halls A, B and C and about 12 GeV for hall D.

The initial electron beam is produced from a photoelectron gun: a polarized laser strikes a photocathode leading to a polarized electron beam. More precisely, four independent lasers (one

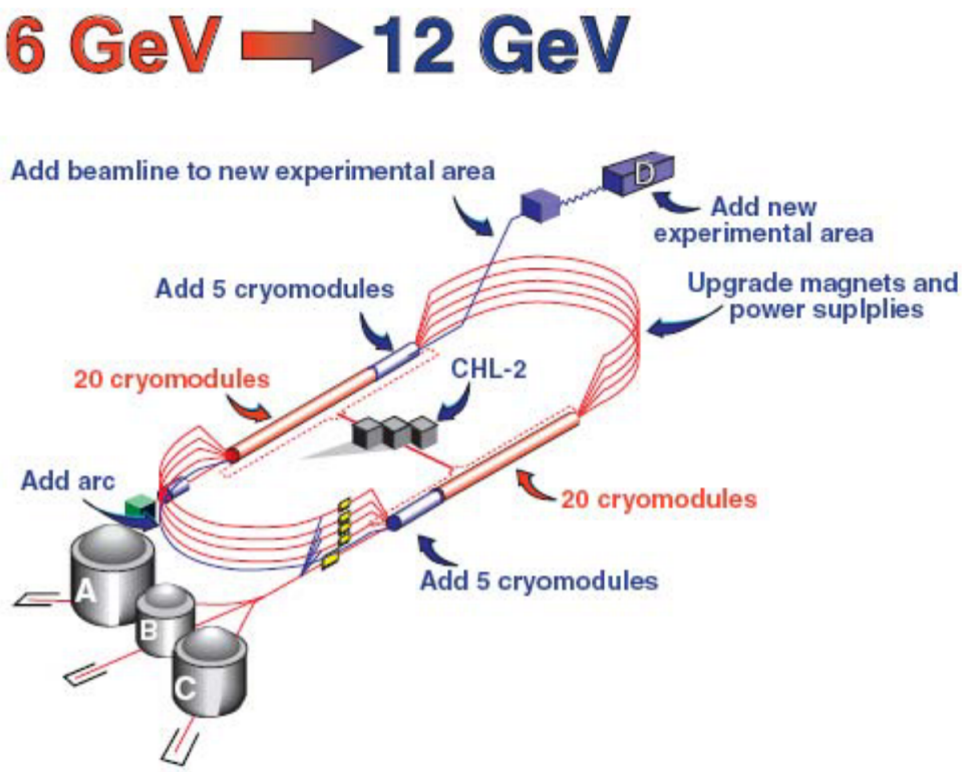

Figure 2.1: Schematic of the CEBAF accelerator highlighting the 12 GeV upgrade [51].

for each hall), functionning either at 249.5 MHz or 499 MHz depending on the configuration of the halls, are first combined into a 1497 MHz beam [52]. This leads to the formation of a continuous wave beam from interleaved beams individually prepared, allowing simultaneous operation of experimental halls at different beam energies and beam currents. This initial beam is then circularly polarized using Pockels cells and waveplates before being sent onto the photocathode. The photocathode is made of a strained superlattice of gallium arsenide in an ultra-vacuum chamber [53], it has a relatively good quantum efficiency (initial quantum efficiency $\simeq 1\%$) and provides an electron beam with a very high polarization (above 85%).

The initial 130 keV electron beam, produced from the photoelectron gun, is then gradually accelerated in the injector [54]. The injector, also upgraded with a new cryomodule during the 12 GeV upgrade, brings the beam energy to 123 MeV while controlling its characteristics before sending it to the linacs.

Once accelerated in the linacs to the desired energy, after up to 5 passes (5.5 for hall D), the electrons are delivered to the experimental halls by radiofrequency (RF) separators and magnets. Halls A and C have spectrometers with a very limited acceptance which are able to operate at an extremely high luminosity (up to $10^{38} cm^{-2} s^{-1}$), leading to very precise measurements in small phase-space regions. Halls B and D are able to provide a large set of measurements but with a lower precision (a luminosity up to $10^{35} cm^{-2} s^{-1}$) due to their very large acceptance and therefore limited beam current.

2.2 Hall B

Hall B is one of the three original experimental halls with hall A and hall C. The main spectrometer used in hall B, the CEBAF Large Acceptance Spectrometer (CLAS) was upgraded to CLAS12 [55] to operate with the CEBAF 12 GeV upgrade. Because of its large acceptance (leading to high occupancies in the detectors), it operates at a relatively low current (between 1 and 100 nA) requiring dedicated instrumentation along the beamline.

2.2.1 Beamline instrumentation

In order to conduct the physics program, hall B is equipped with a set of beamline devices [56] to control the quality and stability of the beam delivered to the hall and measure its main characteristics. Indeed, the experiments taking place in hall B require a stable beam (in particular its transverse size and position) for safe operation, as well as an accurate measurement of the beam current and its polarization.

The first part of the hall B beamline, mainly controlled by the accelerator staff, is equipped with several devices, including magnetic quadrupoles and dipoles, which are essentially used to shape and position the beam. The second part is mainly controlled by the hall B shift staff and contains mostly beam monitoring tools. Most of these devices are described below and some are shown on figure 2.2.

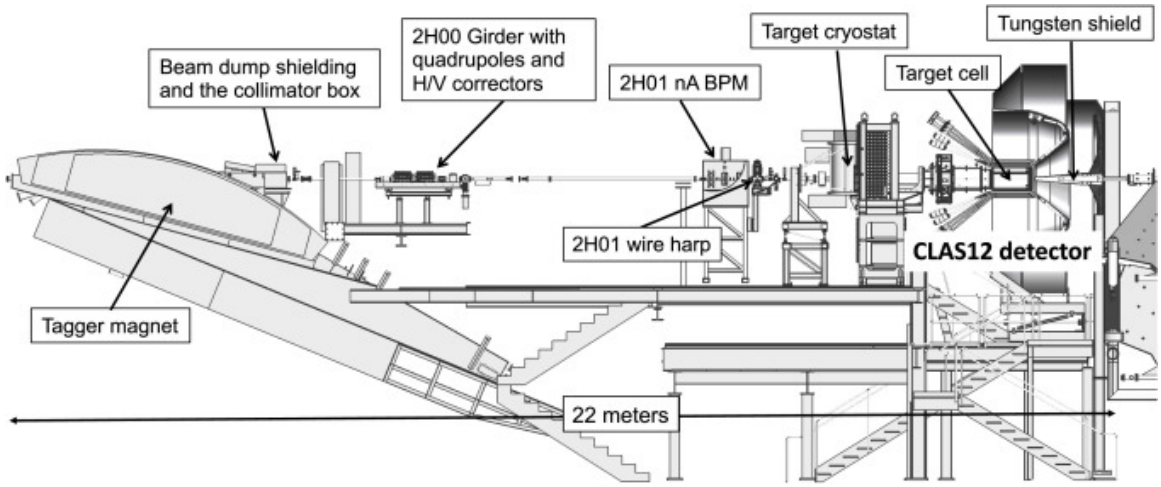

Figure 2.2: Schematic of the end of the Hall B beamline and some of its devices [56].

Beam stability measurements

The safety of CLAS12 detectors is mainly ensured by beam halo counters associated with the fast shutdown (FSD) procedure. Beam halo counters consist of photomultiplier tubes (PMT) which record the light produced by scintillation or Cherenkov effect from plastic mounted on their photocathode (see A.3 for a brief explanation). Beam halo counters are positioned closed to

the beamline at three different locations along it. Any increase of the count rate in the beam halo counters beyond a given safety threshold triggers the FSD procedure preventing the accelerator from delivering beam. Other PMT-based devices called the beam-offset monitors (BOMs) are located on the target (see section 2.2.2) and are integrated in the FSD. Upstream collimators are also installed to protect sensitive detectors.

Beam position measurements

In order to test the beam quality, beam position monitors (BPMs), as well as harps, are installed along the beamline. Wire harps [57], made of tungsten wires, moving across the beam at different angles in the transverse plane, are used in combination with the beam halo counters to establish the beam transverse profile (the FSD being disabled during the harp scan). In addition, BPMs [56], using position-sensitive resonant cavities specially designed for hall B low currents [58], are continuously measuring the beam position in the transverse plane, and are used as feedback in the beam position control loop.

Beam current measurements

Beam current measurements are done at several points along the beamline and with several devices such as the Faraday cup. The Faraday cup [59] is a large lead cup mounted inside a vacuum chamber that converts the collected charge into an electric current. The BPMs can also be used to measure the current in addition to the beam position.

Beam tuning

A tagger dipole, positioned upstream of the detectors, is used during beam tuning to protect them against any sort of radiation damage. Designed for up to 6.2 GeV operation (before the CEBAF 12 GeV upgrade), the beam was initially deflected by the tagger dipole into a dump and was used, in combination with a radiator, to induce a tagged photon beam. The tagger dipole was kept after the 12 GeV upgrade, however, when the beam energy is above 6.2 GeV the beam has to be dumped inside the tagger magnet itself and the beam current is limited to a few nA.

During the beam tuning procedure in hall B, to protect the detectors, the beam is initially dumped in the tagger dipole and is tuned in the first part of the beamline, upstream of the tagger. The first set of wire harps and beam halo counters are used to measure the beam characteristics. Once the profile is satisfying (stable and with a transverse width below 300 μm) in the first part of the beamline, the tagger dipole is switched off and the beam is then tuned, with the same procedure, in the rest of the beamline in the hall.

Beam polarization measurements

Finally, a Møller polarimeter (based on electron-electron scattering) is used to measure the beam polarization received in hall B [56]. Polarization measurements are done using a polarized target installed upstream of the tagger dipole, the latter magnetized to protect the detectors. The target consists of two iron-cobalt alloy foils oriented at $\pm 20^{\circ}$ with respect to the beamline. Scattered electrons from Møller scattering, separated with quadrupole magnets, are detected in coincidence, and the asymmetry is computed while varying the polarization of the target. The amplitude of the asymmetry is then used to compute the beam polarization. Polarization measurements are done with an absolute precision of a few percent.

2.2.2 Target

For the CLAS12 experiment, unpolarized liquid hydrogen and liquid deuterium cryogenic targets have so far been used. These targets are made of a 50 mm-long Kapton cone target cell, with an upstream diameter of 24 mm and a downstream diameter of 15 mm (see figure 2.3). The cell is inside a 450 mm-long and 100 mm-wide scattering chamber. The scattering chamber plays the role of an extension of the beamline around the target. It maintains vacuum around the target and keeps the material thickness as small as possible, to limit the interactions of the particles scattered from the target. A set of beam halo counters, called beam-offset monitors (BOMs), are used to monitor the position of beam around the target and are also integrated into the FSD. CLAS12 and the target system are designed to use a large set of different targets including liquid hydrogen, liquid deuterium, ammonia and nuclear targets with different polarizations. During operation, the liquid hydrogen target is kept at a pressure of 1.2 bar and is cooled at 20.16 K to be in a fully liquid state. In the rest of this document, and in particular for the analysis, an unpolarized liquid hydrogen target is used, to study electron scattering off protons.

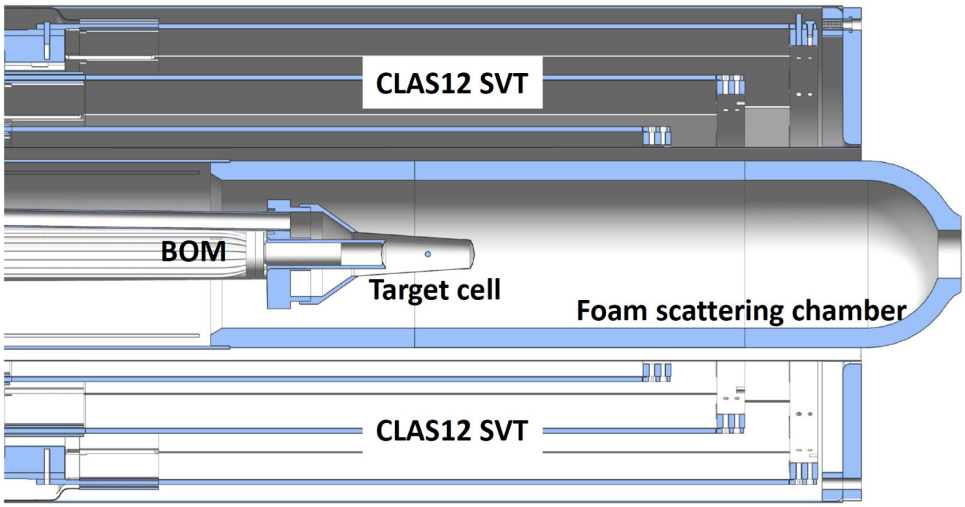

Figure 2.3: Schematic of the target system, with the beam-offset monitors and the innermost CLAS12 detectors [56].

2.3 CLAS12

The CLAS12 spectrometer is the main spectrometer in hall B, it was commissionned at the end of 2017 and took its first physics data in spring 2018.

The goal of the CLAS12 spectrometer is to provide a complete reconstruction and identification of the particles by determining their charge, mass and momentum based on the combined use of several detectors. Tracking systems are responsible for the reconstruction of the charge and momentum of the particles by measuring the curvature of the tracks in a magnetic field. Identification of the particle is completed by measurement of its energy or its velocity which provides the particle mass, as shown in equation 2.1 where E is the energy of the particle, m its mass, p its momentum and c the speed of light in vacuum:

$$E^2 = m^2c^4 + p^2c^2 \tag{2.1}$$

The CLAS12 spectrometer is divided into three main parts (see figure 2.4):

- the central region: to detect particles scattered with a large polar angle (see notations in appendix A.2):
$$35^\circ < \theta < 125^\circ \tag{2.2}$$
- the forward region: to detect particles emitted with a polar angle:
$$5^\circ < \theta < 35^\circ \tag{2.3}$$
- the forward tagger: to detect the very forward particles:
$$2^\circ < \theta < 5^\circ \tag{2.4}$$

Most of the scattered electrons are detected in the forward detector or forward tagger while the central detector is generally used to detect low-momentum recoil particles.

Each region has its own tracking system to measure the momentum of the particles, followed by particle identification detectors. In the central region (see section 2.3.1), the tracking system is made of the association of a silicon vertex tracker (SVT) and a Micromegas vertex tracker (MVT) inside a 5T-solenoidal magnetic field (the SVT and MVT forming the central vertex tracker CVT). Particle identification is given by a central time-of-flight detector (CTOF) and a central neutron detector (CND). In the forward region (described in section 2.3.2), the tracking system is formed of drift chambers immersed in a toroidal magnetic field (up to 3.58 T). A forward Micromegas tracker (FMT) was designed to improve the reconstruction of the vertex in the forward region but was not used to produce the data used in this thesis. A forward time-of-flight detector (FTOF), a high-threshold Cherenkov counter (HTCC), an electromag-

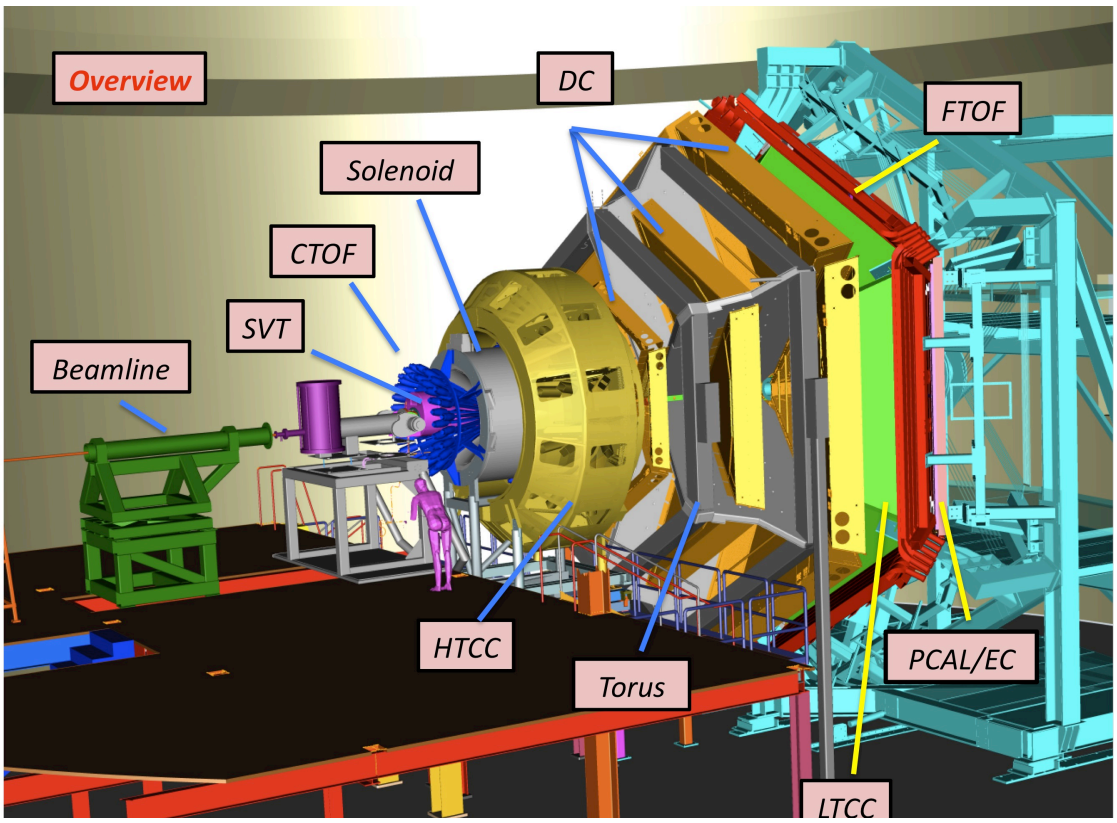

Figure 2.4: Schematic of the CLAS12 spectrometer from the side, the main detectors used in this analysis are indicated.

netic calorimeter (EC) and a pre-shower calorimeter (PCAL) provide the particle identification for most of the particles in the forward region. Additional detectors exist in the forward region, a ring-imaging Cherenkov detector (RICH) and a another Cherenkov detector called the low-threshold Cherenkov counter (LTCC). However since they are not relevant in this thesis they are not described here. Finally the forward tagger (see section 2.3.2) is equipped with a Micromegas tracker and the identification is provided by a calorimeter and a hodoscope.

2.3.1 Central region

The central region (see figures 2.5 and 2.6), also called the "central detector" or the "barrel", is a set of detectors used for particles emitted with a polar angle between 35° and 125°. Starting from the target, the innermost detector is the central vertex tracker (CVT), followed by the central time-of-flight detector (CTOF) and the central neutron detector (CND).

Tracking system: central vertex tracker

The central vertex tracker (CVT) is responsible for the reconstruction of momentum and vertex in the central region. It consists of the silicon vertex tracker (SVT) and the barrel Micromegas tracker (BMT) inside a 5 T solenoidal field, as shown on figure 2.7. The momentum and the

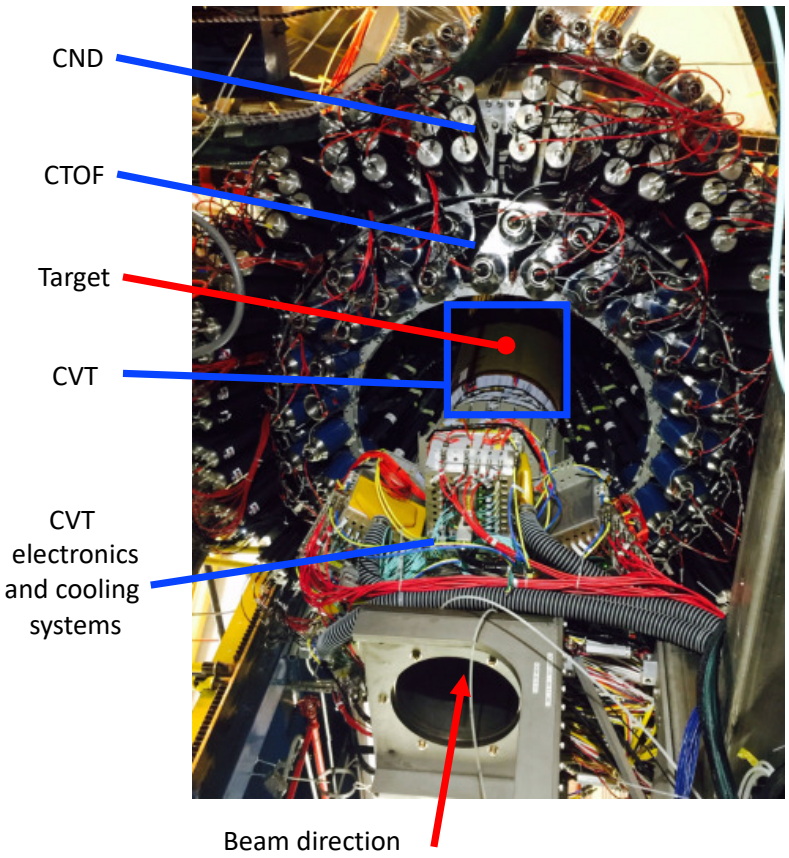

Figure 2.5: Photo of the central region [55] taken from upstream. The outermost PMTs correspond to the CND and the CTOF, while the CVT, taken out here, is shown at the center of the picture. The approximate position of the target, not visible on the photo, is indicated.

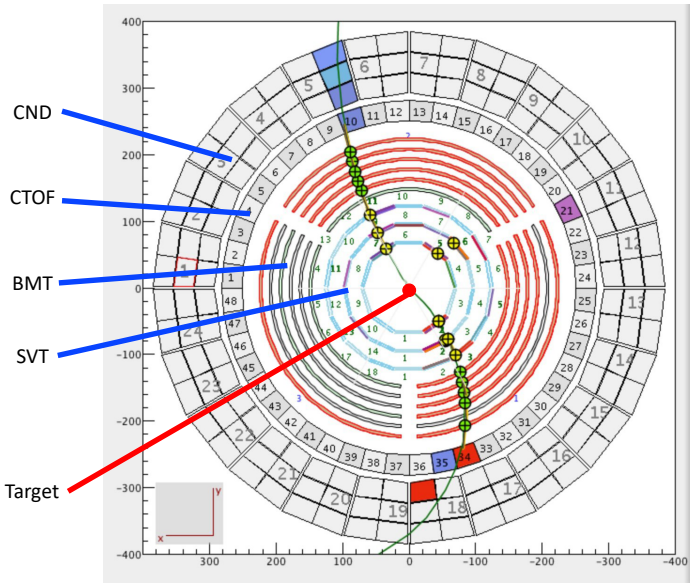

Figure 2.6: Diagram of two particles reconstructed by the detectors in the central region, visualised thanks to the from the CLAS12 event display (see section 2.3.4). The view is taken from the tranvserse plane (x-y plane, see notations in appendix A.2).

vertex of the charged particle are obtained by identifying its trajectory in the magnetic field, which is reconstructed from the information given by each detection layer in the CVT. The 5 T solenoidal field is also used to protect the drift chambers against electrons produced by Møller scattering in the target.

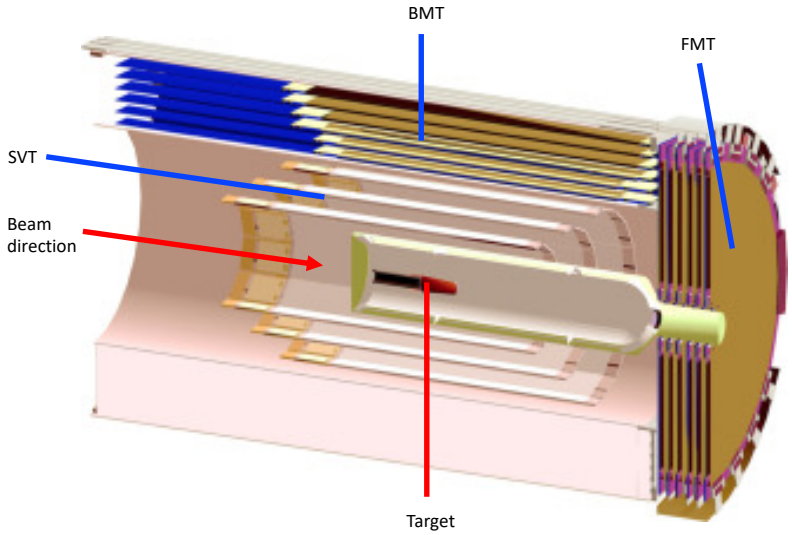

Figure 2.7: Diagram of the detectors [55] around the target system with the six layers of BMT, the three double layers of SVT and the Forward Micromegas Tracker (FMT).

The SVT [60] is a silicon detector (a brief description of the principle of silicon detectors is given in appendix, section A.3.1). The SVT is formed of 42 microstrip modules arranged in three polygonal regions of 10, 14 and 18 modules (as shown on figures 2.6 and 2.7). Each module is double-sided and each side has 256 strips. In order to provide two-dimensional information, the SVT strips make an angle, varying between -3° and 3°, with the longitudinal axis of the module. The spatial resolution for the SVT is expected to be below 50 μm, resulting in an azimuthal resolution below 5 mrad and a polar resolution between 10 and 20 mrad.

The BMT [61] consists of six layers of cylindrical Micromegas detectors divided in three azimuthal sectors (see figures 2.6 and 2.7). Three layers, with strips along the beamline, called Z layers, provide information about the azimuthal angle and three layers with circular strips perpendicular to the beam axis, called C layers, provide information about the polar angle. Each individual detector, called a tile, covers an azimuthal angle of about 115°, called a sector. Therefore an almost full azimuthal coverage is obtained with three tiles per layer, leading to a total of 18 Micromegas tiles. The expected spatial resolution of the MVT is between 100 μm and 200 μm. The information provided by the MVT is combined with the the information provided by the SVT to improve both the vertex and the polar angle resolution. Detailed information about the Micromegas detectors can be found in chapter 3.

Another Micromegas detector was designed to be positioned in the central region to supplement the forward tracking: the forward Micromegas tracker (FMT). The BMT and the FMT

were designed together to form the Micromegas vertex tracker (MVT). However, since the FMT was removed in summer 2018 and was not used for the data taking it is not described in this chapter, though detailed information can be found in chapter 3.

Particle identification: central time-of-flight detector and central neutron detector

The central time-of-flight detector (CTOF) [62] is a scintillator-based detector responsible for the identification of charged particles in the central region (see section A.3 for a brief description of scintillators and the time-of-flight technique). It is made of 48 3 cm-thick plastic scintillation bars arranged to form a cylinder (see figure 2.8). Each scintillation bar is connected, on each end (downstream and upstream), to a photomultiplier tube (PMT) by a light guide. Because of the very limited space available to place the PMTs and the strong magnetic field in the solenoid, long bent light guides are used (1 m upstream and 1.6 m downstream). The CTOF is designed to have large signals to account for the limited transmittance (roughly 50% to 60%) due to the important length of the light guides. A magnetic shield is added to the PMTs to compensate for the fringe field of the solenoid.

Particle identification is done using the time-of-flight method, comparing the time measured by the CTOF and the start time calculated by the trigger system. It is designed to have an effective time resolution of 80 ps leading to a separation at 3σ for π/K up to 0.58 GeV/c, 0.93 GeV/c for the K/p separation and 1.14 GeV/c for the π/p separation.

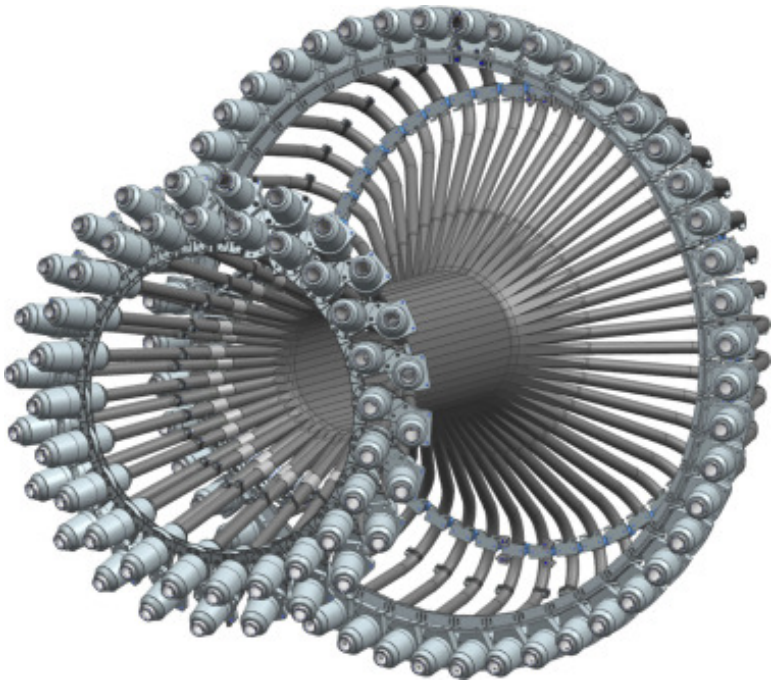

Figure 2.8: Schematic of the CTOF [55] with its 48 3 cm-thick scintillator bars connected to PMTs .

The central neutron detector (CND) [63] is responsible for the identification and the reconstruction of momentum for neutrons emitted in the central region. In the same way as the CTOF,

the CND is made of scintillator bars connected to PMTs using light guides, but in of 3 layers of 48 scintillators each. It is used in addition to the CTOF to increase the neutron detection efficiency. The CND was not be used for the measurement presented in this thesis.

2.3.2 Forward region

The forward region, also called "forward detector", is a set of detectors used to detect particles emitted with a polar angle between 5° and 35°. From upstream to downstream, detectors in the forward region are: a high-threshold Cherenkov counter (HTCC), drift chambers (DCs) associated with a toroidal magnet (called torus, and providing a magnetic field up to 3.58 T), forward time-of-flight (FTOF) and an electromagnetic calorimeter (EC).

The forward region is divided into 6 sectors, structured around the 6 superconducting coils of the torus. All sectors cover almost 60° each in order to have an almost full azimuthal coverage. All six sectors in the forward region are identical, with the exception of the ring-imaging Cherenkov detector (RICH) and low-threshold Cherenkov counters (LTCC), not relevant in this thesis and not detailed here.

Tracking system: drift chambers

The drift chambers, associated with the torus, are responsible for the tracking in the forward region [64] (the principle of drift chambers is described briefly in section A.3.2). The drift chambers are positioned between the HTCC and the FTOF, roughly 2 to 4 m downstream of the target, and are structured around the torus as shown on figure 2.9. The drift chamber system is composed of three independent radial regions, each of them made of six identical sectors covering the entire azimuthal range. Each region of the drift chambers is placed in a different magnetic field area, as shown on figure 2.11. Each region is made of 12 layers, with 112 sense wires per layer. Wires are organized within an hexagonal cell structure, each sense wire being surrounded by six field wires, with a cell radius increasing with the distance to the target (from 0.78 cm to 1.96 cm). The wires are strung between the two endplates as shown on figure 2.10. Half of the wires make a 6° stereo angle with respect to the sector midplane while the other half makes an angle $-6°$. The gas inside the chambers is a mixture made of 90% argon and 10% CO_2 by mass, the gas is continuously being renewed at a rate of roughly two or three volumes per day. The expected single-wire spatial resolution for the drift chamber is between 300 μm and 500 μm.

Particle identification: high-threshold Cherenkov counter, forward time-of-flight detector, electromagnetic calorimeter

The high-threshold Cherenkov counter (HTCC) [65] is a Cherenkov detector (a description of the Cherenkov effect and the principle of Cherenkov detectors is given in section A.3.4) de-

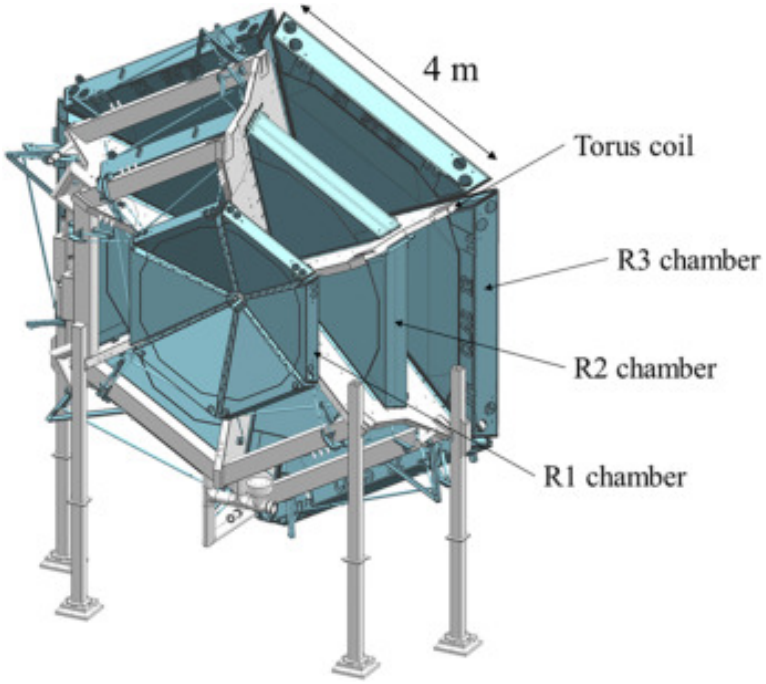

Figure 2.9: Diagram of the DC (in blue) and the torus magnet (in grey): R1, R2 and R3 correspond to the three regions [64].

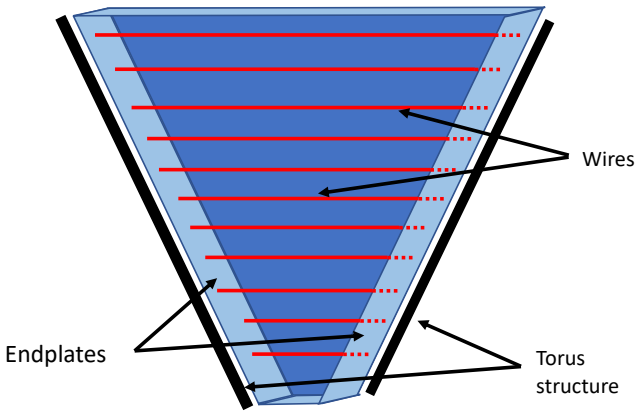

Figure 2.10: Diagram of a DC sector showing how the wires are strung between the two endplates. The stereo angle is not shown here.

signed to identify electrons by providing pion rejection for momenta below 4.9 GeV/c. The gas used in the HTCC for the production of Cherenkov light is CO_2, providing a 15 MeV threshold for the detection of electrons and a 4.9 GeV threshold for pions. The HTCC is made of 48 mirrors that focus the light produced by charged particles onto PMT windows (see figures 2.12). Positioned as the first detector of the forward region (and in particular before the DC), the HTCC is made with low-density materials to minimize multiple scattering and energy losses. In order to maximize the active area of the HTCC and to avoid high density areas in the center of the detector, mirrors and PMTs are positioned at the edges of the sectors, near the torus coils. The HTCC is playing a major part in the trigger system thanks to its ability to send a fast signal for

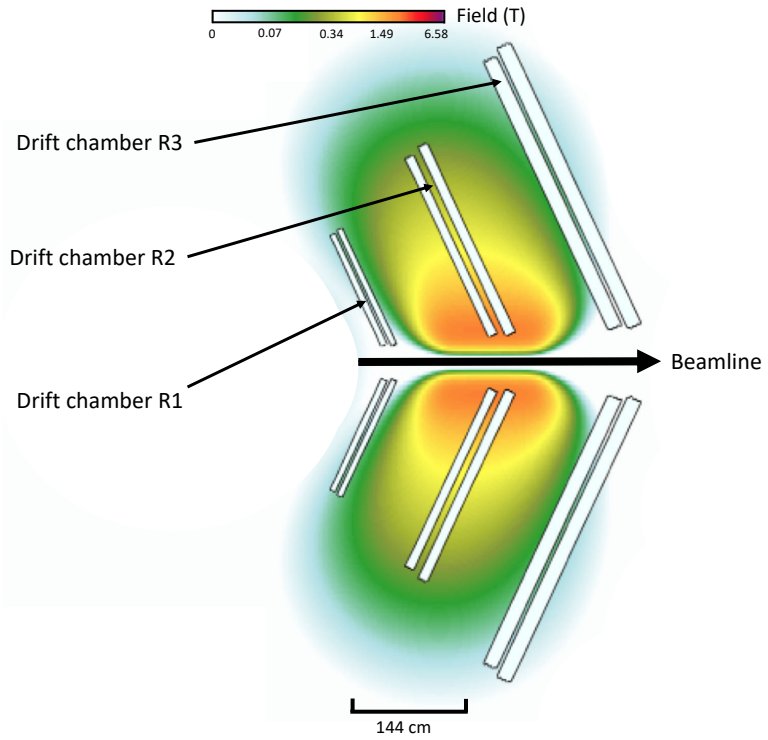

Figure 2.11: Intensity of the absolute torus magnetic field for the different DC regions (R1, R2 and R3 correspond to regions 1 to 3).

the scattered electron.

In comparison, the low-threshold Cherenkov counter (LTCC) [66] is designed to separate pions from kaons for momenta between 3.5 GeV/c and 8.5 GeV/c. With the use of C_4F_{10} gas, the threshold for the detection of pions is 3.5 GeV/c and the threshold is 8.5 GeV/c for the detection of kaon.

The forward time-of-flight [67] provides time-of-flight measurements (the time-of-flight technique is briefly described in section A.3.6) in the forward region. It is the main detector used for the separation of charged particles with up to about 5 GeV/c. However, the precision of the separation decreases with the momentum of the particles, as illustrated in the analysis (on figure 4.2). The FTOF is able to perform a π/K separation up to 2.8 GeV/c momenta, 4.8 GeV/c for the K/p separation and 5.4 GeV/c for the π/p. The time-of-flight technique is applied between the time measured by the FTOF and the start time calculated by the trigger system. The FTOF is also made of six sectors, and each sector is divided into three sets of plastic scintillators: panel 1-a, panel 1-b and panel 2, as highlighted on figure 2.13. In each panel, rectangular scintillator counters are assembled and read out by PMTs. Panels 1-a and 1-b both cover polar angles 5° to 35° and contain 23 and 62 counters per region, respectively (panel 1-a is made of refurbished counters from CLAS while panel 1-b are new scintillators). Panel 2 is formed of five wide scintillators per sector covering polar angles 35 to 45° for the identification of low momentum outbending particles.

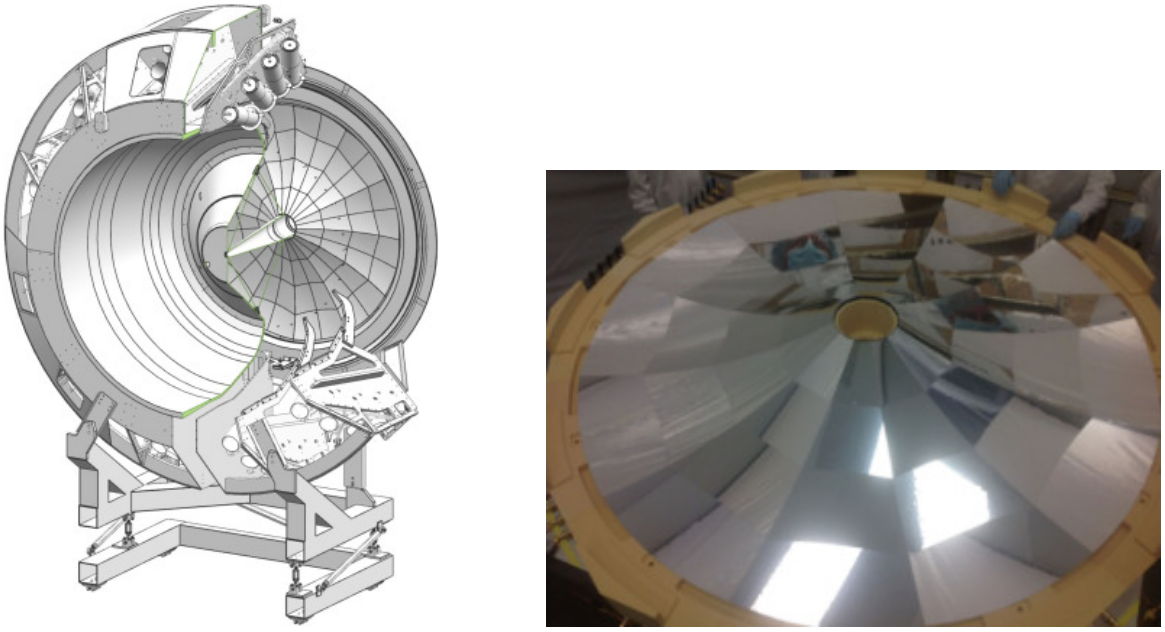

Figure 2.12: Diagram of the HTCC and photo of its mirrors [55].

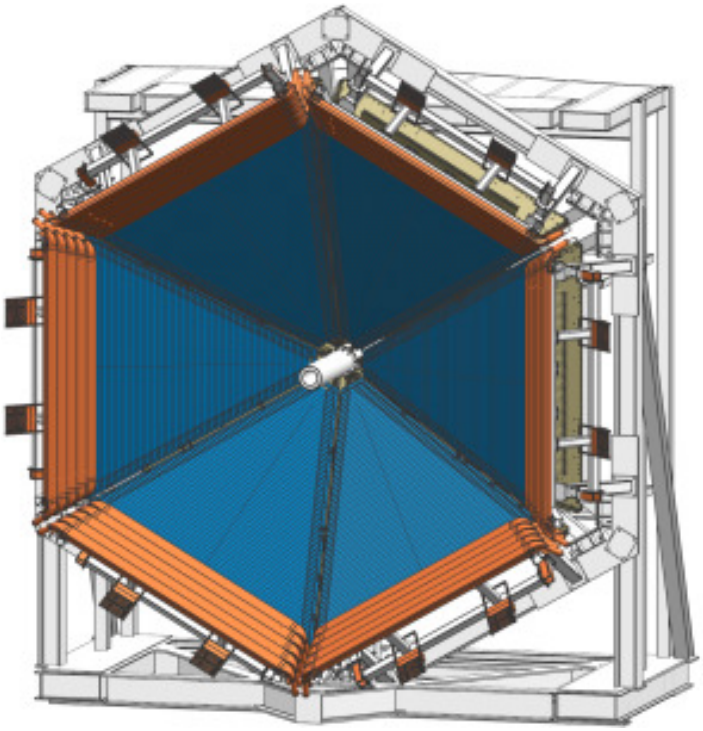

Figure 2.13: Diagram of the FTOF [67]: in blue are highlighted panel 1-b scintillators and in orange panel-2 sincillators, panel 1-a scintillators are not represented here.

The electromagnetic calorimeter (ECAL) [68] is a sampling calorimeter located at the very downstream end of the forward detector. The ECAL is made of the CLAS electromagnetic calorimeter (EC) to which was added a pre-shower calorimeter (PCAL) in order to entirely absorb the shower for high-energy electrons and to provide a good reconstruction of photons from high-momentum π^0 decays. PCAL and EC are also organized in six identical sectors, each

sector consisting of layers of scintillators separated by layers of 0.2 cm-thick lead. 15 layers of scintillator are used in each PCAL sector and a total of 39 in the EC. The scintillators are segmented to form strips, read out by PMTs. The strips are 10 cm-wide in the EC, while, in the PCAL, the strips are 4.5 cm-wide but roughly half of the PCAL strips (called "double strips") are coupled two-by-two to a single readout channel leading to 9 cm-wide effective strips. The scintillators in PCAL and ECAL are organized in three different types of layer, called U, V and W layers, with three different strip orientations (see figure 2.14). Clusters are reconstructed when a signal is detected at the intersection of the three layers U, V and W.

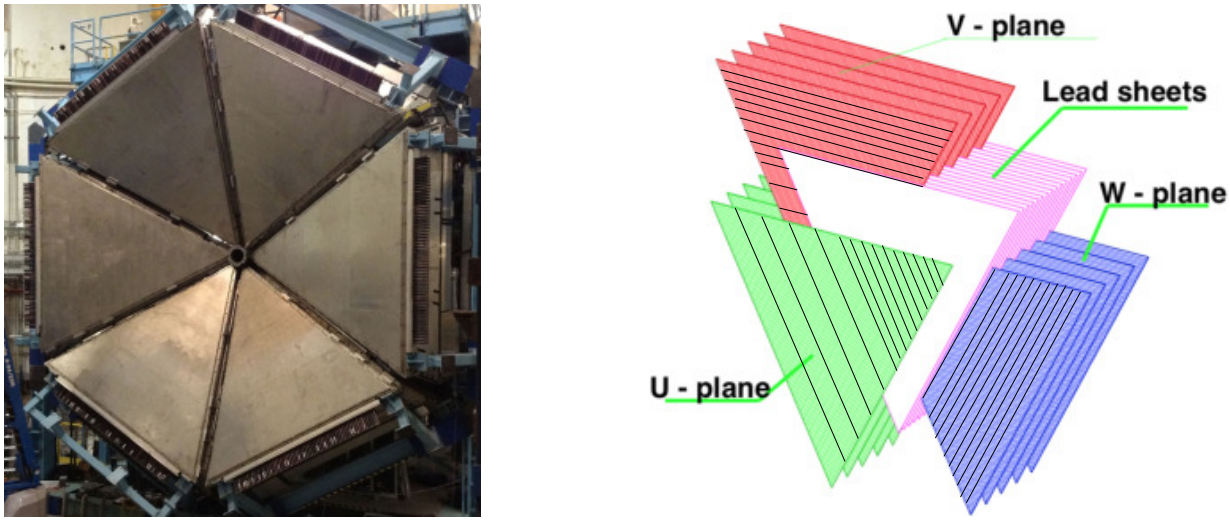

Figure 2.14: Forward electromagnetic calorimeter. Left: photo of the PCAL in front of the EC [55]. Right: diagram of the lead and scintillator layers [68], highlighting the U, V and W layers (the direction of the strips is represented here to illustrate the description of the calorimeter).

2.3.3 Forward tagger

The forward tagger (FT) [69] consists of an electromagnetic calorimeter, a scintillation hodoscope and a Micromegas tracker (see figure 2.15). The FT is placed inside the forward detector, around the beamline, between the HTCC and the torus magnet. It is designed to identify electrons and photons for polar angles between 2° and 5°.

Forward tagger calorimeter

The FT calorimeter consists of 332 cooled lead tungstate ($PbWO_4$) crystals. The 332 paralellepipedic 20 cm $\times$ 15 mm $\times$ 15 mm crystals, arranged along the beamline, are wrapped together to form a ring of $\simeq$30 cm diameter. The scintillation light produced by the crystals is collected by avalanche photodiodes and amplified before being read out by an analog-to-digital converter.

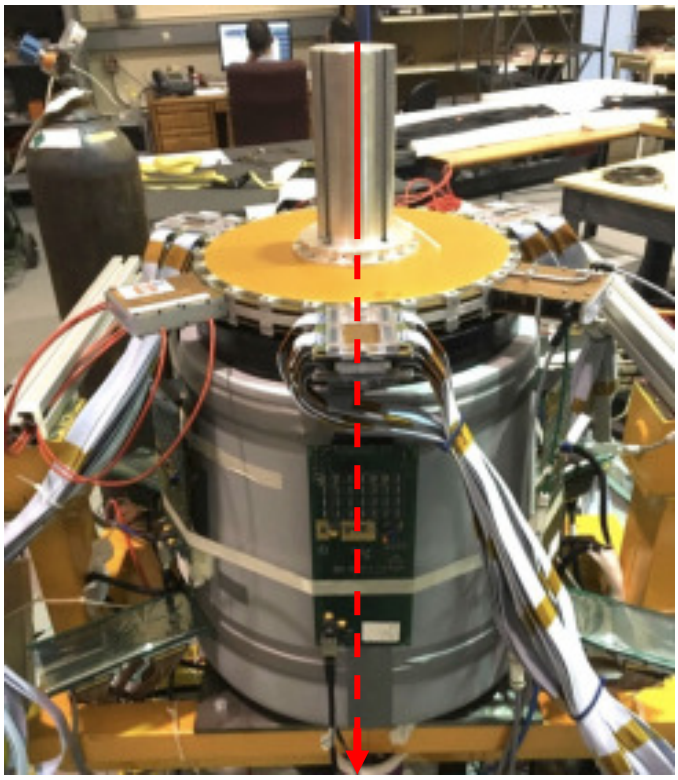

Figure 2.15: Photo of the forward tagger before installation in CLAS12 [69]. The FT calorimeter is at the bottom the hodoscope in the middle and the tracker is at the top. The red line corresponds to the direction of the beamline.

Forward tagger hodoscope

The forward tagger hodoscope is used to separate electrons, that will induce a hit in both the hodoscope and the FT calorimeter, from photons, that will only be detected in the calorimeter. The hodoscope consists of two layers of 116 plastic scintillators each, connected to photomultipliers by 5 m-long optical fibers. The scintillators are 7 mm thick for the upstream layer and 15 mm thick for the downstream layer and a 9 mm clearance is used behind each layer to position the optical fibers. One hodoscope layer is shown on figure 2.16.

Forward tagger tracker

The forward tagger tracker is designed to provide a precise measurement of the electrons' scattering angle. The tracker uses the Micromegas technology, described in detail in chapter 3. The FT tracker consists of two double-layers of strip Micromegas detectors and is positioned upstream of the hodoscope. For each double-layer disk, the strips of the first layer are oriented perpendicularly with respect to the second to provide a two-dimensional information in the plane transverse to the beam axis. The expected spatial resolution is between 100 μm and 200 μm. The readout electronics are placed off-detector, using micro-coaxial cable assemblies to connect the detectors and the front-end electronics. A view of the tracker is shown on figure 2.17.

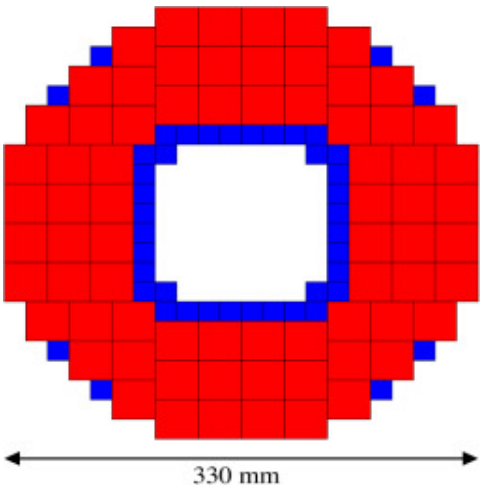

Figure 2.16: Schematic of one layer of scintillator blocks in the forward tagger hodoscope [69]. Red blocks are 30 mm large while blue ones are 15 mm large.

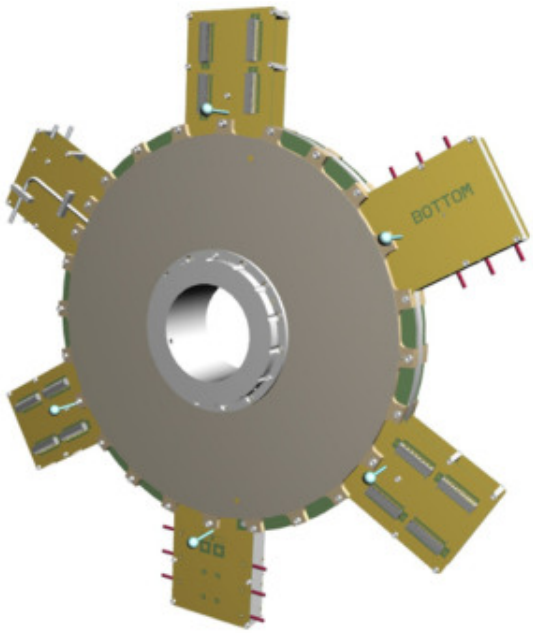

Figure 2.17: Schematic of the forward tagger tracker: the two double-layer disks are attached to each other [69]. The active area is colored in grey, and the six rectangles attached to the flanges contain the connectors for the coaxial cables.

2.3.4 CLAS12 data acquisition and software

Data acquisition

The CLAS12 data acquisition system can run at a trigger rate of 15 to 20 KHz, with a lifetime above 90% and a data rate of 0.5 to 1 GB/s [70]. A set of trigger rules to select different physics topologies have been developed. The electron trigger, which accounts for about half of the events recorded during physics data taking, requires an electron reconstructed in one of the six sectors of the forward detector (this is the trigger used in this analysis, see chapter 4). One quarter of the

events comes from the forward tagger trigger, in which one electron is required in the forward tagger and additional charged particles are required in the forward detector. The remaining fraction comes from monitoring triggers or physics topology triggers largely pre-scaled (with only a limited fraction of events being recorded).

Monitoring and remote control software

To ensure the proper functionning and safety during data taking, the shift crew is continuously monitoring the beam, beamline and DAQ status, as well as checking the data quality. To achieve this, beam conditions, detector parameters and status are continuously recorded and are made available, in real time, to the shift personnel, as shown on figures and 2.18 and 2.19. This also provides remote control on the beamline and detector parameters, such as the movement of harps for beam tuning or the detector voltages.

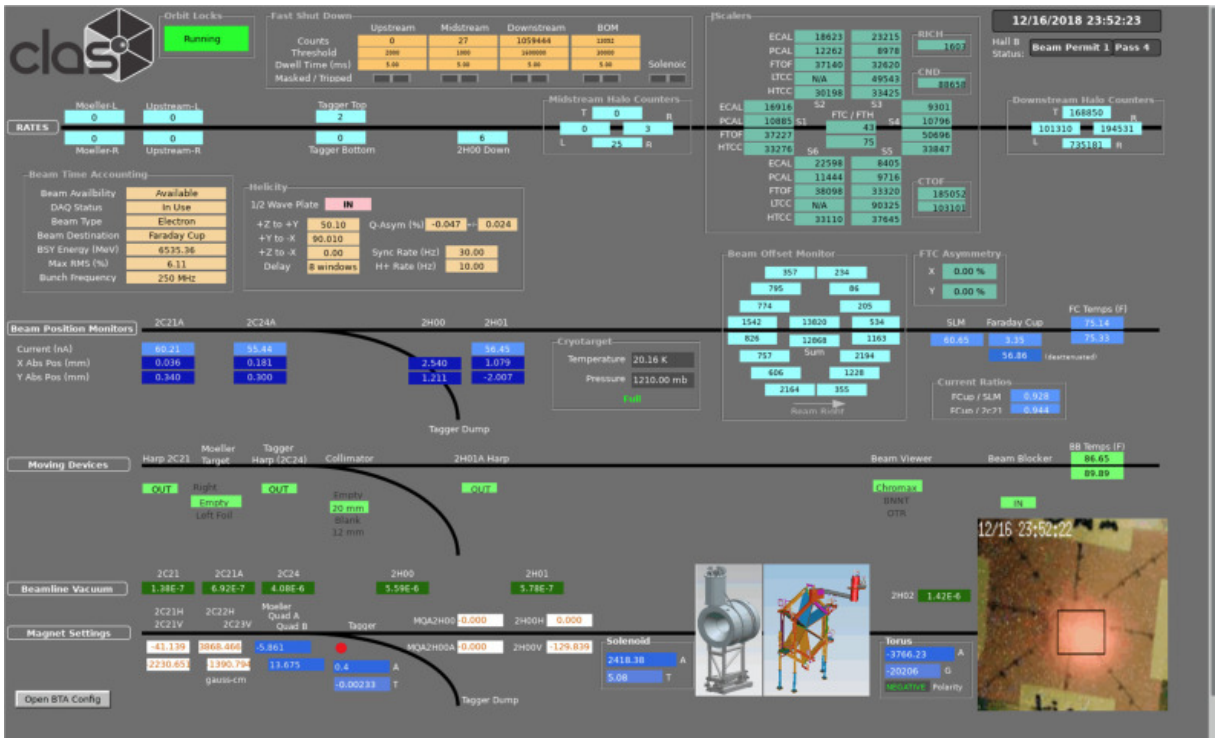

Figure 2.18: Beamline overview [55] used by the shift personnel, showing beam position and current, beam halo counter rates, fast shutdown system settings, target information, etc.

The CLAS12 monitoring suite is used both online by the shift crew and offline by detector experts to identify any issue with the behavior of detectors [71]. It displays high-level information on raw or reconstructed data files such as hit occupancies, detectors hitmaps, cluster sizes or time distributions, as shown on figure 2.20. The design and development of the MVT monitoring suite was part of the work done by the author and is detailed in chapter 3, section 3.2.3.

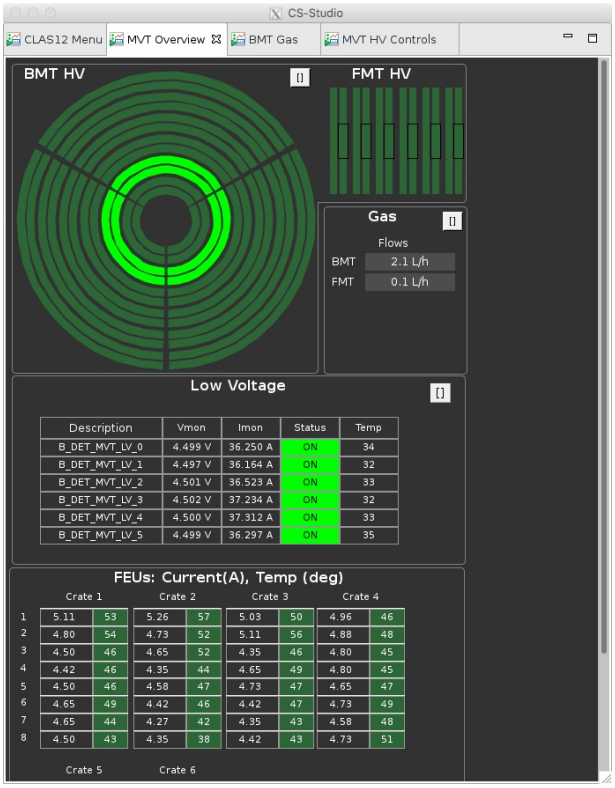

Figure 2.19: Micromegas Vertex Tracker remote control overview. The top panel is a graphical representation of the high voltages, the gas flows are summarized on the right and the electronics status is shown in the middle and the bottom panel.

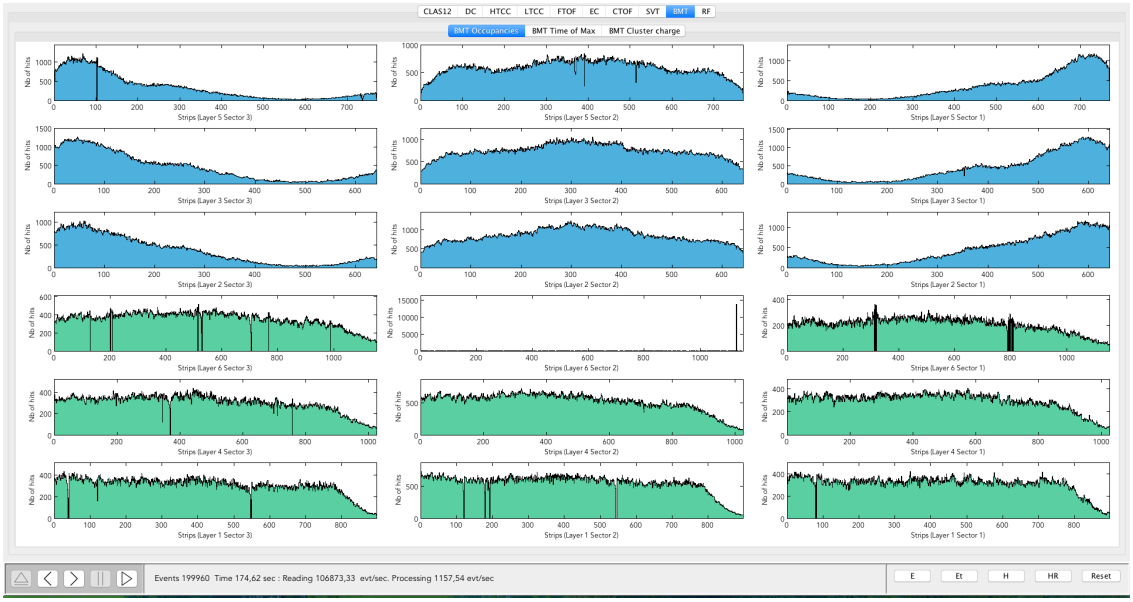

Figure 2.20: View of the occupancies for the Barrel Micromegas Tracker from the monitoring suite. The 18 histograms represent the different tiles organized by sector and layer number, and for each histogram the x-axis is the strip number (more information is given in chapter 3).

CLAS12 event display

The CLAS12 event display (CED) tool [71] is a software mainly used to visualise reconstructed data event by event. It provides a precise graphical description of the detectors, the position of

the hits, clusters and reconstructed trajectory of the particles, for each event (see figure 2.21). This tool is very useful for detector experts to identify reconstruction issues or general issues with the detectors.

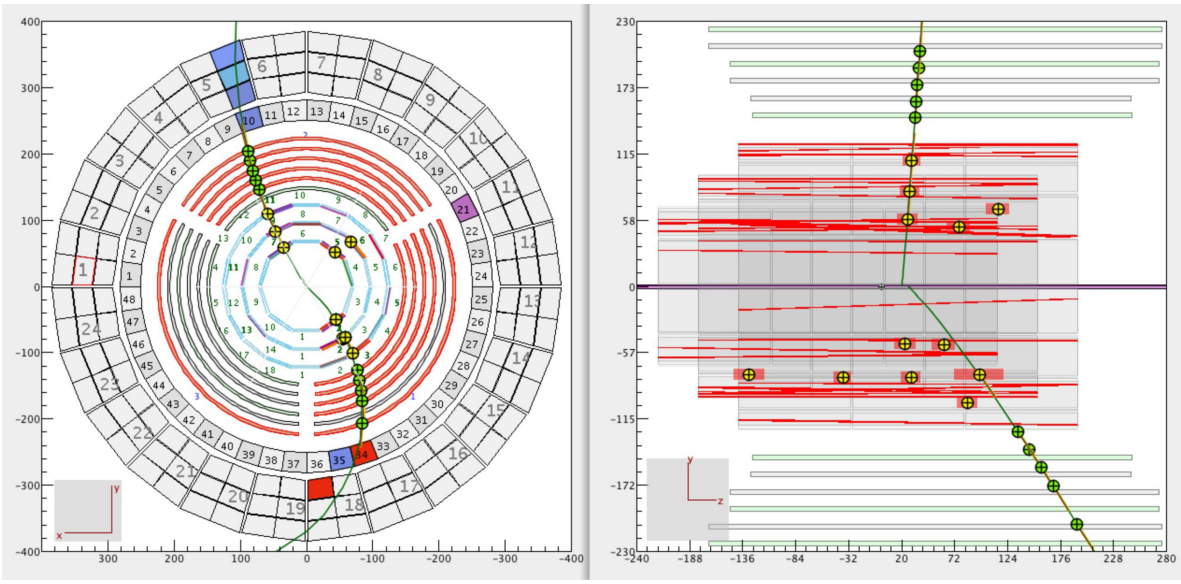

Figure 2.21: View of one event in the central detector using the CLAS12 event display (CED), on the left in the plane transverse to the beamline and on the right in a plane parallel to the beamline. On the left are visible from inside to outside: the SVT, the BMT, the CTOF and the CND while on the right only the SVT and the BMT are visible. The small circles represent the position of the hits and the green lines represent the reconstructed trajectory of the particles.

Simulation software: GEMC

A simulation framework, called GEant4 Monte-Carlo (GEMC), was developped to perform physics simulations of the CLAS12 spectrometer. GEMC is based on the Geant4 simulation software [72], which simulates the passage of particles through matter. A precise description of all the CLAS12 detectors was implemented, allowing to test the behavior of particles going through the CLAS12 spectrometer. With the use of event generators, reproducing physical processes, GEMC can also provide estimations of measurements with the CLAS12 spectrometer. A simulation of DVCS and π^0 electroproduction, using the GEMC framework, is described in section 4.1.3.

Chapter 3

Micromegas detectors for CLAS12

Micromegas detectors [73] are used as trackers in the CLAS12 spectrometer. The Micromegas Vertex Tracker (MVT) consists of a Barrel Micromegas Tracker (BMT) that improves the tracking in the central region and a Forward Micromegas Tracker (FMT) that complements the drift chambers in the forward region. Finally a forward tagger tracker (FTT) provides tracking in the forward tagger region. Micromegas detectors were built and tested at CEA Saclay (France) before being installed at Jefferson Lab.

In this chapter, the general principle of Micromegas detectors is detailed, followed by a description of the Micromegas-based detector systems used in the CLAS12 experiments. The assembly of the Micromegas detectors and their integration with the CLAS12 spectrometer in Hall B are then explained. Finally the commissionning of the Micromegas detectors is described. The work on Micromegas detectors done by the author of this thesis is mainly described in section 3.2 and 3.3 (a detailed list is given in appendix, section A.4).

3.1 Description of the detectors

3.1.1 Principle of Micromegas detectors

Micromegas detectors are gaseous detectors, they are designed to detect charge carriers created by ionization of the gas from incoming charged particles.

Micromegas detectors (see figure 3.1) are based on the separation of the gas volume into a large conversion area and a thin amplification area. The conversion gap is a few millimeters thick and is subject to a few kV/cm electric field while the amplification gap is only roughly 100 μm wide and subject to a strong electric field (up to several hundreds of kV/cm). The separation of the volume is done by a metallic micro-mesh. Primary electrons created by the ionization of the gas in the conversion area drift toward the amplification area. Because of the electric field ratio in the two regions, narrow drift field lines are formed along the micro-mesh holes, called the funnel effect, allowing most of the electrons to go through the micro-mesh. The fraction of

electrons that crosses the micro-mesh is called the micro-mesh transparency, it is usually higher than 95% when the electric field difference between the conversion and amplification regions is large. When the electrons reach the amplification gap, the electric field is such that an avalanche effect occurs: primary electrons acquire enough energy between collisions to create further ionizations. Electrons are quickly collected by the strips, and ions drift towards the micro-mesh. Because of the funnel effect created by the field difference, the large majority of ions do not reach the conversion gap and are collected by the micro-mesh. A measurable signal is induced on the strips by the drift of the charges in the amplification area.

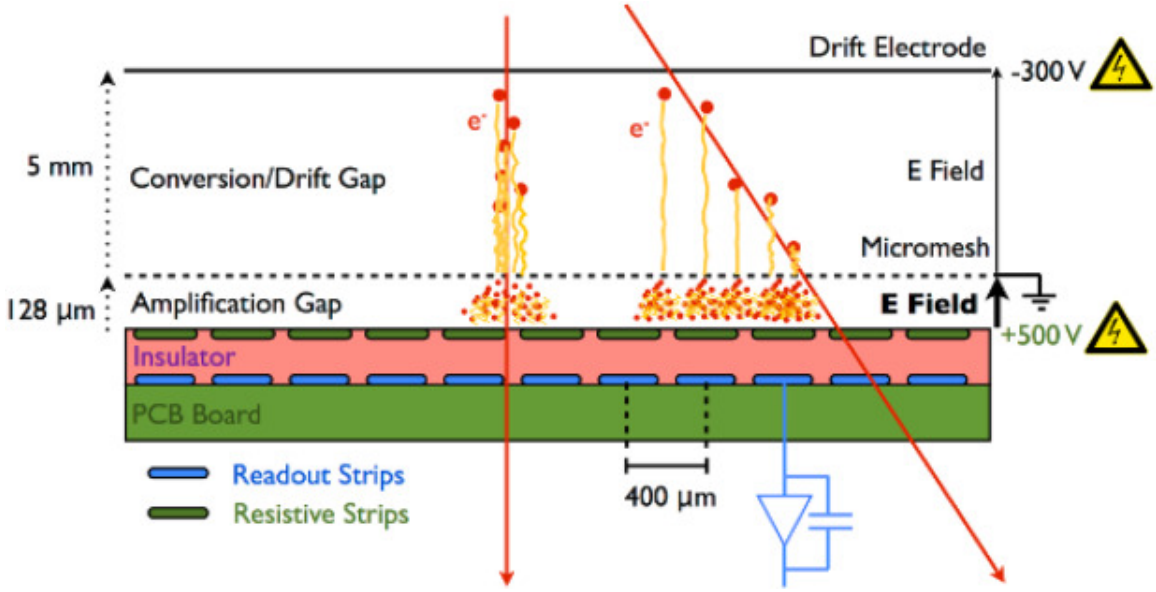

Figure 3.1: Schematic of a Micromegas detector [61]

Strip Micromegas detectors use parallel strips and therefore only provide one-dimensional information about the incoming particle (as opposed to pixel detectors that provide two-dimensional information). The distance between the strips is called the pitch and is directly related to the spatial resolution of the detector. Strip detectors are generally arranged in layers with different orientations of the strips.

With their thin amplification gap, leading to a fast evacuation of charges, Micromegas are designed to sustain high flux (at least several hundreds of kHz/cm^2). Micromegas detectors can achieve detection efficiencies higher than 95% and spatial resolutions below 100 μm. However, energy resolution is generally not good enough to perform particle identification.

In order to have an overall uniformity of the detectors (and, in particular, a uniform gain), bulk technology [74] is used for all CLAS12 Micromegas detectors, in which the manufacturing process is designed to keep the strips and micro-mesh at a constant distance.

Due to the high electric field, discharges between the strips and the micro-mesh are known to occur in Micromegas detectors in nominal running conditions. These discharges lead to the formation of currents between the strips and the micro-mesh, voltage drops and sparks. Even if this does not provoke early ageing, voltage drops cause inefficiencies for a few ms. In order

to limit the impact of sparks, resistive technology [75] is used for all CLAS12 Micromegas detectors. Resistive Micromegas have an extra insulator layer above the readout strips, on top of which resistive strips are deposited (with the same pattern as readout strips). Signals on the readout strips are induced from the resistive strips by capacitive coupling.

Finally, the choice of the gas mixture plays an important role in the design of Micromegas detectors. Noble gases are often used: they do not chemically react with the detector itself and provide relatively high gains. However noble gases lead to unstable amplification and are generally mixted with polyatomic gases to stabilize the amplification.

3.1.2 Barrel Micromegas Tracker (BMT)

The BMT is designed to improve tracking in CLAS12 central region. In particular, combined with the SVT, it improves the central vertex tracker (CVT) vertex and polar resolutions (see section 2.3.1). It is positioned inside a 5 T solenoidal magnetic field, between the SVT and the CTOF.

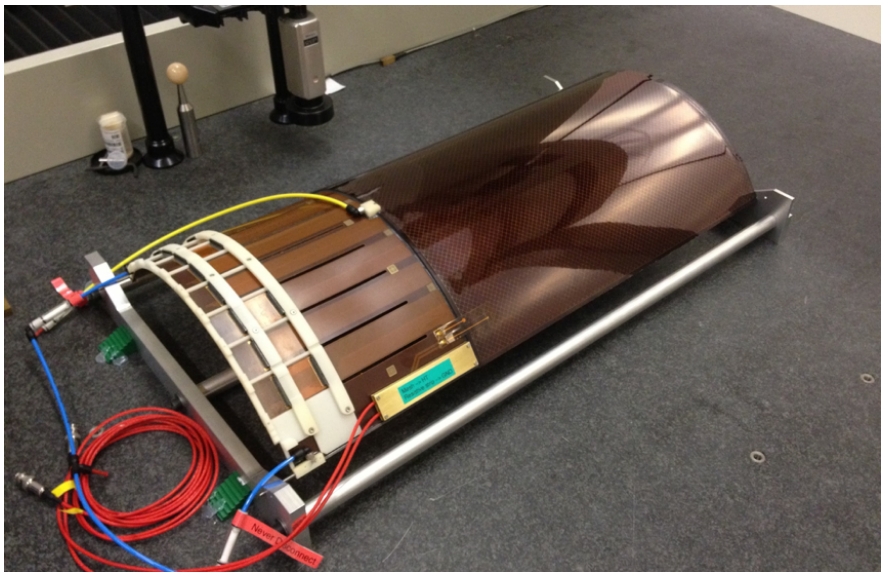

Figure 3.2: Photo of a BMT tile: the active area is the dark brown zone, the light brown at the bottom left is the mechanical structure on which the readout electronics are connected (inside the white slots). High voltage from the power supply is provided by the red cable and gas is continuously flowing, entering the detector through the yellow pipe and being extracted through the blue pipe.

The BMT consists of 18 curved resistive bulk Micromegas detectors, called tiles (see figure 3.2). Tiles are organized in six cylindrical layers divided in three sectors covering approximately 115° each. Layers are arranged with different strip orientations to provide two-dimensional information: Z layers have strips along the beam axis providing information about the azimuthal angle of incoming particles while C layers have circular strips perpendicular to the beam axis and provide information about polar angles. The second, third and fifth layers are Z layers and

the first, fourth and sixth layers are C layers (the first layer being the most inner one). The number of strips and the pitch are adjusted to cover the entire active area: C layers have more strips than Z layers and the number of strips tends to increases with the radius with the constraint that the number of strips is a multiple of 64 to match the readout electronics. For C layers, the pitch varies within a tile to keep the angular resolution constant for particles coming from the vertex. Details about BMT layers are listed in table 3.1.

Layer	Radius	Pitch (μm)	Number of strips	Strip orientation
1	146	330 - 860	896	C
2	161	487	640	Z
3	176	536	640	Z
4	191	340 - 770	1024	C
5	206	529	768	Z
6	221	330 - 670	1152	C

Table 3.1: Radius, pitch, number of strips and strip orientation for each BMT layer.

3.1.3 Forward Micromegas Tracker (FMT)

The FMT is designed to provide vertex tracking in the CLAS12 forward region. It is the first detector in the forward region, in front of the HTCC and about 35 cm downstream of the target. The FMT is positioned on the downstream end flange of the BMT (see figure 3.3), inside the 5 T solenoidal magnetic field.

The FMT consists of a stack of six resistive bulk Micromegas disks (as shown on figure 3.4). The six disks are all identical, but with different strip orientation, each disk making a 60° angle with its neighbors. Each disk has 1024 strips, a 525 μm pitch. Micromegas detectors have a diameter of 450 mm and their active area of FMT detectors is segmented into two independent parts: an inner part with diameter between 86 mm and 166 mm and an outer part with diameter between 168 mm and 380 mm. The inner part can therefore be turned off or set at a lower amplification voltage when the particle flux is very high.

3.1.4 Forward Tagger Tracker (FTT)

The FTT is designed to provide tracking for very forward electrons sent in the forward tagger (see section 2.3.3). The FTT is positioned upstream of the forward tagger hodoscope.

The FTT design is very similar to the FMT one, it consists of four disks arranged in two double-layers (see figure 3.5). Each disk of each double-layer has its strips oriented perpendicularly to its neighbour. Each disk has 768 strips and a 500 μm pitch.

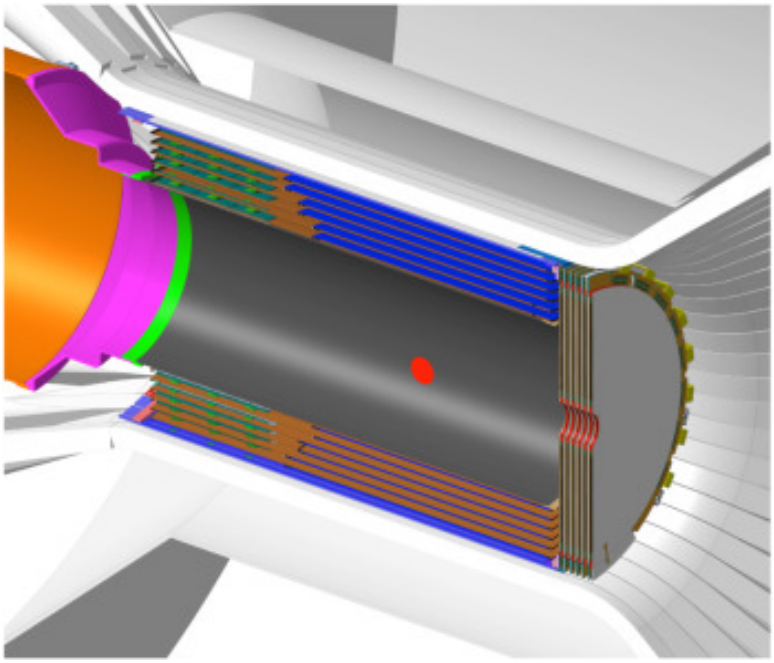

Figure 3.3: Schematic of the MVT [61] with the six layers of BMT (with their active area shown in blue) and the six FMT disks (with their active area shown in grey). The MVT is shown inserted in the CTOF and the solenoid magnet. The SVT, positioned inside the BMT, is not represented here. The electron beam enters from the left and reaches the target position at the red dot.

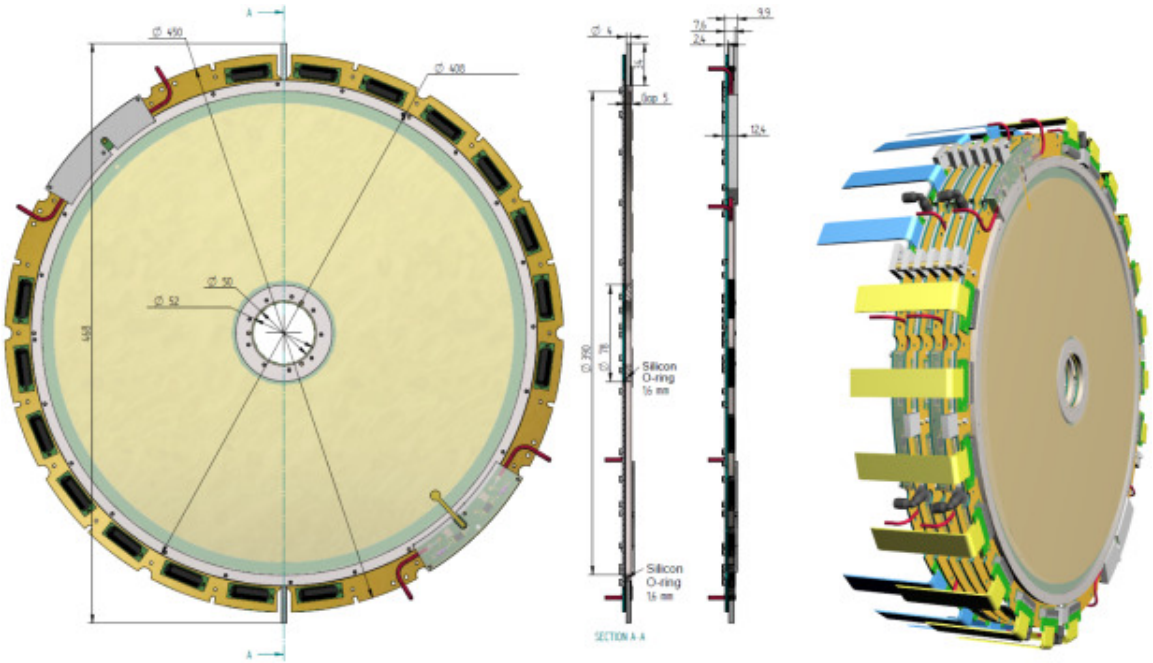

Figure 3.4: Schematic of the FMT [61]: one disk is shown on the left (with the active area in yellow, readout connectors in black and high-voltage cables in red), and the stack of six FMT disks is shown on the right (readout cables in blue and yellow, high-voltage cables in red and gas entrance and exit in black).

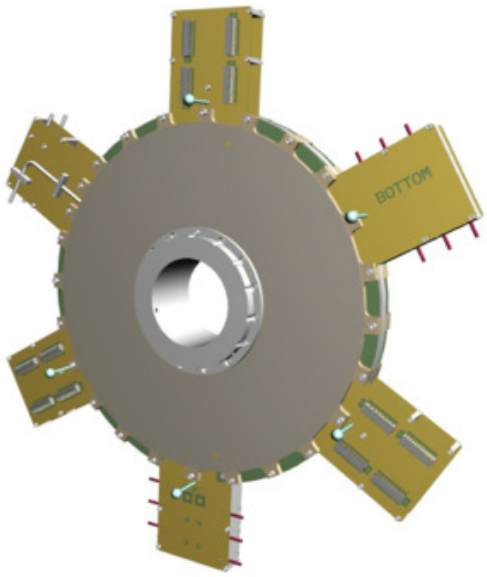

Figure 3.5: Schematic of the FTT [69]: the two-double disks are attached to each other, the active area is shown in dark grey. In the edges of each disk, six extensions are added to contain connectors for the readout electronics, gas and high voltages. The six extensions are designed to be outside of other detectors' acceptance: their position corresponds to the mechanical structure of the torus.

3.1.5 Gas system

Micromegas need a homogeneous gas flow in their active area and a constant gas pressure to keep the gain uniform, avoid deformations and overcome the outgassing of the detectors. A gas circulation loop is designed to keep the detectors continuously flushed.

The gas mixing system unit is installed outside of the hall and is used to create the gas mixture. The mixtures are then sent inside the experimental hall and distributed to the detectors, before being released outside of the experimental hall, as shown on figure 3.6. Two programmable logic controllers (PLC) manage the gas flow in the MVT and the FTT. The PLC also measures flow rates and pressure at different points and can trigger alarms or interlocks if needed, to avoid damaging the detectors and stop potential gas leaks.

The gas flow in each detector is kept between 1 and 2 l/h. Six independent gas lines are used for the BMT, one for each layer, with tiles inside a layer connected in series. Two lines are used for the FMT, with disks connected in series in sets of three, and two lines are used for the FTT. The total gas flow inside the BMT, the FMT and the FTT can be controlled remotely using the PLC. The flow inside each line can be visualised and adjusted manually.

The choice of the gas mixture is a trade-off between gain, stability, transverse diffusion, drift velocity and cost. A mixture with 90% argon and 10% isobutane (iC_4H_{10}) was found to be the best for the BMT to reach high gain, reduce the transverse diffusion and decrease cost. Since the MVT is inside the solenoid magnet, the charge carriers produced during ionization are subject to the Lorentz force caused by the magnetic field. Since this Lorentz force is transverse to the

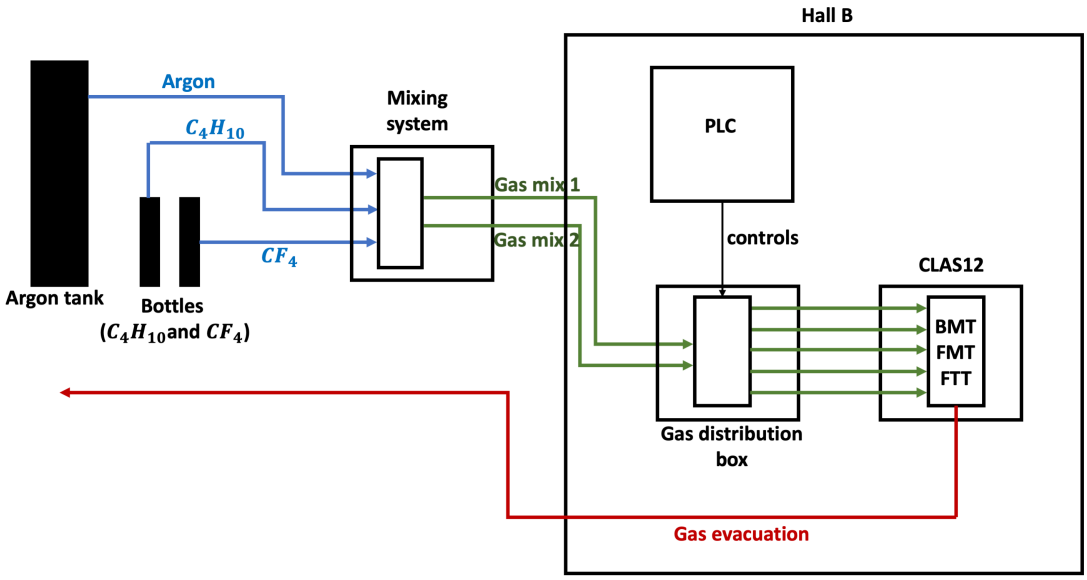

Figure 3.6: Overview of the gas distribution system for the BMT, FMT and FTT.

direction of the strips for the BMT Z layers, the reconstruction for these Z layers is affected, the charges being spread over several strips. The use of argon and isobutane reduces the effect of the Lorentz force by reducing the drift velocity and consequently improves the spatial resolution (the effect of the magnetic field on the drift of the charge carriers and is defined and estimated more precisely in section 3.3.3). For the FMT, and the FTT, the gas mixture is made of 80% argon, 10% isobutane and 10% tetrafluoromethane (CF_4), the addition of CF_4 being used to improve the timing resolution by increasing the charge carriers' drift velocity.

3.1.6 Readout electronics

The MVT electronics are designed to read more than 20,000 channels, with an up to 20 kHz trigger rate and a timing precision of a few ns. Charge is measured on a 10-bit range which is sufficient for all Micromegas signals. The data acquisition system is divided into front-end and back-end electronics.

Front-end electronics

Signal amplification, shaping, digitization, compression and association of the signal with a trigger are done by the front-end electronics, in the front-end units (FEUs). Each FEU (see figure 3.7) is mainly composed of 8 application-specific integrated circuits (ASICs), an 8-channel flash analog-to-digital converter (FADC) and a field programmable gate array (FPGA) that controls the ASICs and the ADC. The front-end electronics are also constrained by the very limited space available in the barrel region, as well as the very high magnetic field in the area. A specific

ASIC called DREAM (dead-timeless readout electronics ASIC for Micromegas) was developed to meet the challenges posed by the MVT. For each readout channel, signals are constantly processed and stored in the DREAM in a switched capacitor array at a rate of up to 50 MHz, this is read by the FPGA only if a trigger signal is received. The FPGA also apply corrections such as pedestal equalization, coherent noise subtraction and zero suppression (defined below). The coherent noise is estimated, chip by chip, by taking the median value of the noise for the channels of each chip and this coherent noise is subtracted at the DREAM level. A zero suppression algorithm is used to reduce the amount of data recorded by Micromegas electronics (to avoid recording noise). For each channel, a threshold is defined based on the average level of noise and only signals above this threshold are recorded. Because of the limited space available and the high magnetic field, front-end crates containing the front-end units are deported about 1.5 m upstream, and are able to operate within the residual magnetic field. The connection with the detectors is done with a micro-coaxial cable with low 40 pF/m linear capacitance. Each FEU is powered with 4.5 V low voltage and consumes about 6 A. Traditional cooling is not possible in the solenoid magnetic field, therefore cooling is provided by fans located about 2 m upstream and connected to the FEUs by plastic pipes.

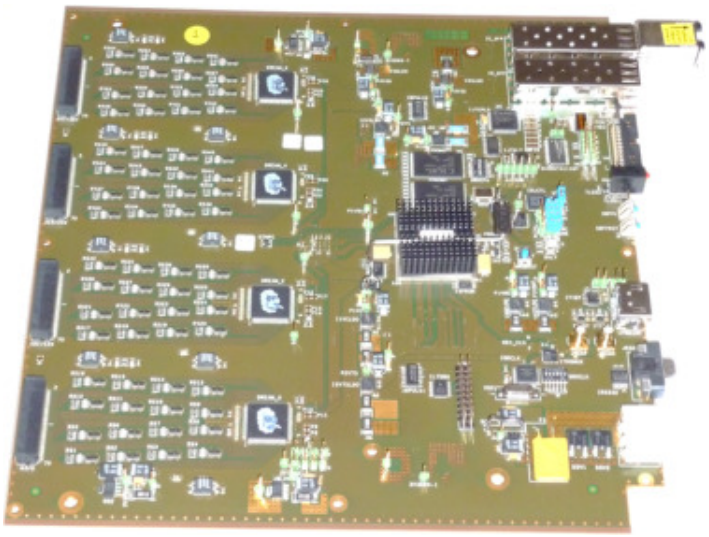

Figure 3.7: Picture of an FEU [61]. Four DREAM chips are visible at the center of the FEU (the other four being on the other side).

Back-end electronics

Signals from the FEUs are then sent towards the back-end unit via optical links. The back-end is in charge of gathering signals from the different FEUs and grouping them by event. It is also responsible for the interactions with the rest of the CLAS12 electronics, such as the event building and the trigger systems. Two back-end units (BEUs) are used for the MVT.

The data acquisition system used for the FTT is similar to the MVT one. The MVT and the FMT systems are totally independent.

3.2 Detector assembly and integration

3.2.1 MVT assembly and integration with the SVT and the CLAS12 system

A first partial assembly was performed at CEA Saclay before shipment. One sector of the BMT was assembled to test the mechanical structure, cabling and overall assembly process.

Once shipped to Jefferson Lab, the MVT was assembled in summer 2017 in a clean room. Assembly of the BMT was done sector by sector starting from inner layers. The readout cables were positioned first, followed by high-voltages and gas distribution cables. FEUs were connected to the BEUs and powered by low voltages.

The MVT was then integrated with the SVT (see figure 3.8). After performing a geometrical survey of the two detectors, the SVT was inserted in the MVT mechanical support. After connecting the back-end units of the two detectors, common data taking could be performed. Some faulty elements (such as optical fibers) were identified and replaced and first tracking was done using cosmic ray data.

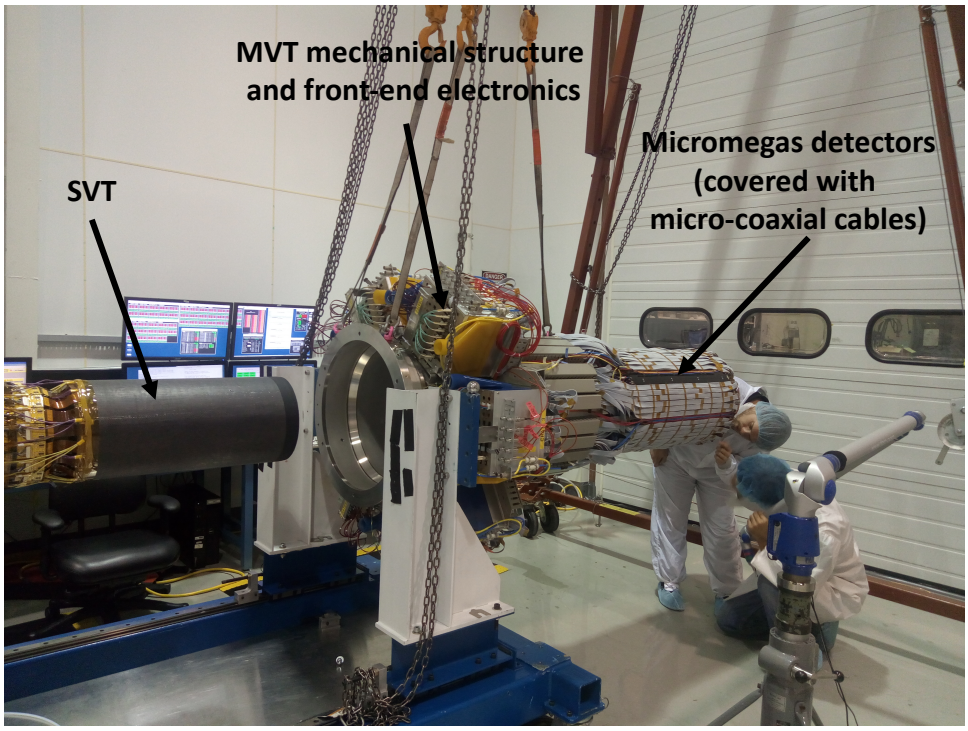

Figure 3.8: Photo of the assembly of the CVT: the SVT (on the left) is inserted in the MVT strcture (on the right).

Finally the whole CVT was moved into the hall B at the end of the year 2017 (see figure 3.9). A crane was used to move the unit formed by the MVT and the SVT on a mobile cart. The cart could be inserted in or out of the CTOF/CND to access the MVT. The gas distribution box and cooling system were installed on the cart. The high voltage power supply, gas controller and

BEUs were installed on a rack a few meters away from the cart and connected with the rest of the CLAS12 system.

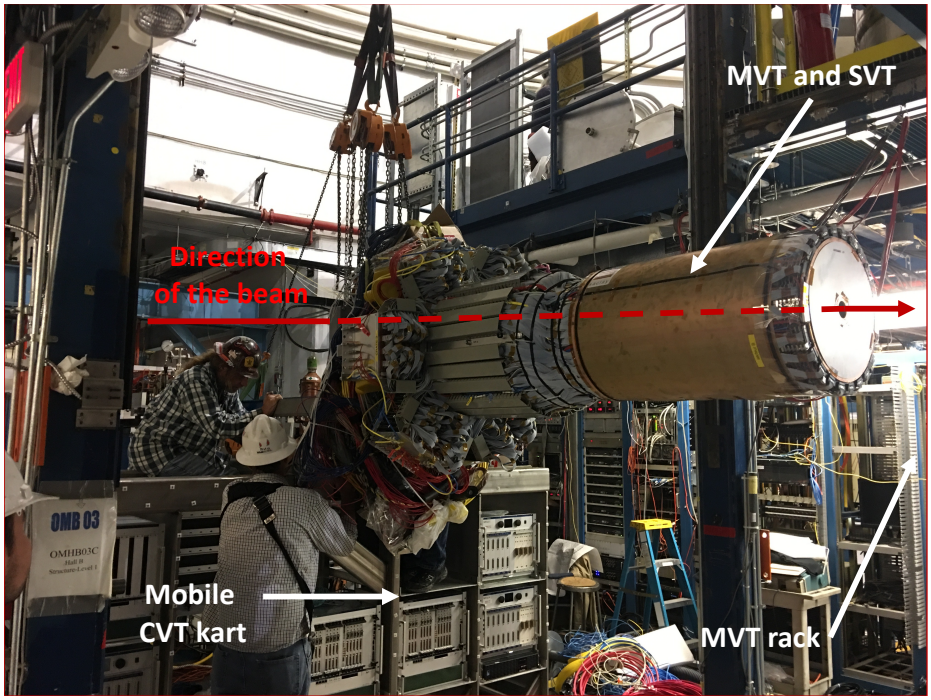

Figure 3.9: Photo of the installation of the CVT on the CVT mobile cart in hall B, using a crane. The MVT rack is at the right, behind the detectors, barely visible in this picture.

3.2.2 Gas system integration

For safety reasons, and, in particular, because isobutane is a flammable gas, the gas bottles are placed outside of the hall. A gas line connects the bottles to the gas distribution box on the CVT cart.

Due to delays, the gas mixing system was not ready at the start of data taking: premix bottles were used. Premix bottles had to be replaced roughly every two days. The mixing system was built in spring 2018. It consists of two independent lines, one line for the BMT (with 90% argon and 10% isobutane) and one line for the FMT and the FTT (with 80% argon, 10% isobutane and 10%) as show on figure 3.10.

Isobutane has a boiling point around $-11°C$ at atmospheric pressure. In winter, isobutane started to condensate in the pipes in the mixing system unit and in the mass flow controllers. To avoid the formation of liquid, pipes have been wrapped with heating tape.

After circulation of the gas in the detectors, an exhaust line is used to eject the gas ouside of the hall. It was found that pressure waves induced by the wind outside of the hall were propagating to the detectors through the exhaust pipes, triggering the interlock systems to protect the detector in case of excessive pressure. The impact of wind was largely reduced by protecting the gas evacuation.

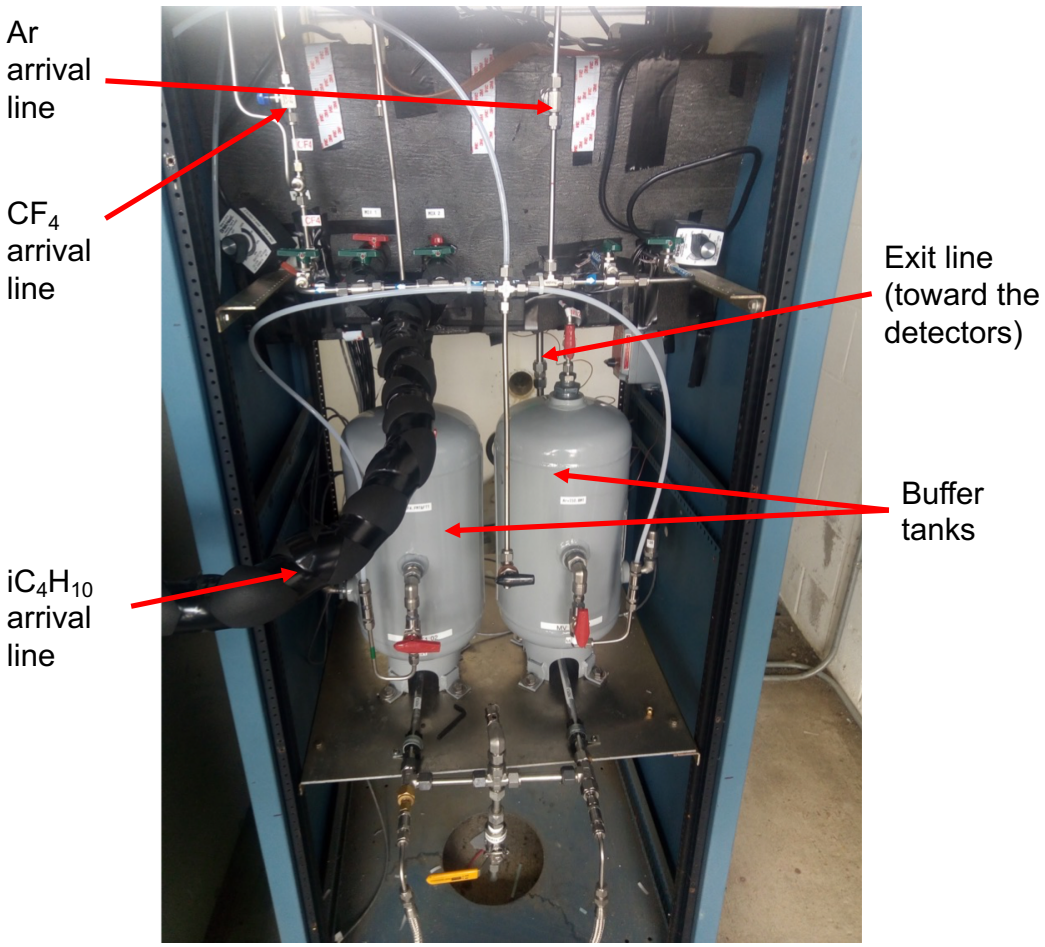

Figure 3.10: Photo of the gas mixing system. The two mixes are prepared in the buffer tanks at the center of the photo from argon, isobutane and tetrafluorocarbone bottles, the mixes are then sent into the hall to the detectors.

3.2.3 Software integration

In addition to the physical integration, the MVT and the FTT are integrated in the CLAS12 software system. This includes the CLAS12 interlock and remote control system (called slow controls). Monitoring is also done to continuously check the correct operation of the detector. Finally this includes data processing and in particular decoding and reconstruction.

Slow controls and interlocks

During data taking, access to the hall is not possible, remote control of the detectors is therefore essential. The majority of the sensors, valves and power supply channels are integrated in the slow control system. The slow control system is used by the shift staff or detector experts to turn on or off the Micromegas detectors. Interlocks are used to ensure the safety of the detector by raising an alarm and/or turning a system off if an incident occurs.

The overview of the MVT slow control system is shown on figure 3.11 (a similar tool is available for the FTT). The overview is designed to contain all the essential information about

the MVT, it also gives access to detailed windows for high voltages (HV), low voltages (LV), gas system and interlocks (see, for instance, figure 3.12).

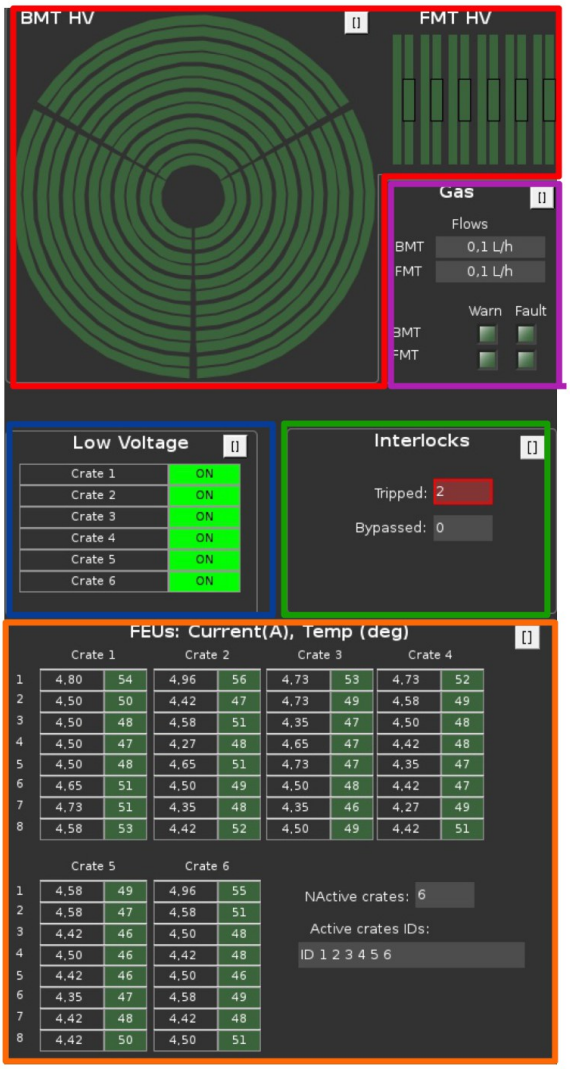

Figure 3.11: Overview of the MVT remote controls. The top region in red corresponds to the high voltages for the BMT and the FMT. The purple square is an overview of the gas system. The blue and orange regions correspond to the low voltage used to power the front-end units. The green square is an overview of the interlock status configured for the MVT.

The interlocks system is a set of rules related to measurements from MVT sensors. Interlocks are designed to make sure that the detector cannot be damaged by any incident or improper use of the detectors. Rules were added, removed or adjusted based on real incidents during the months of testing and during data taking. A view of the interlocks for the gas system and FEUs is shown on figure 3.13.

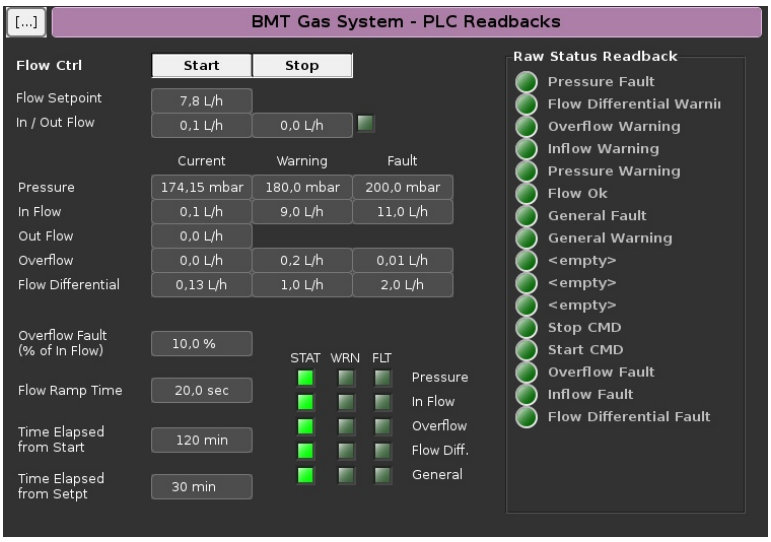

Figure 3.12: Detailed view of the MVT gas remote controls showing pressure and flow rates measurements and interlocks.

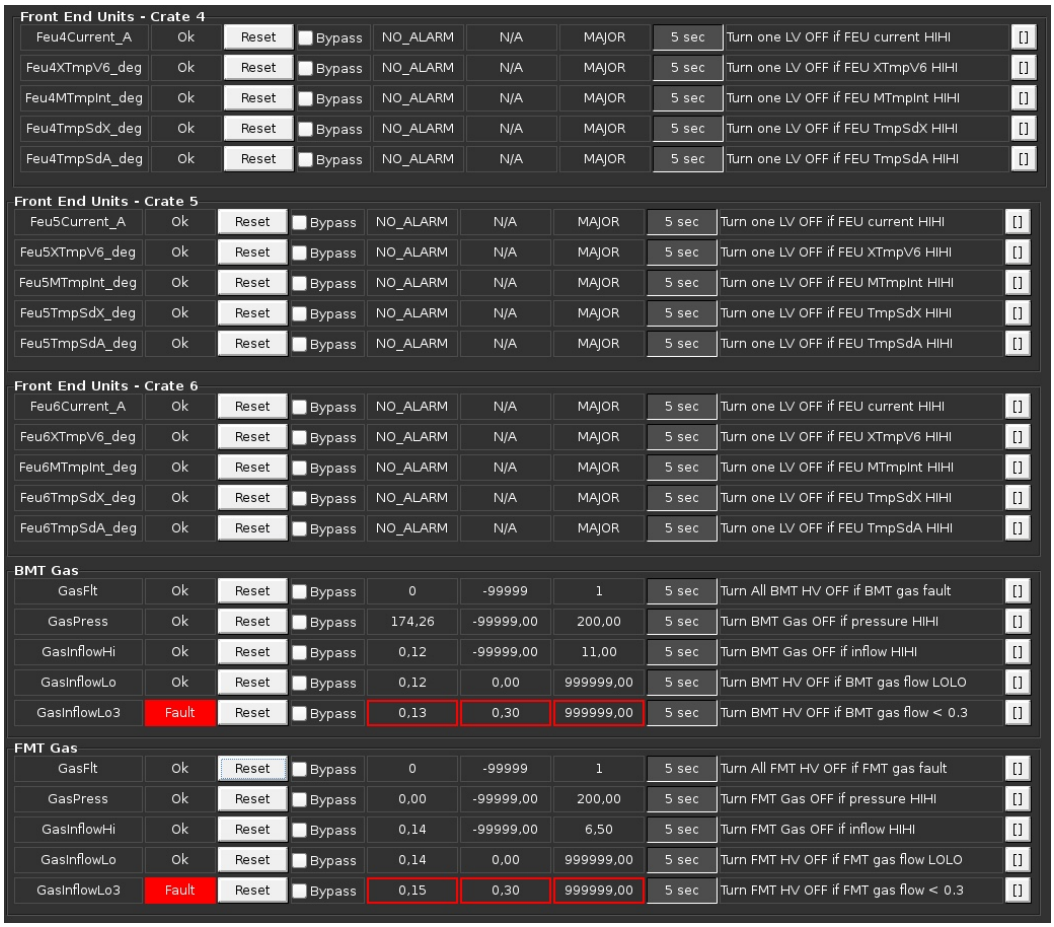

Figure 3.13: Detailed view of the MVT interlock controls. Each line corresponds to a specific rule. Most of the rules have alarms and warnings set before shutting the system down. Here two interlocks are triggered causing high voltages to be turned off because the gas flow is too low in the detectors.

Monitoring

In addition to slow controls, data collected by the MVT is also analyzed to ensure that the detectors are working properly. Using the CLAS12 software framework, monitoring tools have been developed to ensure the correct operation of the Micromegas detectors. One version, called shifter monitoring, is designed to be used by the shift staff during beam operation, while an expert version is used from time to time to display more information about an incident.

The shifter monitoring focuses on two kinds of histograms: hitmaps and time distribution histograms. Hitmaps show the accumulated number of hits per channel for each of the detectors, regularly refreshed (see figure 3.14). Noisy strips can therefore be easily identified, as well as electronic or cabling issue (groups of 64 or 512 channels exhibiting a different behavior), one can also spot gas circulation or gain issues.

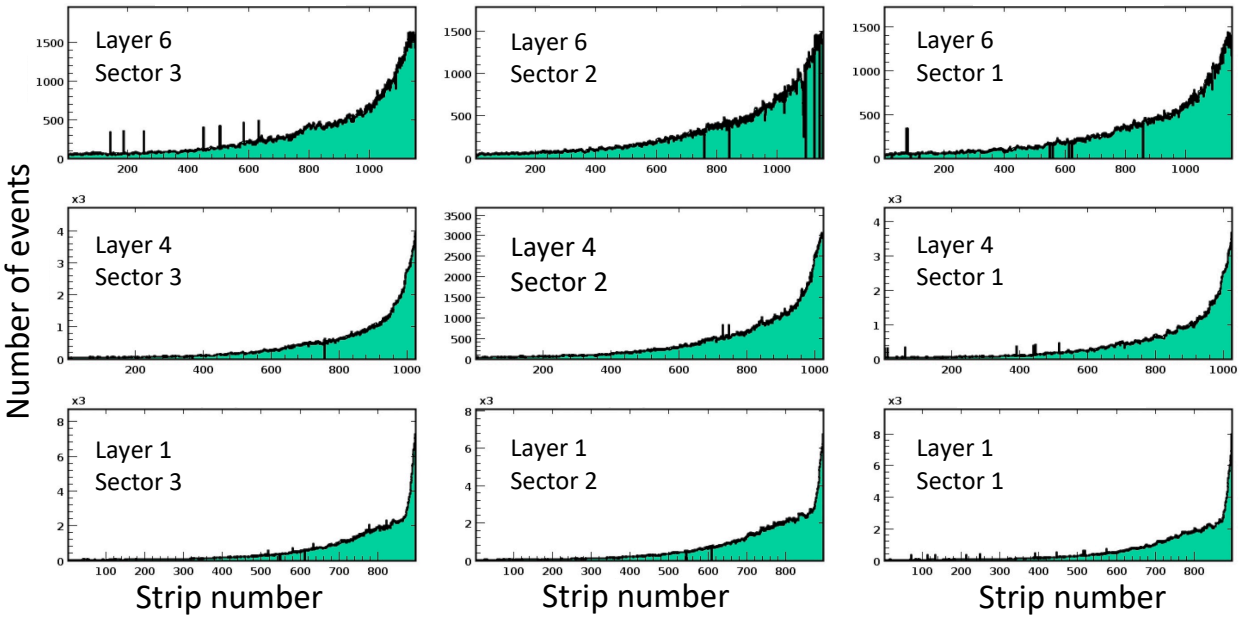

Figure 3.14: Hitmaps for the BMT C layers, from 10.6 GeV electron beam data (sectors in columns and layers in row). The shape is caused by the increasing flux of particles when the polar angle decreases. Noisy or dead channels are also visible.

The time distribution plot displays the time of the pulse within the acquisition window, defined by the maximum of the pulse (see figure 3.15). If the detector is properly parametrized, most of the pulses have their maximum around the middle of the time window visible over the background. This plot is used to synchronize the Micromegas electronics with the CLAS12 trigger system.

Unlike the shifter monitoring, composed of a very reduced sample of histograms, the expert monitoring contains all the plots that could be useful to identify incidents. Some examples of distributions from the expert monitoring are: average number of hits per event and per detector or channel, average maximum of the amplitude per strip, integral of the pulse, number of clusters

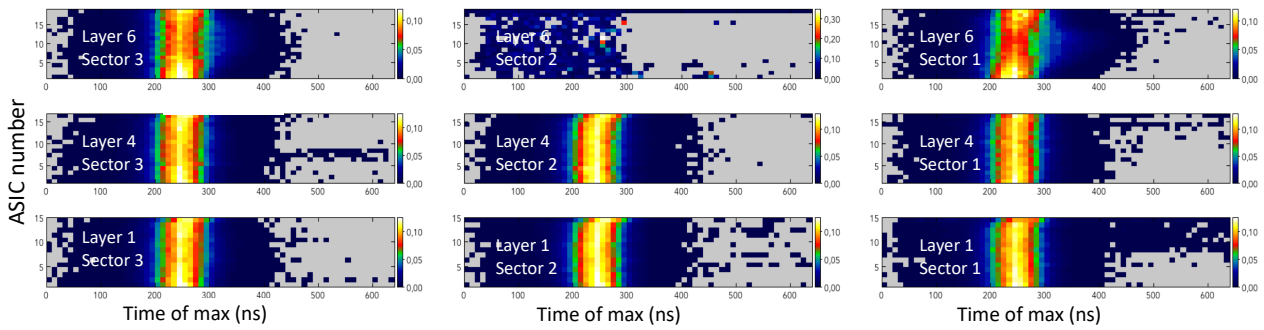

Figure 3.15: Distribution of the time of the maximum of the pulse within the acquisition window for all ASICs of the BMT C layers, from 10.6 GeV electron beam data. One can notice that the detector layer 6 sector 2 was not functioning properly when this data sample was taken.

(a cluster is a group of consecutive channels with hits), number of tracks, angles of the tracks with respect to the detector, etc. This tool was mainly used during the tests and commissioning.

Decoder

Micromegas detectors are used to reconstruct the trajectory of the particles passing through their active area. A first step, called the decoder, converts readout information into geometrical information: each electronic channel is associated with a given sector, layer and strip of a detector. The reconstruction then uses this decoded data, and performs tracking using the detector geometry.

During the assembly, cabling is carefully checked and recorded in the translation table, associating an electronic channel with a specific strip in the MVT, see figure 3.16 for an example of a translation table. The translation tables are kept in a database and used during the decoding process to extract geometrical information from data.

crate	slot	channel	sector	layer	component
69	24	1	1	1	896
69	24	2	1	1	895
69	24	3	1	1	894
69	24	4	1	1	893
69	24	5	1	1	892
69	24	6	1	1	891
69	24	7	1	1	890
69	24	8	1	1	889
69	24	9	1	1	888
69	24	10	1	1	887
69	24	11	1	1	886
69	24	12	1	1	885
69	24	13	1	1	884
69	24	14	1	1	883
69	24	15	1	1	882
69	24	16	1	1	881

Figure 3.16: Extract of the translation table for the BMT. The first three columns correspond to the readout (FEU, ASIC and channel number) and the last three columns correspond to the detector (sector, layer and strip number).

In addition to this data translation, the decoder is also used to reduce the size of events by reducing the information contained in an event. This is done by fitting the signals and storing only the results of the fit instead of the entire signal. A Micromegas signal, called a pulse, is composed of several samples, typically 5 to 16, with a 40 ns sampling time (see figure 3.17). For the Micromegas detectors, the decoder was written to compute and store the amplitude, the time of the maximum of the pulse and the integral of the pulse. A simple parabolic fit around the maximum sample is used to determine the time and amplitude of the pulse. To precisely extract the time of the maximum, a fine timestamp correction is also added. Because the clock frequency of the electronic chip is higher than the sampling frequency, precise clock information is stored when a trigger is received, to provide precise absolute time resolution for each signal.

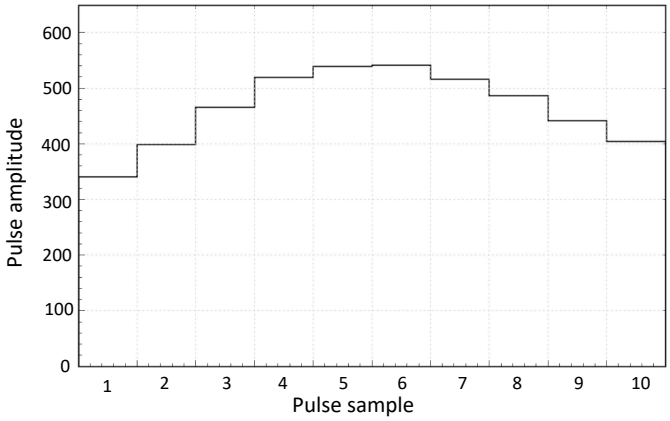

Figure 3.17: Example of a pulse with 10 samples recorded in the Micromegas detectors.

Once decoded, the events are reconstructed: the hits are gathered into clusters and the position of these clusters is used to determine the particle trajectory (see [71]). The reconstruction is not described in more details in this thesis since it was not part of the work done by the author.

3.3 Detector commissioning

3.3.1 Cosmic ray test bench

In order to calibrate detectors and test their performances, a cosmic test bench was designed and installed at CEA Saclay early in the project. The goal of this bench is to test each of the Micromegas detectors, to compute their 2D efficiency map using cosmic muons and to determine the best operating conditions of the detectors.

The cosmic test bench consists of a vertical stack of six detectors (see figure 3.18). Two scintillators are installed at the top and the bottom of the bench to provide the trigger. Four double-layer flat Micromegas (called multigens to distinguish them from the tested Micromegas detector) are used as trackers to provide the reference track of a cosmic ray. In the middle of the stack, empty trays receive the detectors which must be characterized.

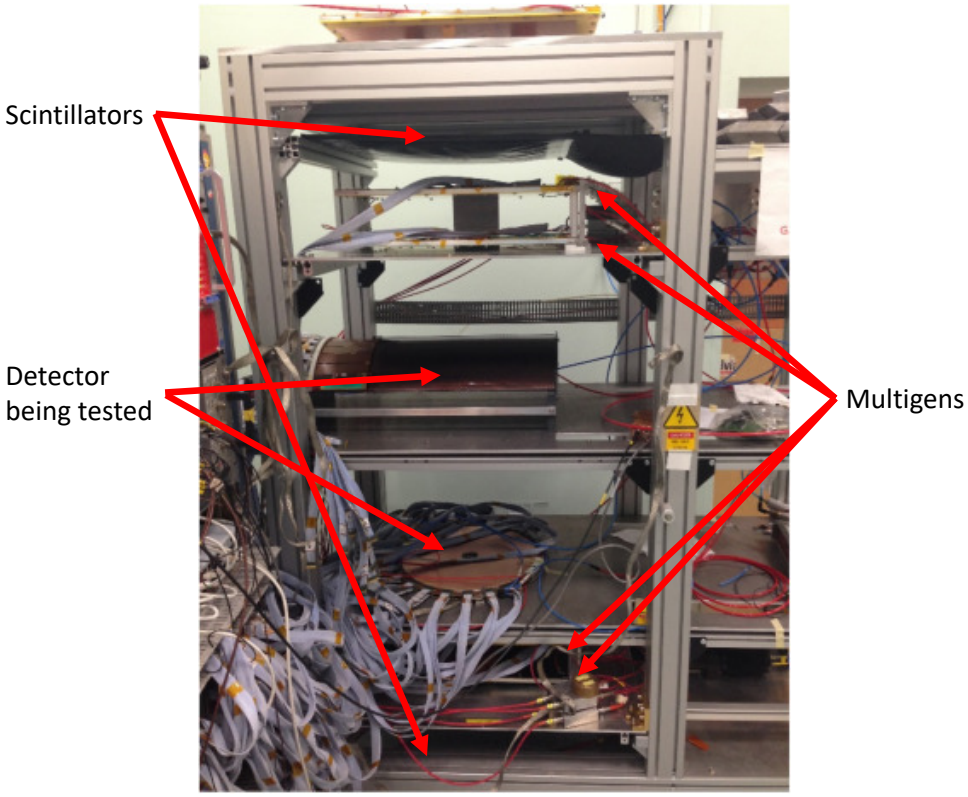

Figure 3.18: Picture of the cosmic ray bench used at CEA Saclay to test Micromegas detectors. Here a BMT tile and a FMT disk are being tested.

To use the cosmic bench, the first step is to work on the alignment of the four reference multigens. Among the four multigens, two are chosen as references. The other detectors are then aligned with respect to these reference multigens by finding rotations and translations of the remaining multigens to minimize their residuals with respect to the reference tracks provided by the two reference multigens. Once the multigens are aligned, the geometry of the detector being tested is implemented (flat geometry for the FMT and cylindrical geometry for the BMT). Once the geometry is implemented, the efficiency of the detector is obtained by comparing the intersection of the reference tracks provided by the multigens with the signal collected on the Micromegas tile or disk that is being tested. If the intersection of the track from the multigens with the Micromegas detector corresponds to a signal detected in the Micromegas, the particle is considered detected. The efficiency is therefore defined as the number of tracks going through the detector and that are associated with a hit, divided by the total number of tracks going through the detector:

$$\varepsilon = \frac{N_{tracks\ detected\ by\ the\ Micromegas}}{N_{tracks\ going\ though\ the\ Micromegas}} \tag{3.1}$$

All MVT and FTT detectors have been systematically characterized before shipment to Jefferson Lab. These tests included a study of the efficiency as a function of the amplification voltage, called the “efficiency plateau” (see figure 3.19) and a two-dimensional efficiency map (see figure 3.20 for an example). The efficiency map is used to check that the entire active area is

functioning while the efficiency plateau is used to determine the right operating point, being the minimal voltage with maximal efficiency, preventing any saturation of the readout (for instance about 500 V for the BMT tile shown in figure 3.19).

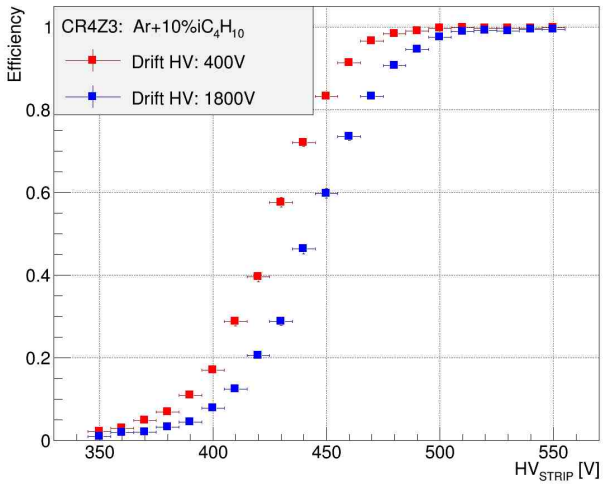

Figure 3.19: Efficiency as a function of the amplification high voltage at two drift voltages for a BMT tile, extracted from cosmic ray data. One can note that the onset of the plateau is shifted towards higher amplification voltage when the drift voltage increases (since the electron transparency depends on the ratio between the amplification voltage and drift voltage).

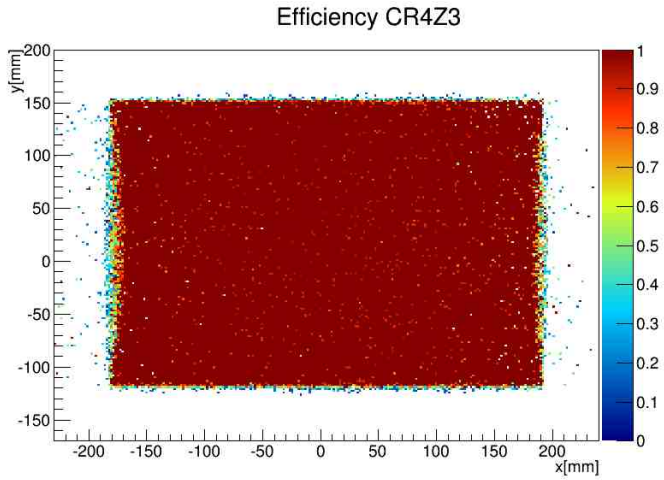

Figure 3.20: Efficiency map for a BMT tile, extracted from cosmic ray data.

3.3.2 Cosmic ray data taking with the central detector

Cosmic ray data taking with the SVT

Before beam data taking, the Micromegas detectors took several months of cosmic ray data with the SVT while being in the clean room. The trigger was provided by the SVT. This data

taking was mainly used to test the MVT. Cabling issues and faulty devices were identified and fixed. The electronics were tested and in particular noise studies were performed. Slow controls were implemented providing remote control and detector safety using interlocks. Detectors were tested, in particular high voltages were tuned and gas tests were made to adjust the flow rates. During this period, the tracking algorithm was being developed and was not good enough to perform advanced studies of detector performances, but some first tracks could be reconstructed (see figure 3.21).

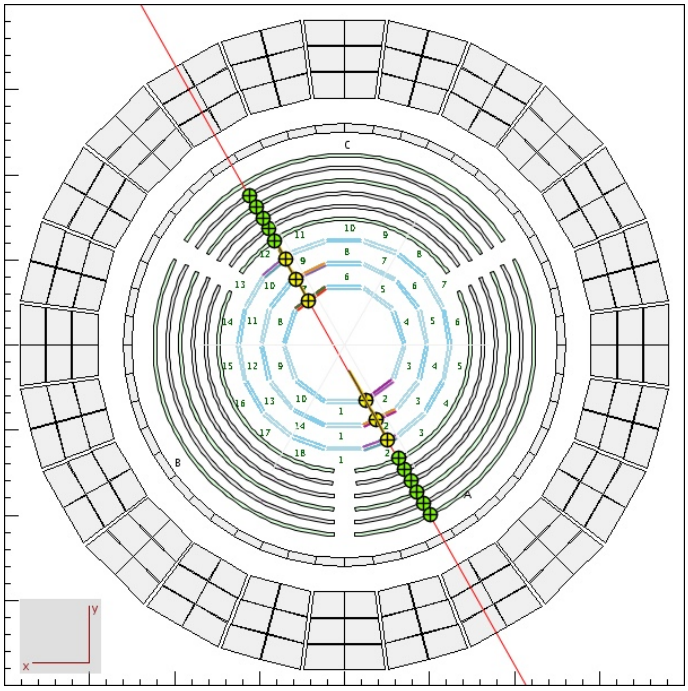

Figure 3.21: Example of a cosmic ray track reconstructed with the CVT. Yellow circles correspond to SVT hits, green circles correspond to BMT hits.

Cosmic ray data taking with the CTOF

Once the CVT was installed in the hall B, cosmic ray data was collected for alignment purposes. The trigger was provided by the CTOF, requiring diametrically opposed hits detected in coincidence. The distributions of events for two BMT layers are shown in figure 3.22, the peculiar distributions observed on the layer 2 are due to the convolution of the cosmic ray distribution with the acceptance of the trigger.

Cosmic ray data taking was also used to perform the alignment of the MVT. A straight-track reconstruction algorithm was developed and was used to align the detectors. The alignment procedure is not discussed here since it was not part of the work done for this thesis.

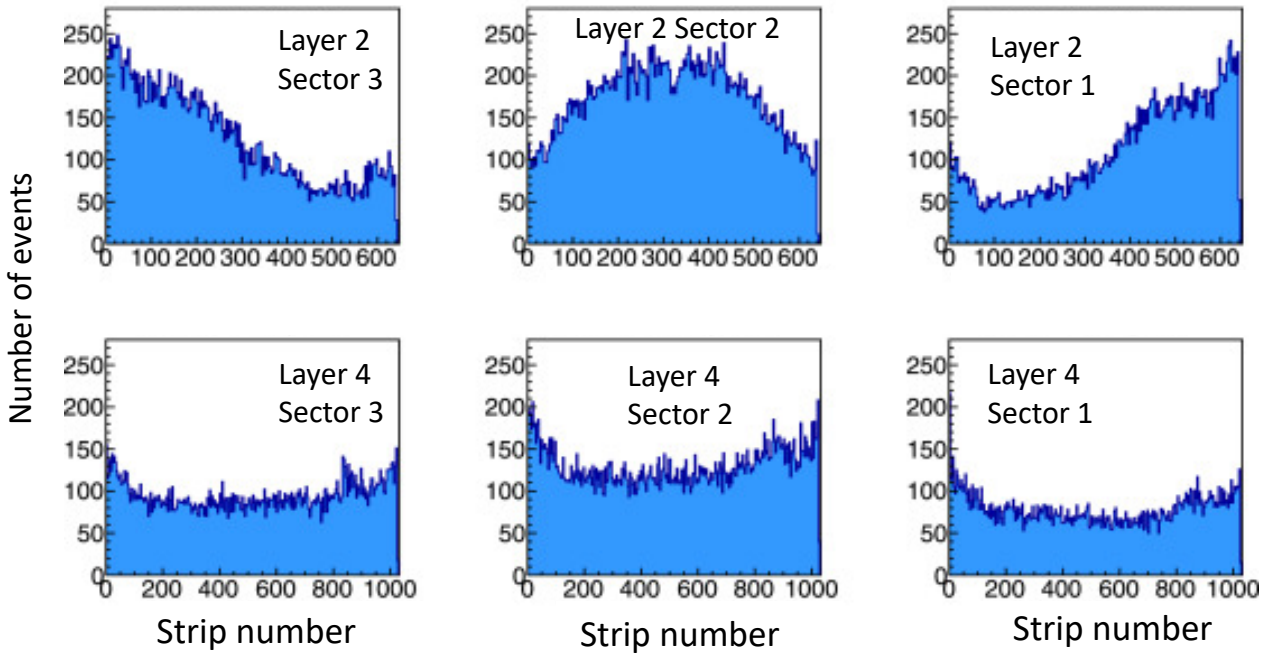

Figure 3.22: Hitmap histogram for cosmic ray data with CTOF used for the trigger for layer 2 (Z layer) and layer 4 (C layer) BMT tiles.

3.3.3 Beam data taking

The Micromegas detectors received their first electron beam at the beginning of 2018. Slow controls and monitoring tools were then used to understand and tune high voltages of the detectors with beam conditions.

Preparation of the electronics

The preparation of the electronics is done with two main steps:

- The first step, before receiving beam in the hall, is to take noise and pedestal run to check the level of noise in the detectors, configure zero suppression (described in section 3.1.6).
- If the level of noise detected by the electronics is sufficiently low, a synchronization of the detector with the trigger is performed, with low current beam conditions. Timing information, called the latency, is given to the FEUs so that the DREAM can fetch the pulse corresponding to a given trigger. The latency is modified and adjusted to match the trigger using time distributions from the monitoring software (figure 3.15). Once this is done, the reconstruction algorithm can be used and the first tracks can be seen in the detectors in coincidence with the SVT and the CTOF (see figure 3.23).

To reduce the amount of data collected from the Micromegas detectors, a method called sparse reading was developed (not part of the work done by the author). The sparse reading is

used to decrease the amount of data generated by the Micromegas detectors by recording, for each pulse, only half of the samples (one sample for every two is kept). The sparse reading was directly implemented in the Micromegas electronics and can be turned on and off at any time.

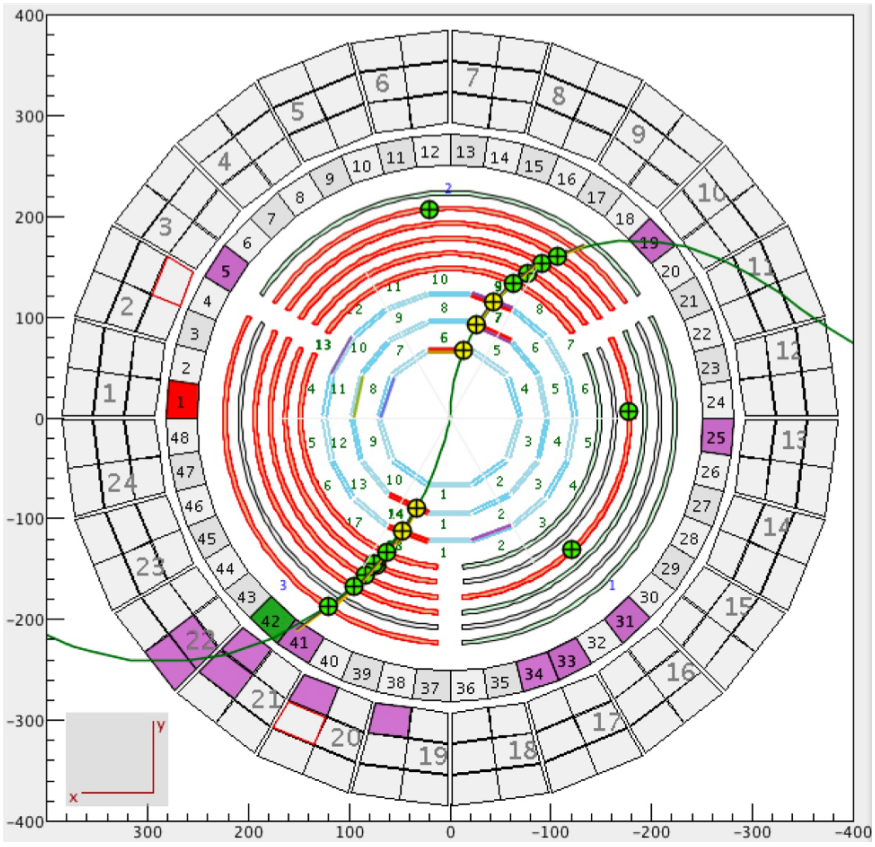

Figure 3.23: Example of tracks reconstructed in the central detector during beam data taking with the solenoid magnet turned on. Here two particles with the same charge are reconstructed.

High voltage tuning

A fine tuning of the high voltages is then performed. The results from the cosmic ray test bench (see section 3.3.1) provide an estimation of the optimal voltages, but, the conditions being different these values had to be refined to accomodate for the higher particle rate and the magnetic field. Ideally one wants to measure the efficiency as a function of the amplification voltage to find the "efficiency plateau", as explained in section 3.3.1. However, the reconstruction algorithm was not ready at this stage to compute the efficiency of the Micromegas detectors. Instead, the cluster multiplicity was used as an alternative observable expected to have a behavior similar to the efficiency (see figure 3.24). The cluster multiplicity is the number of clusters per event and per detector. The cluster multiplicity roughly corresponds to the number of charged particles that go through a Micromegas detector. Given the shape of the cluster multiplicity as a function of the amplification voltage, the nominal amplification voltage was set to 460 V for the FMT and 520 V for the BMT. At high amplification voltage, such as when the amplification voltage is

above 490 V (figure 3.24), the number of clusters increases suddenly. In this region, the amplification region becomes unstable, probably due to excessive amplification of noise fluctuations. Note that the number of hits cannot be used instead of the cluster multiplicity since the the number of hits depends on the amplification voltage.

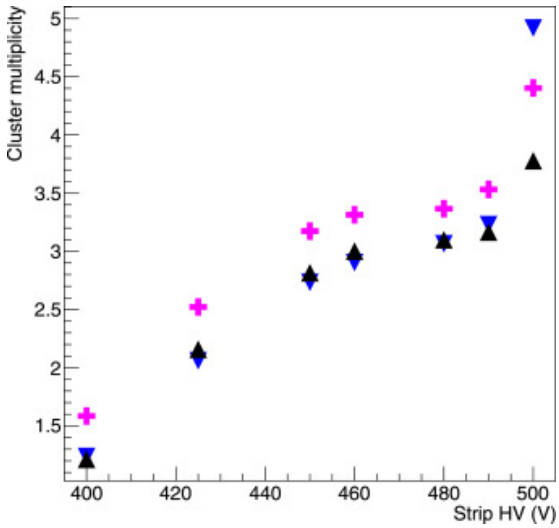

Figure 3.24: Cluster multiplicity as a function of the amplification voltage for three FMT disks. A "plateau" is visible between 460 V and 490 V.

Lorentz angle

The solenoid field affects the drift of the particles inside the Micromegas: instead of drifting orthogonally to the plane of the Micromegas, the charge carriers drift with an average angle, called Lorentz angle (see figure 3.25). This influences mostly BMT Z layers for which the signal collected may be shifted by a few strips. This effect has to be corrected, in order to avoid a systematic shift. Simulations were made to compute this shift, and an estimation was made by analyzing data. Note that the Lorentz angle depends on the drift voltage and high drift voltages are therefore used in the BMT to reduce this angle.

For a track, the angle α is defined as the angle of the incoming particle in the transverse plane (with respect to the beamline) as shown in figure 3.26. The distribution of the size of clusters as a function of this angle α is shown on figure 3.27, for tracks with negative charges. For negatively charged particles, when the angle α is equal to the Lorentz angle, all the charge carriers drift along the particle track, the cluster size is therefore minimal. An estimation of Lorentz angle from data can therefore be obtained from figure 3.27. This angle is then used to provide a Lorentz angle correction in the reconstruction algorithm. The variations of the solenoid magnetic field across the BMT being relatively small, the same value of Lorentz angle was used for all the strips and all the detectors. However, it may be possible to perform this study at different positions of the BMT detectors and compare these results with solenoid magnetic field maps to provide a more precise Lorentz angle value. The value calculated here was found to be in agreement with

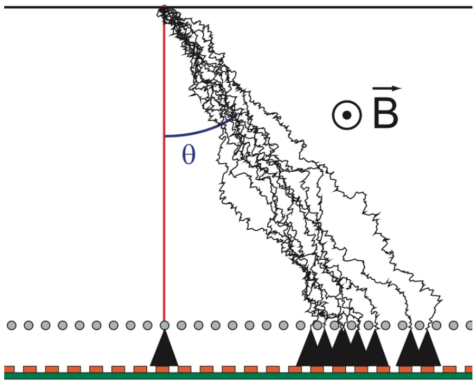

Figure 3.25: Schematic of a Micromegas detector illustrating the effect of the magnetic field on electrons formed at the top of the amplification gap. The Lorentz angle is noted θ.

the Lorentz angle calculated from simulations. To perform the reconstruction, a table is used to interpolation the correct Lorentz angle given the magnetic field and the drift electric field.

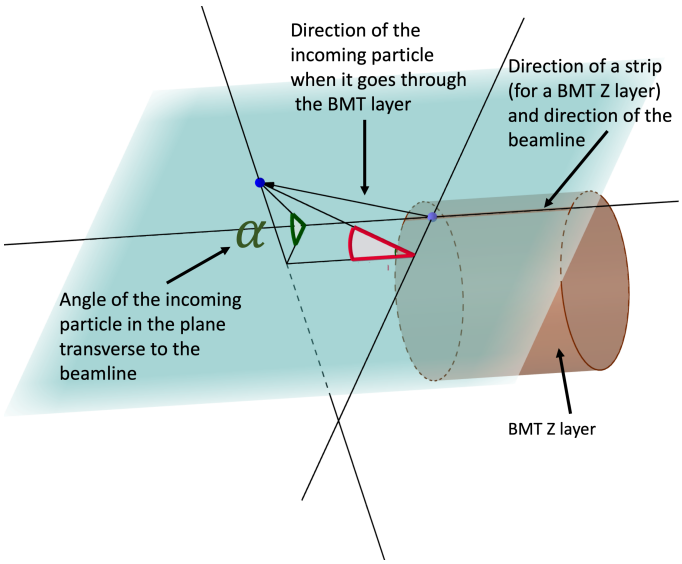

Figure 3.26: Definition of the α angle used to compute the Lorentz angle from data.

3.4 Conclusion

The assembly, commissioning and operation of the Micromegas detectors for the CLAS12 spectrometer have been explained. The main contributions from the author of this thesis are outlined in appendix A.4.

The Barrel Micromegas Tracker is the first curved Micromegas detector of this size. The performances of the Micromegas detectors have not yet been precisely determined but the first estimates give an efficiency of $\simeq 98\%$ and a resolution below 200 μm (see figure 3.28). The Micromegas technology will be used for tracking in future nuclear or high-energy physics experi-

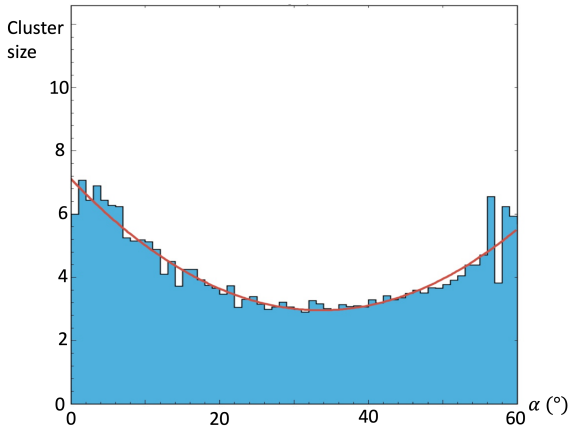

Figure 3.27: Cluster size as a function of the particle transverse angle α, for negatively-charged particles (BMT Z layer). The Lorentz angle corresponds to the angle for which the cluster size is minimal: here about 34°.

ments such as the ATLAS experiment at CERN which has decided to use resistive Micromegas detectors for the upgrade of its New Small Wheel [76].

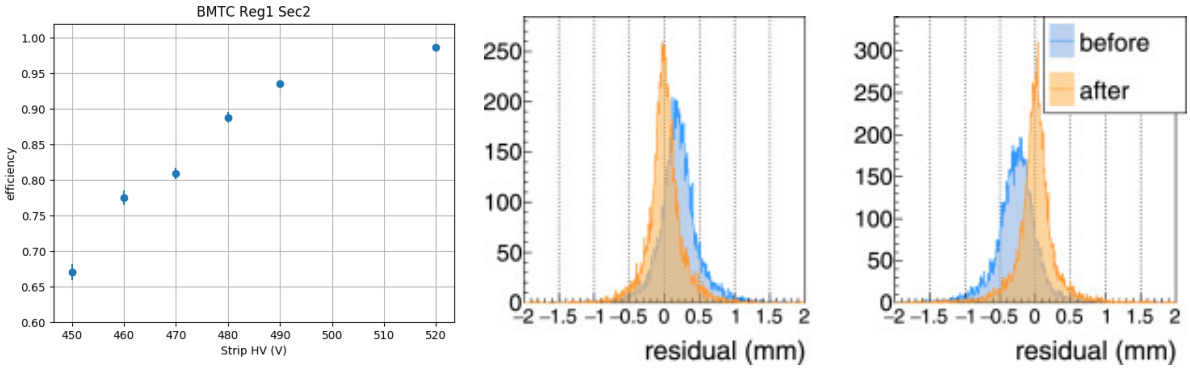

Figure 3.28: BMT performances [61]. Left: BMT efficiency in beam conditions. Right: BMT residuals for two tiles, before and after the alignment procedure.

Chapter 4

Photon electroproduction analysis

As described in chapter 1, GPDs can be accessed through the study of photon electroproduction beam-spin asymmetry (BSA). This chapter is dedicated to the extraction of photon electroproduction BSA off the proton at 10.6 GeV with the CLAS12 spectrometer.

In this chapter, the different steps of the photon electroproduction analysis are described. After an overview of the analysis, the first selection of events is characterized, followed by the definition of the binning, the exclusivity selection and the computation of the beam-spin asymmetries. Finally, corrections are applied and uncertainties are estimated. Unless specified otherwise, this whole chapter describes work done for this thesis by its author.

4.1 Overview of the analysis and definitions

In this chapter, the term "DVCS" refers to "photon electroproduction", even if it is not exact (see section 1.3.2). In addition, "π^0 events " will be used to refer to "π^0 electroproduction events". Moreover, the term "data" will be used to refer to data collected from the experiment with the CLAS12 spectrometer as opposed to "simulation" used to refer to data from simulation.

This thesis is based on the data collected during fall 2018, with a torus field configuration that bends electrons towards the beamline (called "electron inbending" data). Roughly 12% of the total data that will be collected by CLAS12 whith a 10.6 GeV electron beam and an unpolarized proton target is analysed here. Note that the data used for the analysis here is obtained from reconstruction and calibration procedures that are not fully refined and may be improved in the future.

4.1.1 How photon electroproduction events are detected with CLAS12

This analysis is based on the detection of exclusive DVCS events. This exclusivity criterion implies that all three particles of the final states are detected in the event.

While the electron is always detected in the FD (forward detector), the proton can be detected

either in the FD or the CD (central detector) and the photon can be detected either in the FD or the FT (forward tagger), the distributions are shown in table 4.1. A schematic of a typical DVCS event detected in CLAS12 is shown on figure 4.1.

Particles	Proton in CD	Proton in FD	Total
Photon in FD	36%	<0.3%	36%
Photon in FT	49%	15%	64%
Total	85%	15%	100%

Table 4.1: Distributions of DVCS events based on the detectors detecting the proton and the photon for the inbending magnetic field configuration.

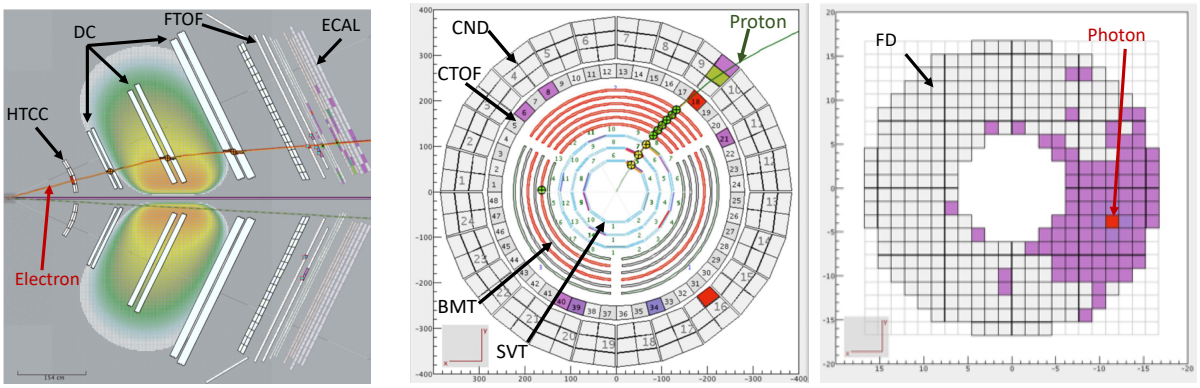

Figure 4.1: Schematic of a typical DVCS event, visualized using the CED tool (CLAS12 event display, see section 2.3.4). Lines (red squares for the FT) represent reconstructed particle tracks and colored shapes represent hits in the detector. The electron is reconstructed in the forward detector (left), the proton in the central detector (middle) and the photon in the forward tagger (right).

The CLAS12 software framework provides a set of rules for particle identification. In this analysis, these criteria are used for the identification of electrons, protons and photons (the development of the particle identification rules is not part of the work done for this thesis).

The following rules are used:

- electrons are identified from negatively charged tracks associated with an FTOF hit and the following ECAL and HTCC requirements (to separate electrons from other negatively charged particles and in particular π^-):
  - a hit in the HTCC with at least two photoelectrons
  - a hit in the PCAL with at least 60 MeV deposited
  - a sampling fraction (total energy deposition in the calorimeter divided by the momentum of the particle) within a five standard deviation from the expected value

- protons are identified from positively charged tracks (that are not already identified as positrons) associated with an FTOF hit (in the forward region) or CTOF hit (in the central region). A separation between protons, pions and kaons is done using the time-of-flight method (see appendix A.3.6).

- photons are identified from hits in the ECAL or FTCAL that are not associated with charged tracks. In the ECAL, photons and neutrons are separated with the time-of-flight method: a cut on $\beta = v/c$ (with v the velocity of the particle estimated with the time-of-flight method and c the speed of light) is applied at 0.9.

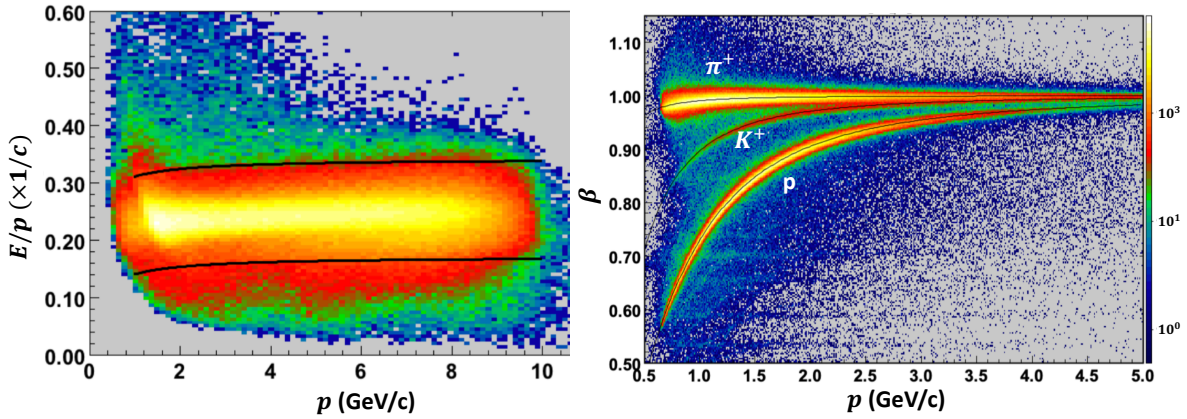

Figure 4.2: Plots illustrating identification of electrons and protons. Left: sampling fraction (total energy deposited in the calorimeter divided by momentum) as a function of momentum, the black lines represent the cuts applied for electron identification. Right: $\beta = v/c$ (with v the velocity of the particle and c the speed of light) as a function of momentum for positive charges in the forward detector.

This selection, with relatively loose cuts, provides a large number of candidates. The remaining background is cleared by the exclusivity cuts (see section 4.4).

4.1.2 Overview of the analysis steps

Pre-selection of events

This analysis starts with the pre-selection (section 4.2): reconstructed data files are skimmed to create small files containing only the information needed for this analysis. A first selection is done to select events with exactly one reconstructed electron. Cuts on Q^2 and W are applied to keep only the kinematic regions of interest from a phenomenological point of view. Events that do not contain at least a proton and a photon are also removed, to be able to perform a fully exclusive analysis. Finally, for each remaining event, the best DVCS candidate is formed among the protons and photons that are reconstructed. π^0 electroproduction events are also selected from events with at least two photons and are used at later stages (section 4.6).

Binning

In this analysis, the phase-space is binned with respect to the variables Q^2, x_B, t and ϕ. This binning, defined in section 4.3, is the result of a consideration of the DVCS yields and the dependencies of the BSA.

Exclusivity selection

To identify DVCS events from the DVCS candidates, a set of exclusivity cuts are applied (section 4.4). Exclusivity variables and exclusivity cuts are based on the four-momentum conservation for the $ep \to ep\gamma$ process:

$$l + p = l' + p' + q' \tag{4.1}$$

where l, p, l', p' and q' are the beam electron, target proton, scattered electron, recoil proton and final photon four-momentum. The initial four-momentum l and p are known: the electron beam received is precisely characterized by the accelerator and the target proton is assumed at rest. All the final four-momenta l', p' and q' are reconstructed with the CLAS12 spectrometer.

π^0 background subtraction

The main challenge with photon electroproduction extraction is the estimation of the dominant source of background: π^0 electroproduction $ep \to ep\pi^0$ (other sources of background are either removed by exclusivity cuts or neglected in this analysis). In this process, the π^0 decays electromagnetically into two photons $ep \to ep\pi^0 \to ep\gamma\gamma$ within 10^{-16} s (with a branching ratio close to 99%, other π^0 decay modes will be neglected in this analysis). In this analysis, the π^0 decay is considered instantaneous and only the resulting photons can be detected.

While the decay is symmetric in the pion center of mass frame by four-momentum conservation, the pion is not at rest in the laboratory frame and the decay generally becomes asymmetric. To understand the process in the laboratory frame, each photon has to be boosted in the direction of the pion. Depending on the angle of the decay with respect to the boost direction, the photons are seen with potentially very different momenta in the laboratory frame. In case of very asymmetric decays in the laboratory frame, one photon can get almost all of the π^0 energy, and the other photon only a very small amount of the energy (see figure 4.3). If only the high-energy photon is detected, the event mimics a DVCS event.

In practice, since the resolution of the detectors is not perfect, it is not always possible to distinguish π^0 from DVCS events. The probability that a π^0 event is analysed as a DVCS event depends on the π^0 direction/energy and on the DVCS selection criteria. The π^0 events that pass the DVCS selection are called contamination. This contamination is generally not negligible in most regions of the phase-space and has to be estimated and corrected for. In this analysis, an estimated π^0 contamination is computed based on a simulation and on the π^0 events selected in data (section 4.6).

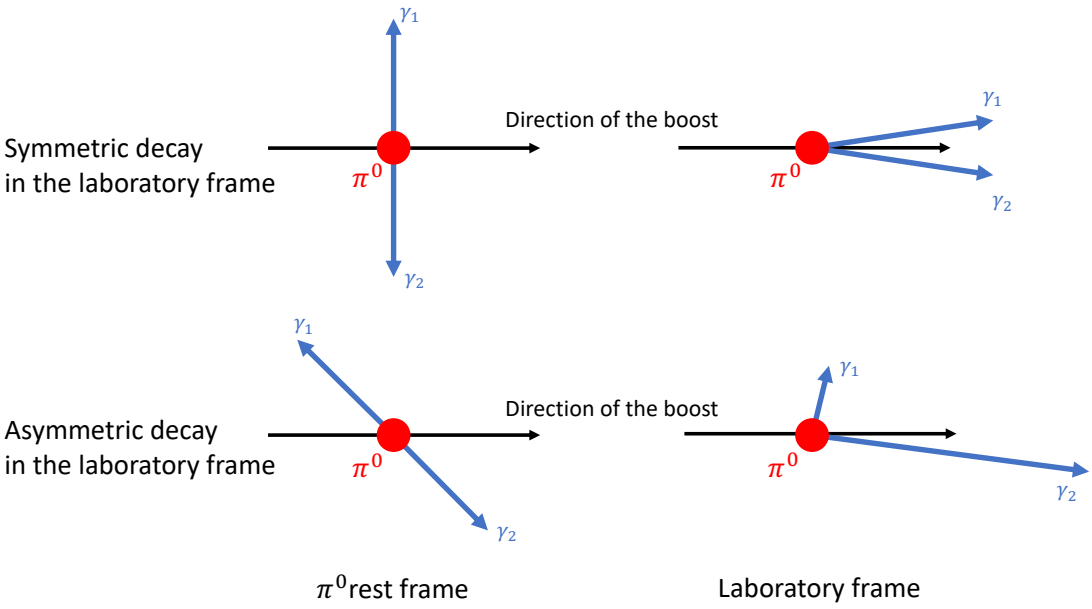

Figure 4.3: Schematic of the decay of a π^0 into two photons. The energy of the π^0 is shared between the two photons depending on the angle of the decay with respect to the direction of the boost i.e. the direction of the π^0 in the laboratory frame.

In this analysis, the π^0 background is taken into account in two steps. In the first step, a selection of π^0 events is performed, to remove from the DVCS analysis all the events that are clearly identified as π^0 events. These π^0 events are reconstructed exclusively from $ep \rightarrow ep\gamma\gamma$ events with exclusivity cuts to identify them, in a similar way to DVCS. In the second step, the remaining contamination is estimated. To estimate this contamination, exclusive π^0 electroproduction is simulated, scaled by the number of exclusive π^0 identified with two photons reconstructed in the data and passed through the same analysis as data. The fraction of events that pass the DVCS and π^0 selection cuts in the simulation are used to estimate the contamination in data.

Bin migration correction

As mentioned above, the results of this analysis are binned with respect to the kinematic variables. It is therefore possible, since the resolution of the detectors is not perfect or because of energy losses for the particles, that some events from a given bin are reconstructed in another bin (phenomenon called "migration"). Its impact on the BSA and the correction needed are estimated in section 4.7.

Estimation of the uncertainties

Finally, statistical and systematic uncertainties are estimated in section 4.8. The statistical uncertainty takes into account both the statistical uncertainty associated with the DVCS events and

the statistical uncertainty associated with the π^0 events. Systematic uncertainties are associated with the beam polarization, the contamination subtraction and the bin migration.

4.1.3 Simulation

Overview of the simulation process

In order to perform this analysis, simulations of the detection and reconstruction of DVCS and π^0 in the CLAS12 spectrometer are needed. The GEMC software, briefly described in section 2.3.4, is used for the simulation. The simulation can be decomposed in three main steps:

1. a Monte-Carlo generator is used to generate a set of DVCS and π^0 events. Each event contains particles and their four-momenta: an electron, a proton and a photon for a DVCS event and an electron, a proton and two photons for a π^0 event.

2. the propagation of these particles from the target and through the detector is simulated in GEMC, for each event. GEMC is the CLAS12 simulation software, briefly described in section 2.3.4, it contains a description of all the detectors from the CLAS12 spectrometer. The interaction of the particles with matter and the signals induced in the detectors are simulated in GEMC. Simulated events are obtained, containing detector hits, with the same structure as experimental data events.

3. the simulated event is finally decoded and reconstructed by the CLAS12 reconstruction software, as if it was an event from data. The reconstructed event is then ready to be used in this analysis.

The second and third step, described above, are based on common CLAS12 software (GEMC and the reconstruction software), which are not part of the work done in this thesis. The event generator, however, is specific to this analysis and was developped by the author.

Monte-Carlo event generator

DVCS and π^0 event generators had already been conceived in the past, however they are usually only able to generate either DVCS or π^0 events but not both DVCS and π^0 events. A Monte-Carlo event generator, capable of generating DVCS, π^0 or both has therefore been developped. The challenge is to generate a number of DVCS and π^0 events that follows the cross-section models used in the generator.

The event generator is separated into two steps:

1. a set of kinematic variables (Q^2, x_B, t, ϕ) is generated and the choice of generating a DVCS or a π^0 event is made.

2. the four-momenta of all particles are computed based on the kinematic variables (Q^2, x_B, t, ϕ) generated in the first step.

Each of these two steps are detailed below.

To perform this first step, because of the very large dependencies of the photon electroproduction cross-section on the kinematic variables, the simple "accept or reject" algorithm is not efficient to sample the cross-section. An implementation of the Metropolis-Hastings algorithm [77] [78] was therefore performed. First, the limits of the phase-space are computed based on the experimental constraints (beam energy, angular acceptance of the detector). Note that since the range in t is different between the photon and the π^0 electroproduction process, t is generated between 0 and 1 and then scaled between the extreme accessible values t_{min} and t_{max}. A starting point $x_0 = (Q^2, x_B, t, \phi)$ is generated randomly inside the accessible phase-space. A new point $x_{i+1,\,proposed}$ is generated from the point x_i by picking from a Gaussian probability density centered around x_i and of resolution σ (the choice of σ will be discussed below):

$$x_{i+1,\,proposed} = x_i + \mathcal{G}aus(x_i, \sigma) \tag{4.2}$$

The "acceptance ratio" α of the point $x_{1,\,proposed}$ is calculated as follows:

$$\alpha = \frac{f(x_{i+1,\,proposed})}{f(x_i)} \tag{4.3}$$

with f the function that is being sampled (the choice of the function f for the generation of DVCS or π^0 will be discussed below). A random number A is then uniformly generated between 0 and 1.

$$A = \mathcal{U}niform(0,1) \tag{4.4}$$

If $A < \alpha$ the point $x_{i+1,\,proposed}$ is accepted as the next point $x_{i+1} = x_{i+1,\,proposed}$, otherwise the point is rejected and the point x_i is used as the next point $x_{i+1} = x_i$. Note that the point x_{i+1} is always accepted if $\alpha \geq 1$.

$$\begin{cases} \text{if } A < \alpha,\ x_{i+1} = x_{i+1,\,proposed} \\ \text{if } A > \alpha,\ x_{i+1} = x_i \end{cases} \tag{4.5}$$

This is repeated for each iteration. Here f is either an estimation of the DVCS cross-section from a DVCS model $f = f_{DVCS}$ or an estimation of the π^0 cross-section from a π^0 model $f = f_{\pi^0}$ or the sum of the two $f = f_{DVCS} + f_{\pi^0}$, depending on whether the generator is used to generate only DVCS events, only π^0 events or both DVCS and π^0 events. When the generator is used to generated both DVCS and π^0 events, for each step, once the point x_{i+1} has been determined, the selection of the process is made randomly based on the ratio of cross-sections. Another number

B, randomly generated from a uniform distribution between 0 and $f(x_{i+1})$, is used.

$$B = \mathcal{U}niform(0, f(x_{i+1})) \tag{4.6}$$

The process is then chosen as follows:

$$\begin{cases} \text{if } B < f_{DVCS}\text{, generate a DVCS event} \\ \text{if } B > f_{DVCS}\text{, generate a } \pi^0 \text{ event} \end{cases} \tag{4.7}$$

The choice of $\sigma = (\sigma_{Q^2}, \sigma_{x_B}, \sigma_t, \sigma_\phi)$ and the number of iterations are important. Indeed if σ is taken as very small compared to the size of the phase-space, a very large number of iterations will be needed to cover the entire phase-space. And if σ is taken too large, the "acceptance ratio" can become extremely small and the algorithm could remain stuck on a few points (in particular for the photon electroproduction, which has a cross-section that varies steeply with the kinematic variables). To perform this analysis, several millions of DVCS and π^0 events have been generated and the following values were used:

$$\begin{aligned} \sigma_{Q^2} &= 0.15\ GeV^2/c^4 \\ \sigma_{x_B} &= 0.015 \\ \sigma_t &= 0.15\ GeV^2/c^4 \\ \sigma_\phi &= 0.3\ ^\circ \end{aligned} \tag{4.8}$$

The model used to estimated the DVCS cross-section is from a private communication with Pierre Guichon and the model used for the π^0 cross-sections is based on a parametrisation of CLAS results from Valery Kubarovsky.

The second step of the event generation can be performed by analytical calculations. The four-momentum of the scattered electron is entirely constrained (up to a global rotation around the beam axis) by the beam energy, Q^2 and x_B. The proton and the photon (for DVCS) or the proton and the π^0 (for π^0 electroproduction) are then entirely constrained by t, ϕ and the necessity to follow the four-momentum conservation. For the case of π^0 events, the decay of the π^0 is simulated. A random direction is selected along which the two photons from the decay are emitted, back-to-back, in the π^0 center-of-mass frame. The two photons are then boosted back to the laboratory frame. A file is created, containing all the four-momenta generated. This file is used as an input file by GEMC, to simulate the propagation, through the CLAS12 detectors, of the particles generated by the event generator.

4.2 Pre-selection of events

The goal of the pre-selection is to filter events and to form either exclusive DVCS or exclusive π^0 candidates. Events are first selected based on their topology: their number of electrons, protons and photons. Kinematic cuts are then applied to ensure that the study is done in a kinematic regime appropriate for phenomenological analysis. To take into account events with multiple protons and photons without increasing the combinatorics, a selection of best proton and photons is then performed to reduce the number of candidates in the following analysis. Finally, among the remaining photons, the best candidates for a potential DVCS or π^0 event are identified.

Note that, as explained in section 4.1.2, π^0 events selected from data are used to reduce and estimate the π^0 contamination. This pre-selection is used to prepare for the selection of both DVCS and π^0 events and therefore treats the two processes in a similar way.

4.2.1 Event topology selection

As mentioned in section 4.1.1, events are only used if they contain at least one identified electron, at least one identified proton and at least one identified photon. The identification of the particles is done following the criteria defined in section 4.1.1.

In addition, this study makes use of the electron trigger (see section 2.3.4), which is designed to select inclusive electron scattering events. To avoid any potential issue, events that have more than one electron are rejected.

Table 4.2 summarizes the number of particles required in each event in application of the event topology criteria.

Particles	Number
Electron	1
Proton	≥ 1
Photon	≥ 1

Table 4.2: Event topology criteria

4.2.2 Kinematic cuts

To ensure that this study is done in the Bjorken regime, in which theoretical interpretations of the results can be considered (see section 1.3.1), cuts are applied to the kinematic variables Q^2 and W^2, to be in the region where the factorization can be applied and above the main resonance region. Since these variables only depend on the reconstructed electron, they can be computed for each event, without ambiguity, after applying the event topology selection. Kinematic cuts

used in this analysis are:

$$\begin{aligned} Q^2 &> 1\ GeV^2/c^4 \\ W^2 &> 4\ GeV^2/c^4 \end{aligned} \tag{4.9}$$

It was decided, however, not to apply a cut on $|t|/Q^2$ to leave more flexibility in the analysis a posteriori. It is still possible to select only some of the bins Q^2 and t bins afterwards.

4.2.3 Selection of best particles

After applying the event topology criteria, each event kept has only one electron but can have several protons and several photons. To reduce the potential combinatorics, a selection of the best proton is performed, followed by a selection of three best photons.

This selection is done using the missing masses in $ep \to epX$ and in $ep \to ep\gamma X$, noted as $MM_{ep\to epX}$ and $MM_{ep\to ep\gamma X}$, and defined as:

$$MM_{ep\to epX} = \sqrt{(l+p-l'-p')^2} \tag{4.10}$$

$$MM_{ep\to ep\gamma X} = \sqrt{(l+p-l'-p'-q')^2} \tag{4.11}$$

with the notations used in section 4.1.2.

Selection of the best proton

By momentum conservation (see equation 4.1), in the case of an ideal DVCS event, the missing mass is null:

$$MM_{ep\to epX} = \sqrt{(q')^2} = 0\ \mathrm{GeV/c^2} \tag{4.12}$$

since it is the mass of the final photon, and in the case of an ideal π^0 event:

$$MM_{ep\to epX} = m_{\pi^0} \approx 0.135\ \mathrm{GeV/c^2} \tag{4.13}$$

In order to select the best proton, the missing mass squared $MM^2_{ep\to epX}$ is computed for each of the protons and only the proton that has the closest value to 0 is kept. Since the mass of the π^0 is very small, this selects both DVCS and π^0 events over the remaining background.

Selection of the best photons

The number of photons is then reduced to a maximum of three, based on the missing mass squared $MM^2_{ep\to ep\gamma X}$. The three photons that have the closest value to 0 are kept. This selects

both photon and π^0 electroproduction since in both cases, an ideal event has a missing mass:

$$MM^2_{ep\to ep\gamma X} = 0\,\mathrm{GeV}^2/\mathrm{c}^4 \tag{4.14}$$

4.2.4 Selection of best photon and π^0 electroproduction candidates

Finally, among the three photons, one is selected as the best DVCS candidate and two (not necessarily different from the first one) as the best π^0 candidates. If the event contains only one photon, it is automatically assigned as a DVCS candidate. Otherwise, this selection is based on the value of the exclusivity variables. For each exclusivity variable i we define a distance d^i:

$$d^i = \frac{(x^i - x^i_{expected})^2}{(\eta^i)^2} \tag{4.15}$$

where x^i is the value of the variable i calculated from data, $x^i_{expected}$ is the expected value for an ideal event and η^i is the estimated resolution of the variable i. The total distance d is defined as the sum of the distances for all the exclusivity variables:

$$d = \sum_{i=variables} d^i \tag{4.16}$$

For each event with at least two photons, the total distance d_{DVCS} is calculated using DVCS exclusivity variables for each photon. And for each event with three photons, the total distance d_{π^0} is calculated using π^0 exclusivity variables for each couple of photons. The variables used for DVCS are defined as follows:

- the missing mass $MM_{ep\to epX}$, defined in equation 4.10
- the missing mass $MM_{ep\to ep\gamma X}$, defined in equation 4.11
- the missing energy $ME_{ep\to ep\gamma X}$, defined as

$$ME_{ep\to ep\gamma X} = E + E_p - E' - E_{p'} - E_{q'} \tag{4.17}$$

  where E, E_p, E', $E_{p'}$ and $E_{q'}$ are the beam electron,target proton, scattered electron, recoil proton and final photon energies.

- the photon cone angle $\theta_{\gamma\,cone}$, defined as the angle between the measured photon $\vec{q'}$ and the expected exclusive photon calculated using the other particles $\vec{q'}_{exclusive} = \vec{l} + \vec{p} - \vec{l'} - \vec{p'}$
- the missing transverse momentum $M_{p_\perp}$, defined as

$$M_{p_\perp\, ep\to ep\gamma X} = (l + p - l' - p' - q')_\perp = \sqrt{(l_x + p_x - l'_x - p'_x - q'_x)^2 + (l_y + p_y - l'_y - p'_y - q'_y)^2} \tag{4.18}$$

The variables used for π^0 candidates are defined as follows:

- the missing mass $MM_{ep\to ep\gamma\gamma X}$, defined as

$$MM_{ep\to ep\gamma\gamma X} = \sqrt{l + p - l' - p' - q'_1 - q'_2} \tag{4.19}$$

  where q'_1 and q'_2 are the four-momenta of the two photons associated with the π^0 event.

- the π^0 invariant mass $M_{\gamma\gamma}$, defined as

$$M_{\gamma\gamma} = \sqrt{q'_1 + q'_2} \tag{4.20}$$

- the missing energy $ME_{ep\to ep\gamma\gamma X}$, defined as

$$ME_{ep\to ep\gamma\gamma X} = E + E_p - E' - E_{p'} - E_{q'_1} - E_{q'_2} \tag{4.21}$$

  where $E_{q'_1}$ and $E_{q'_2}$ are the energies of the two final photons.

- the π^0 cone angle $\theta_{\pi^0\ cone}$, defined as the angle between the π^0 momentum, reconstructed from the two photons $\vec{q'_1} + \vec{q'_2}$ and the exclusive π^0 calculated using the other particles $\vec{q}_{\pi^0\ exclusive} = \vec{l} + \vec{p} - \vec{l'} - \vec{p'}$

- the missing transverse momentum $M_{p_\perp\ ep\to ep\gamma\gamma X}$, defined as

$$M_{p_\perp\ ep\to ep\gamma\gamma X} = (l + p - l' - p' - q'_1 - q'_2)_\perp \tag{4.22}$$

Table 4.3 shows the variables, estimated resolutions and expected values that are used in equation 4.16 for photon or π^0 electroproduction. Note that in this table, resolutions are only roughly estimated since they are only used to identify the best candidates among the background, not to select final DVCS or π^0 events. A much deeper study of the exclusivity variables is presented in section 4.4.

Since the total distances d_{DVCS} and d_{π^0} are expected to be null for ideal DVCS or π^0 events, for each event, the photon that minimizes d_{DVCS} and the couple of photons that minimize d_{π^0} are tagged as the best DVCS and best π^0 candidates respectively. Because the number of photons kept after the first selection can vary between 1 and 3, each event has one photon tagged as the best DVCS candidate and, if the event has at least two photons, a couple of them tagged as the best π^0 candidate.

Note that, even after this pre-selection, most of the events are not DVCS or π^0 events, so most of the particles tagged as best DVCS and π^0 events are background and will be removed at later stages of the analysis.

Photon electroproduction			π^0 electroproduction		
Variable i	$x^i_{expected}$	η^i	Variable i	$x^i_{expected}$	η^i
$MM^2_{ep\to ep\gamma X}$ (GeV^2/c^4)	0	0.01	$MM^2_{ep\to ep\gamma\gamma X}$ (GeV^2/c^4)	0	0.01
$MM_{ep\to e\gamma X}$ (GeV/c^2)	0.938	0.5	$M_{\gamma\gamma}$ (GeV/c^2)	0.135	0.015
$ME_{ep\to ep\gamma X}$ (GeV)	0	1	$ME_{ep\to ep\gamma\gamma X}$ (GeV)	0	1
$\theta_{\gamma\ cone}$ $(^\circ)$	0	1	$\theta_{\pi^0\ cone}$ $(^\circ)$	0	1
$M_{p_\perp\ ep\to ep\gamma X}$ (GeV/c)	0	0.2	$M_{p_\perp\ ep\to ep\gamma\gamma X}$ (GeV/c)	0	0.2

Table 4.3: Variables, expected values and estimated resolutions used for the selection of the best DVCS and π^0 candidates. Exclusivity variables are defined is section 4.4

4.3 Binning of the kinematic domain

Ideally we would like to extract a result for each possible value of our kinematic variables (Q^2, x_B, t, ϕ) inside the accessible kinematic domain. In practice, the accessible kinematic domain has been split, to create kinematic bins. The analysis is performed separately on each of these bins in order to extract a result for each bin if possible. Below is the description of the 24 bins used for the kinematic variables Q^2, x_B and t:

- three bins in x_B
- each x_B bin has four t bins
- each of the t-x_B bins has two Q^2 bins

The binning is adapted to follow the distribution of events as shown in figure 4.4. A precise description of the binning is given in table 4.4.

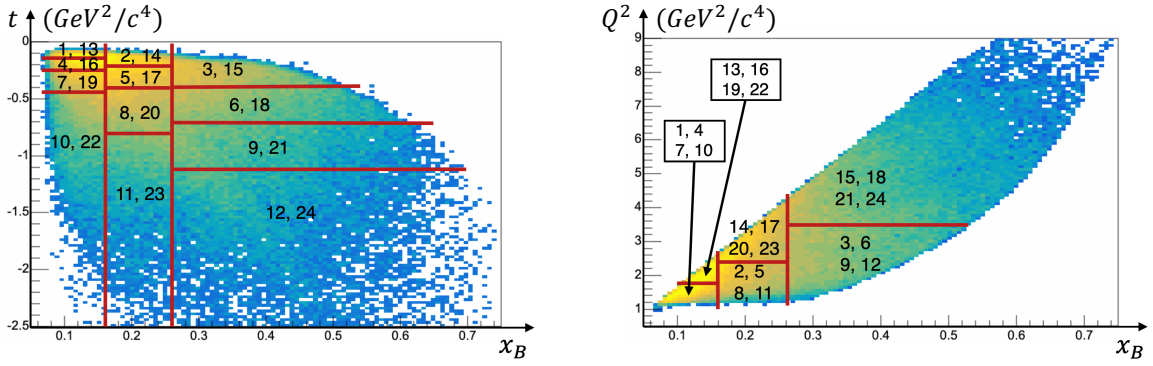

(a) in the t-x_B plane

(b) in the Q^2-x_B plane

Figure 4.4: Distribution of DVCS events and bins in x_B, t and Q^2. Bin numbers are written inside each bin, two in the t-x_B plane for low and high Q^2 bins, and four in the Q^2-x_B plane for the four different t bins.

The number of bins for each variable (4 in t, 3 in x_B, 2 in Q^2) is chosen to favor the kinematic variables t and x_B. The t dependence of the beam-spin asymmetry is probably the most

Bin	x_{Bmin}	x_{Bmax}	t_{min}	t_{max}	Q^2_{min}	Q^2_{max}
1		0.16	-0.15			1.75
2	0.16	0.26	-0.22			2.40
3	0.26		-0.40			3.25
4		0.16	-0.25	-0.15		1.75
5	0.16	0.26	-0.40	-0.22		2.40
6	0.26		-0.70	-0.40		3.25
7		0.16	-0.45	-0.25		1.75
8	0.16	0.26	-0.80	-0.40		2.40
9	0.26		-1.15	-0.70		3.25
10		0.16		-0.45		1.75
11	0.16	0.26		-0.80		2.40
12	0.26			-1.15		3.25
13		0.16	-0.15		1.75	
14	0.16	0.26	-0.22		2.40	
15	0.26		-0.40		3.25	
16		0.16	-0.25	-0.15	1.75	
17	0.16	0.26	-0.40	-0.22	2.40	
18	0.26		-0.70	-0.40	3.25	
19		0.16	-0.45	-0.25	1.75	
20	0.16	0.26	-0.80	-0.40	2.40	
21	0.26		-1.15	-0.70	3.25	
22		0.16		-0.45	1.75	
23	0.16	0.26		-0.80	2.40	
24	0.26			-1.15	3.25	

Table 4.4: Precise description of the kinematic bins

interesting from a phenomenological point of view, to study the t dependence of the shear forces and pressure distribution (see for instance [79]). The x_B variable is chosen because, the π^0 contamination mainly depends on x_B, and, because of its size, the understanding and subtraction of this contamination is one of the key points of this analysis. A fine binning in x_B allows to better separate bins that are highly contaminated from bins that are almost purely DVCS events and therefore, overall, offers a better understanding of the π^0 contamination. Finally the Q^2 dependence of the beam-spin asymmetry does not seem as crucial across the accessible range.

The size of the bins was chosen to cover the entire phase-space while keeping the number of events in each bin sufficient to perform a beam-spin asymmetry extraction. The choice of the binning was done before the background subtraction, an optimisation could be done by taking into account the π^0 background.

Each of these 24 bins is divided in 10 ϕ bins (ϕ being the angle between the leptonic and hadronic planes, with the Trento convention, as introduced in section 1.3.1). The ϕ binning is a trade-off between the number points needed to perform an harmonic analysis and the statistical significance of each point (see section 4.8 for a discussion of the uncertainties).

4.4 Selection of exclusive $ep \to ep\gamma$ events

The selection of exclusive DVCS events is performed after applying all the pre-analysis steps and after removing all the events that are identified as π^0 events, with two photons reconstructed (for the sake of simplicity, the identification of π^0 is presented later, in the π^0 background section 4.6).

Once this is done, the following DVCS exclusivity cuts are applied (motivated in sections 4.4.1, 4.4.2 and 4.4.3):

- photon cone angle:

$$\theta_{\gamma\, cone} \;<\; 1.5^\circ \tag{4.23}$$

- missing transverse momentum in $ep \to ep\gamma X$:

$$M_{p_\perp\, ep\to ep\gamma X} \;<\; 0.15\ GeV/c \tag{4.24}$$

- missing energy in $ep \to ep\gamma X$:

$$-0.5\ GeV \;<\; ME_{ep\to ep\gamma X} \;<\; 1.2\ GeV \tag{4.25}$$

- squared missing mass in $ep \to ep\gamma X$:

$$-0.04\ GeV^2/c^4 \;<\; MM^2_{ep\to ep\gamma X} \;<\; 0.04\ GeV^2/c^4 \tag{4.26}$$

- missing mass $ep \to e\gamma X$:

$$0.1\ GeV/c^2 \;<\; MM_{ep\to e\gamma X} \;<\; 1.7\ GeV/c^2 \tag{4.27}$$

Since most of the background comes from events with very low photon energy, an additional cut on the photon energy E'_q is applied (which removes only about 3% of the DVCS events in the kinematic phase-space of this analysis):

$$E'_q \;>\; 2\ GeV \tag{4.28}$$

The distribution of events for each exclusivity variable, before and after applying the exclusivity cuts, is shown on figure 4.5.

The distribution of the number of events, identified as DVCS events, for a given (Q^2, x_B, t, ϕ) bin i, noted $n_{ep\gamma,\, id}(i)$, is presented on figure 4.6.

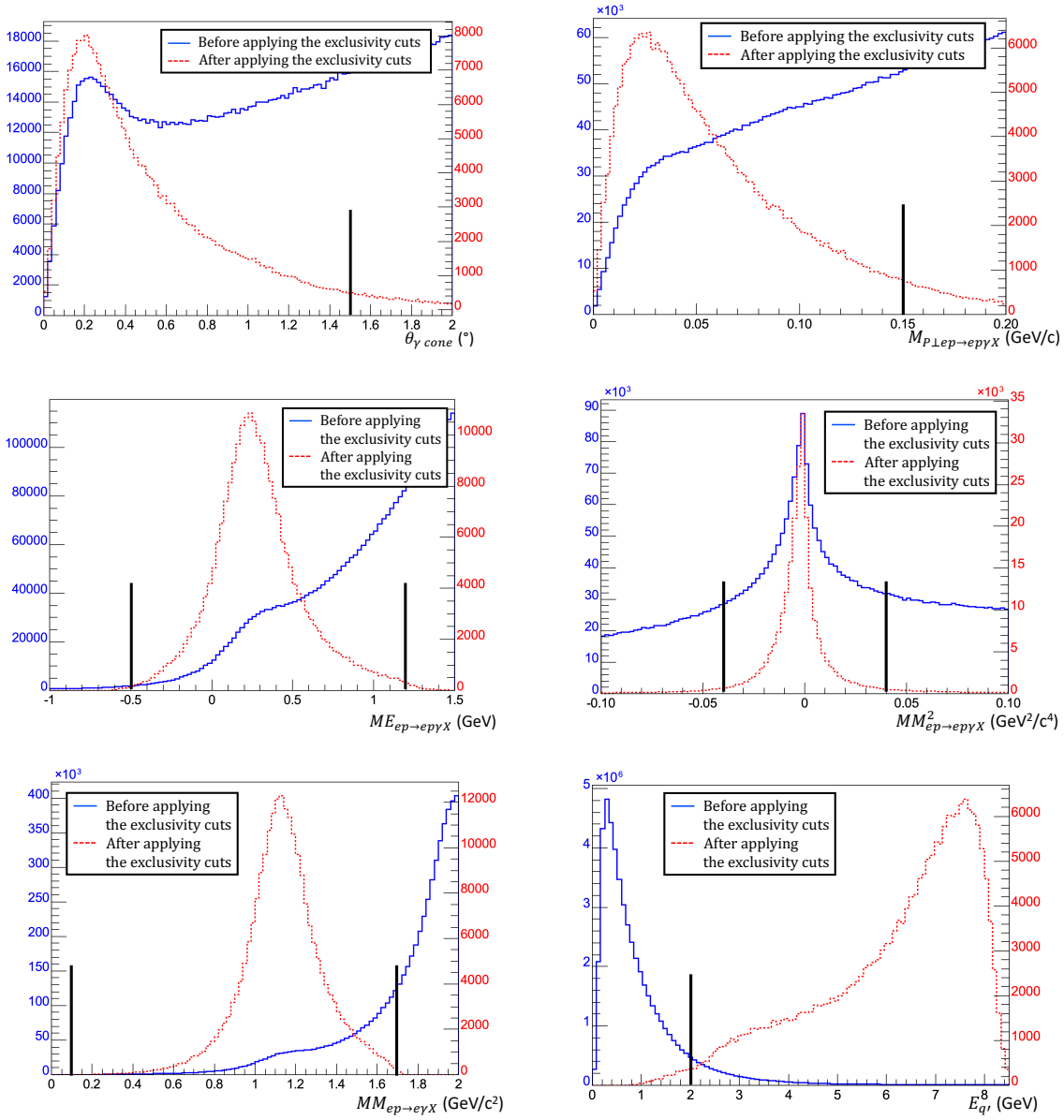

Figure 4.5: Distributions of cone angle, missing transverse momentum, missing energy and missing mass squared in $ep \to ep\gamma X$, missing mass in $ep \to e\gamma X$ and photon energy, from data. Blue curve and left axis: distributions before exclusivity cuts, red curve and right axis: after exclusivity cuts (each variable is shown after applying the cuts on all the other exclusivity variables). The position of the cuts is represented by the vertical bars.

4.4.1 Prioritisation of the exclusivity variables

In order to select the most efficient variables for identifying the photon electroproduction signal, precise studies of the exclusivity variables were performed on simulation data. The simulations contain both photon and pion electroproduction events with realistic proportions, as detailed in section 4.1.3. The priority is given to the variables that are the most discriminating, in order to keep as much DVCS as possible while rejecting as much background as possible. For each variable taken independently, a scan is performed, by taking different positions of the cuts and

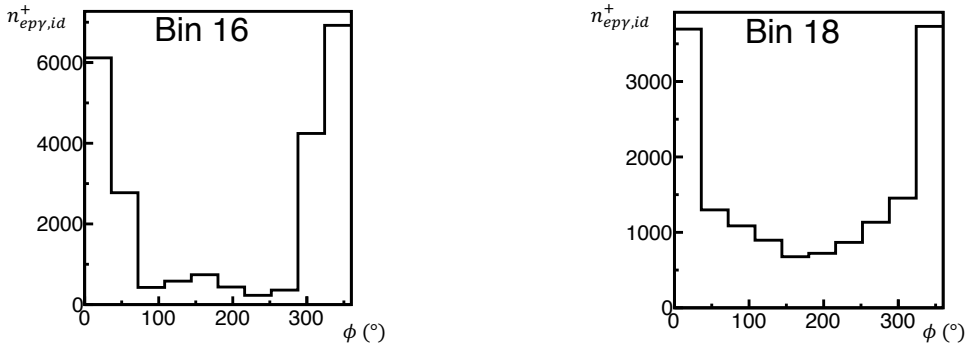

Figure 4.6: Distribution of the number of events with positive helicities that pass all the DVCS selection cuts $n^+_{ep\gamma,\,id}(i)$ as a function of the angle ϕ for two typical kinematic bins. The other bins are presented in the appendix, on figure A.5.

the efficiency of the cut is computed for each position.

To quantify the results, two fractions have been defined: the "efficiency" of the cut, and the "contamination" fraction associated with the cut. The "efficiency" is defined as the fraction of DVCS events that are kept after applying the cut. The "contamination" fraction is defined as the number of π^0 events that are kept after applying the cut, divided by the total number of events after the cut.

The results, see figure 4.7, show that the photon cone angle and the missing transverse momentum are overall the most discriminating variables, followed by the missing energy. The missing mass squared $MM^2_{ep\to ep\gamma X}$ is not very discriminating since, for both DVCS and π^0 events, the variable is null for ideal events. The results from figure 4.7 could potentially be used to determine the position of the cuts. In this analysis however, a different method is used to optimise the position of the cuts, detailed in section 4.4.2.

4.4.2 Optimisation of the exclusivity cuts on the simulation

As described above in section 4.4.1, the position of the exclusivity cuts is a tradeoff between the fraction of background removed and the fraction of signal kept. In this analysis, the choice was made to cut at the position that minimizes the beam-spin asymmetry statistical uncertainty around $\phi = 90°$ from a simulation. The area around the angle $\phi = 90°$ is the region that has the highest asymmetry and therefore is driving the fit of the amplitude of the BSA. It is also an angle for which the π^0 electroproduction cross-section, and therefore, the contamination from π^0 events, is generally high (see section 4.6.2). It is therefore the region that is the most interesting to optimize. The statistical uncertainty $\Delta A_{LU,\,\pi^0\,corr}$, used here, is defined in section 4.8.1. This statistical uncertainty includes the DVCS selection and the π^0 correction. This study starts from wide exclusivity cuts for all the variables and refines the cuts, one variable at a time. The priority is given to the most discriminating variables, based on the results from section 4.4.1.

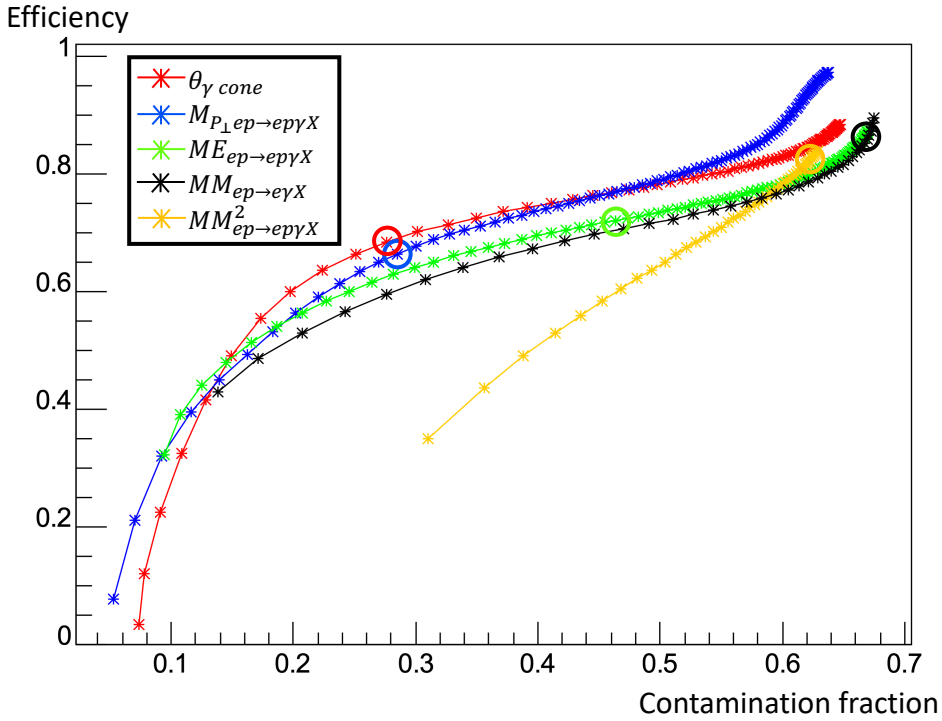

Figure 4.7: Efficiency as a function of the contamination fraction for different cut positions for each exclusivity variable (all analysed independently) from simulation. The circles correspond to the final position of the DVCS selection cuts for the simulation (obtained in section 4.4.2). The photon cone angle and the missing transverse momentum are overall the most discriminating variables.

The position of the cut is varied, step by step, to find if an optimal cut position exists.

The first variable studied is the photon cone angle. The BSA statistical uncertainty as a function of the position of the photon cone angle cut is shown on figure 4.8. A minimum is clearly visible for bins with high x_B (such as bin 18), while, for bins with low x_B (such as bin 16), the statistical uncertainty rapidly decreases and then stays constant when the position of the cut increases. This behavior is mainly related to the level of pion contamination for each bin. Low x_B bins have a very small contamination (see section 4.6), therefore the behavior of the statistical uncertainty is dominated by the DVCS statistics. High x_B bins generally have a relatively high contamination (see section 4.6). In this case, since most of the DVCS signal is concentrated close to $\theta_{\gamma\,cone} = 0$ while the π^0 signal has a broad distribution (as shown on figure 4.9), the statistical uncertainty tends to decrease first, when most of the signal selected is DVCS, and then increases as more and more π^0 events are being selected. Since the contamination is negligible for this study in low x_B bins, any value above 0.5° for the photon cone angle cut is acceptable to keep almost all the DVCS statistics. The optimised position of the cut for bins with contamination is obtained for $\theta_{\gamma\,cone} \simeq 0.5^\circ$. It is noticeable that this value is similar for all the kinematic bins when a minimum exists. The choice to position the cut photon cone angle cut for $\theta_{\gamma\,cone} = 0.5^\circ$ is therefore satisfying, over the entire kinematic phase-space.

The same stategy is applied to the second most discriminating variable: the missing trans-

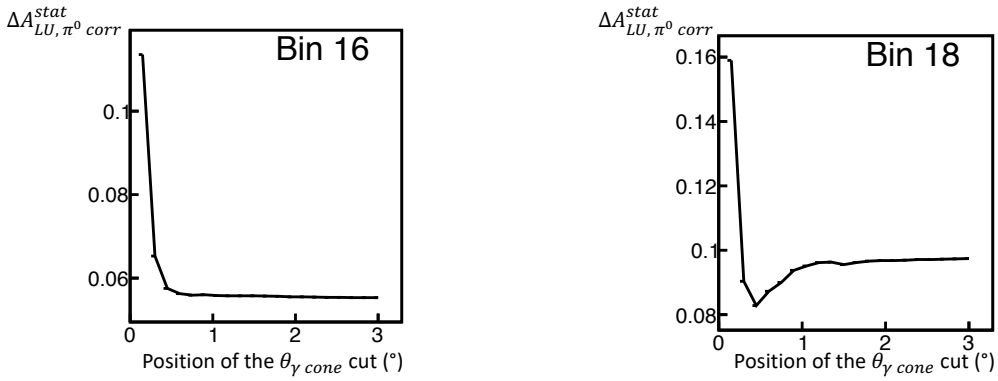

Figure 4.8: Beam-spin asymmetry statistical uncertainty around $\phi = 90°$ as a function of the position of the photon cone angle cut for the kinematic bins 16 (left) and 18 (right) from simulation. Wide exclusivity cuts are used for all the other exclusivity variables. The other bins are presented in the appendix, on figure A.6.

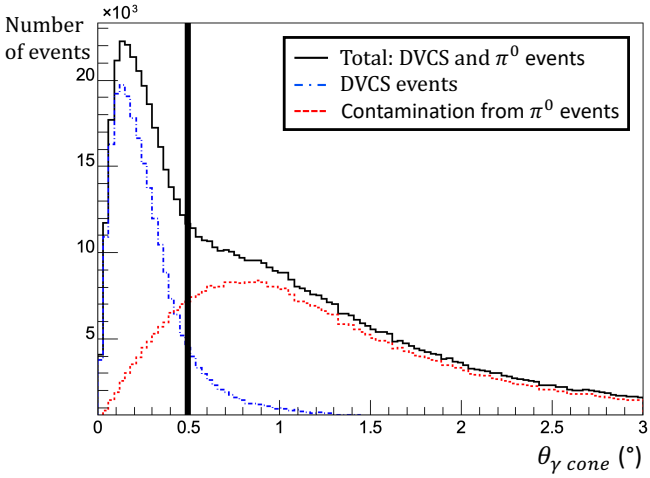

Figure 4.9: Distribution of the number of DVCS and π^0 events as a function of the photon cone angle from simulation. The vertical black bar represents the final position of the photon cone angle cut.

verse momentum, after applying the optimised photon cone angle cut (and keeping cuts wide for all the other exclusivity variables). The statistical uncertainty as a function of the position of the missing transverse momentum cut is shown on figure 4.10. The same behavior is observed with a minimum around $0.12\,\mathrm{GeV/c}$. Following the same reasoning, the optimised missing transverse momentum cut position on the simulation is set to $M_{p_\perp\ ep\to ep\gamma X}$ =$0.12\,\mathrm{GeV/c}$ for all the kinematic bins.

This process is then applied to the third most discriminating variable: the missing energy in $ep \to ep\gamma X$. However, when the optimised photon cone angle and missing transverse momentum cuts are used, the missing energy $ME_{ep\to ep\gamma X}$ does not really reveal any minimum as shown on figure A.8. Note that, when the photon cone angle and missing transverse momentum cuts are not optimised, and wide cuts are used for all the exclusivity variables, the missing energy does have a minimum, as shown in the appendix, on figure A.9. This is an evidence that the selection

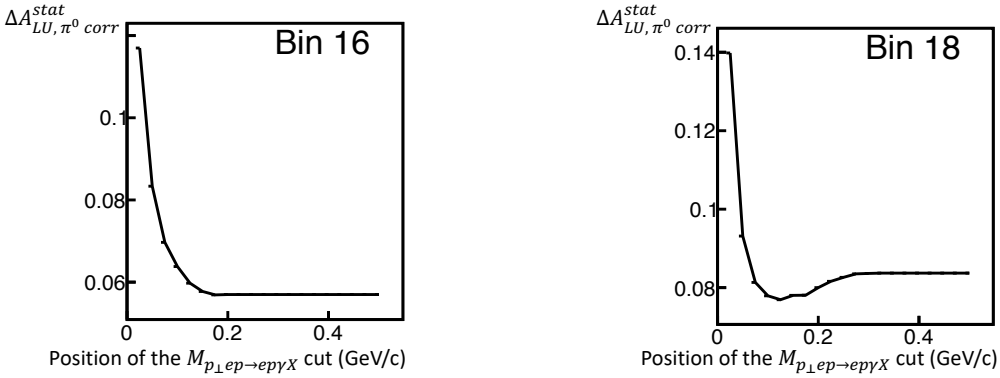

Figure 4.10: Beam-spin asymmetry statistical uncertainty around $\phi = 90^\circ$ as a function of the position of the missing transverse momentum in $ep \to ep\gamma X$ cut for the kinematic bins 16 (left) and 18 (right) from simulation. The photon cone angle cut position is optimised and wide exclusivity cuts are used on all the other exclusivity variables. The other bins are presented in the appendix, on figure A.7.

of DVCS events with the optimised photon cone angle and missing transverse momentum cuts is sufficient to remove as much π^0 contamination as possible while keeping a large fraction of DVCS events. Optimised exclusivity cuts are therefore applied only to $\theta_{\gamma\,cone}$ and $M_{p_\perp\ ep\to ep\gamma X}$. The wide exclusivity cuts are therefore kept for the remaining exclusivity variables $ME_{ep\to ep\gamma X}$, $MM^2_{ep\to ep\gamma X}$ and $MM_{ep\to e\gamma X}$.

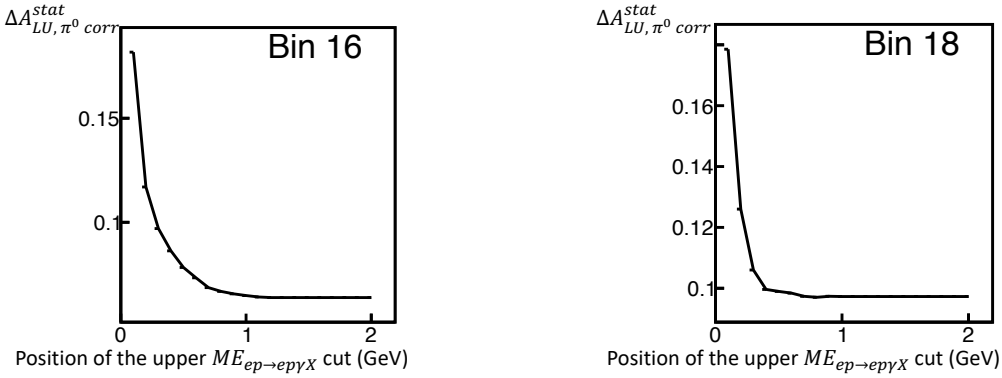

Figure 4.11: Beam-spin asymmetry statistical uncertainty around $\phi = 90^\circ$ as a function of the position of the missing energy in $ep \to ep\gamma X$ cut for the kinematic bins 16 (left) and 18 (right) from simulation. The photon cone angle and missing transverse momentum cut positions are optimised and wide exclusivity cuts are used on the other exclusivity variables. The other bins are presented in the appendix, on figure A.8.

The final cuts for the selection of DVCS events from the simulation are:

$$\theta_{\gamma\,cone} \ < \ 0.5^\circ \tag{4.29}$$

$$M_{p_\perp\ ep\to ep\gamma X} \ < \ 0.12\ GeV/c \tag{4.30}$$

$$-0.5\ GeV \ < \ ME_{ep\to ep\gamma X} \ < \ 1.2\ GeV \tag{4.31}$$

$$-0.04\ GeV^2/c^4 \ < \ MM^2_{ep\to ep\gamma X} \ < \ 0.04\ GeV^2/c^4 \tag{4.32}$$

$$0.1\ GeV/c^2 \ < \ MM_{ep\to e\gamma X} \ < \ 1.7\ GeV/c^2 \tag{4.33}$$

4.4.3 Adaptation of the exclusivity cuts to data

The optimisation of the exclusivity cuts presented in the previous sections 4.4.1 and 4.4.2 is based on a simulation, since, in this case, the real background contamination is perfectly known. To adapt the cuts from simulation to data, resolutions from simulation and data have been compared. Distributions of cone angle in the simulation and data are shown on the left on figure 4.12. In order to estimate the resolution of the distributions from a simple fit function, the distributions have been symmetrized about the y-axis and the bins around $\theta_{\gamma\,cone} = 0°$, that exhibit a different behavior due to phase space effects have not been used, as shown on the middle and right on figure 4.12. The position of the cut in the data is obtained from the position in the simulation, scaled by the ratio of resolutions. The final photon cone angle cut position in the data is $\theta_{\gamma\,cone} = 1.5°$.

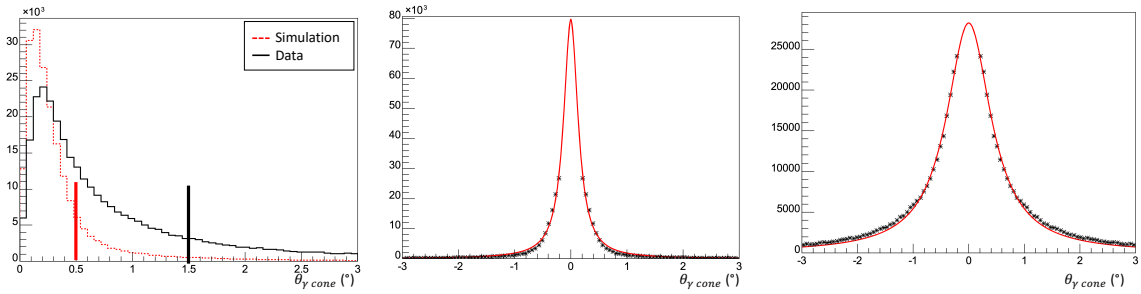

Figure 4.12: Distribution of photon cone angle in the simulation and data (left) with the final position of the cuts shown with vertical bars. To estimate the resolutions of these distributions from simple fits,in the simulation (middle) and in the data (right), the initial distributions are symmetrized and the bins around $\theta_{\gamma\,cone} = 0°$ are not considered. The resulutions are then obtained with a Lorentzian fit: the resolutions are 0.155° in the simulation and 0.48° in the data. Wide exclusivity cut are used for all exclusivity variables.

The same strategy is then used to obtain the missing transverse momentum cut position in the data. Distributions from simulations and data are shown in figure 4.13. The final missing transverse momentum cut position in the data is $M_{p_\perp\ ep\to ep\gamma X}$ =0.15 GeV/c.

After application of the optimised cut positions on $\theta_{\gamma\,cone}$ and $M_{p_\perp\ ep\to ep\gamma X}$, the impact of the three remaining variables $ME_{ep\to ep\gamma X}$, $MM^2_{ep\to ep\gamma X}$ and $MM_{ep\to e\gamma X}$ is small, as shown in section 4.4.2. They are mainly applied to remove outlier events. The wide exclusivity cuts from

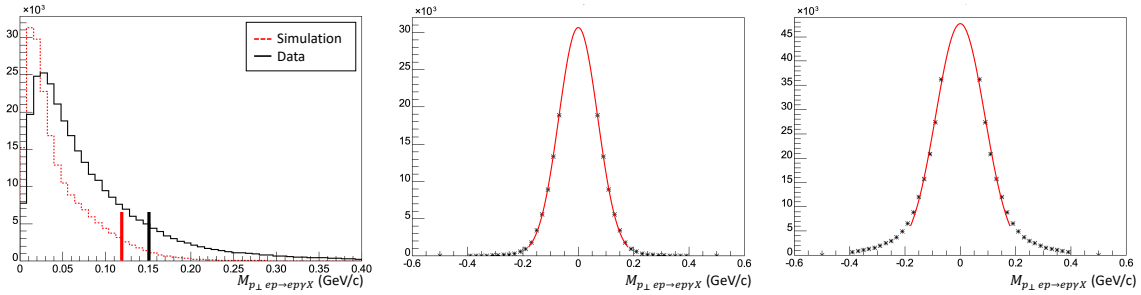

Figure 4.13: Distribution of missing transverse momentum in $ep \to ep\gamma X$ in the simulation and data (left), with the final position of the cuts shown with vertical bars. To estimate the resolutions of these distributions from simple fits, in the simulation (middle) and in the data (right), the distributions are symmetrized and the bins around $M_{p_\perp\, ep\to ep\gamma X} = 0\,\mathrm{GeV/c}$ are not considered. The resulutions are then obtained with a Gaussian fit: the resolutions are $0.070\,\mathrm{GeV/c}$ in the simulation and $0.088\,\mathrm{GeV/c}$ in the data. Wide exclusivity cut are used for all exclusivity variables.

the simulation are therefore kept to analyse the data.

The optimised cuts for the selection of DVCS events from data are:

$$\theta_{\gamma\, cone} \;<\; 1.5^\circ \tag{4.34}$$

$$M_{p_\perp\, ep\to ep\gamma X} \;<\; 0.15\ GeV/c \tag{4.35}$$

$$-0.5\ GeV \;<\; ME_{ep\to ep\gamma X} \;<\; 1.2\ GeV \tag{4.36}$$

$$-0.04\ GeV^2/c^4 \;<\; MM^2_{ep\to ep\gamma X} \;<\; 0.04\ GeV^2/c^4 \tag{4.37}$$

$$0.1\ GeV/c^2 \;<\; MM_{ep\to e\gamma X} \;<\; 1.7\ GeV/c^2 \tag{4.38}$$

4.5 Raw asymmetries of $ep \to ep\gamma$ events

Raw beam-spin asymmetries are calculated for events that pass the DVCS selection cuts described in section 4.4. At this stage, only events that are identified as π^0 events, with two photons reconstructed, are removed and no additional corrections for pion electroproduction contamination are applied, these asymmetries are called "raw".

Asymmetries for a (Q^2, x_B, t, ϕ) bin i are computed with the following equation:

$$A_{LU,\,raw}(i) = \frac{1}{P}\,\frac{N^+_{raw}(i) - N^-_{raw}(i)}{N^+_{raw}(i) + N^-_{raw}(i)} \tag{4.39}$$

with, for the raw beam-spin asymmetries, the following notations:

- P is the beam polarization: $P = 0.863$ with an uncertainty $\Delta P = 0.037$ measured from Møller polarimetry as explained in section 2.2.1
- $N^{\pm}_{raw}(i) = \frac{n^{\pm}_{ep\gamma,\,id}(i)}{C^{\pm}}$, the number of identified DVCS events $n^{\pm}_{ep\gamma,\,id}(i)$ with a beam helicity $\pm$, in a given (Q^2, x_B, t, ϕ) bin i, normalized by the total accumulated charge $C^{\pm}$.

Following the assumptions mentioned in section 1.3.3, the ϕ distribution of beam-spin asymmetries in each (Q^2, x_B, t) bin are fitted with two parameters p_0 and p_1 using the following form:

$$\frac{p_0\ sin(\phi)}{1 + p_1\ cos(\phi)} \tag{4.40}$$

At this stage, only the statistical uncertainty $\Delta A^{stat}_{LU,raw}$ is taken into account (details about the calculation of statistical uncertainties are given in section 4.8.1):

$$\Delta A^{stat}_{LU,\,raw}(i) = \frac{2}{P}\ \frac{\sqrt{\left[N^{-}_{raw}(i)\ \Delta N^{+}_{raw}(i)\right]^2 + \left[N^{+}_{raw}(i)\ \Delta N^{-}_{raw}(i)\right]^2}}{\left[N^{+}_{raw}(i) + N^{-}_{raw}(i)\right]^2} \tag{4.41}$$

with

$$\Delta N^{\pm}_{raw}(i) = \frac{1}{C^{\pm}}\sqrt{n^{\pm}_{ep\gamma,\,id}(i)} \tag{4.42}$$

The results are shown on figure 4.14 with the fit parameters obtained for each kinematic bin. The behavior of the BSA greatly depends on the kinematic bins. High x_B and high $|t|$ bins (such as bins 9, 11, 12, 21, 23 or 24) have an amplitude much lower (p_0 between $\simeq 0.05$ and $\simeq 0.2$) than low x_B and low $|t|$ bins (such as bins 1, 2, 4, 13, 14 or 16) for which the amplitude reaches about 0.25. For the raw BSA, the parameter p_1 is always negative, varying between $\simeq 0$ and $\simeq -0.8$ with the tendency to decrease for high x_B and high $|t|$ bins. Low Q^2 bins (bins 1 to 12) have a lower amplitude than high Q^2 bins (bins 13 to 24) but, at this stage, the effect of Q^2 is overall relatively small compared to x_B and t.

4.6 π^0 electroproduction background

As mentioned in section 4.1.2, π^0 electroproduction is the main source of background and cannot be fully removed by exclusivity cuts. The subtraction of π^0 events is done in two steps:

- a first subtraction is applied before the selection of DVCS events, for π^0 events that can be identified. In this case, the two photons from the π^0 decay are correctly reconstructed and allow an identification of the event using π^0 exclusivity cuts described in section 4.6.1
- a second subtraction is applied after the selection of DVCS, for π^0 events that resemble DVCS events too much to be removed by exclusivity cuts. In this case, in which one

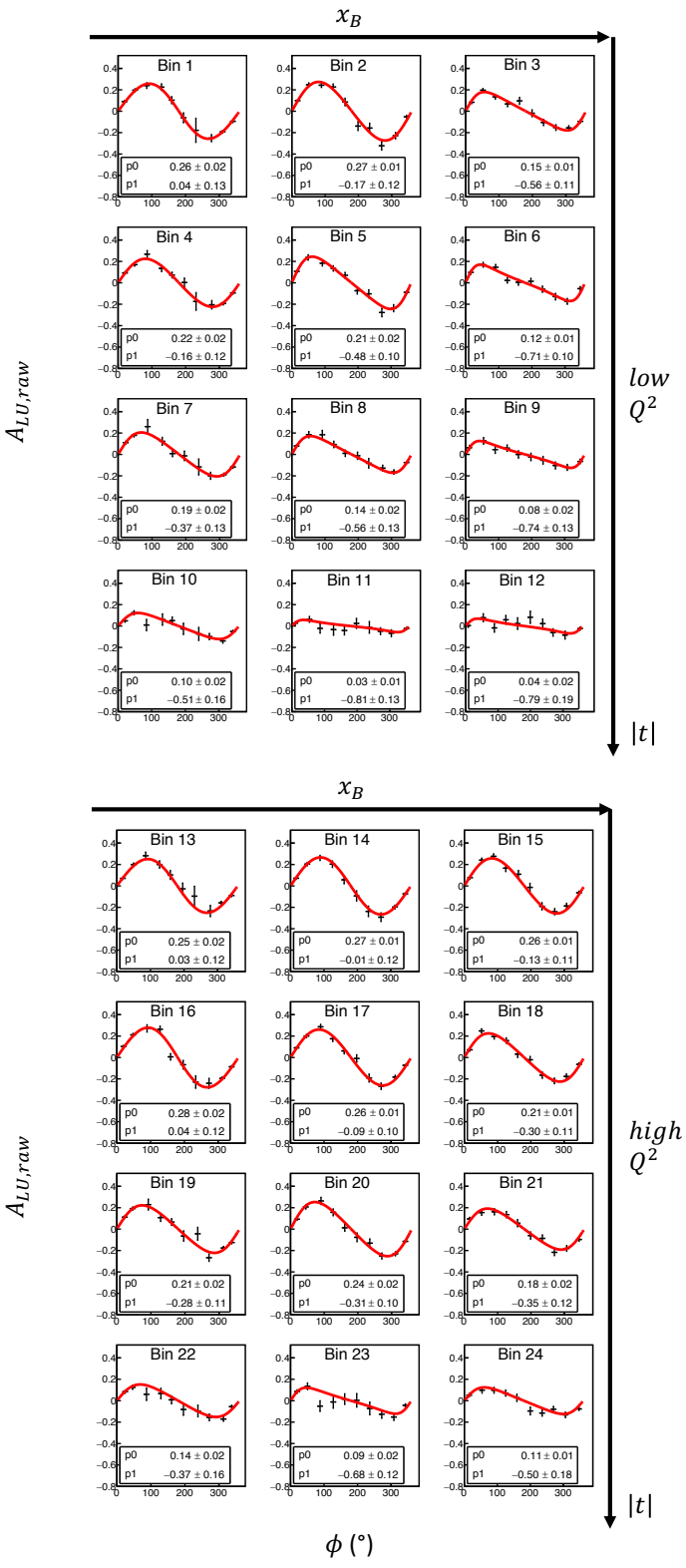

Figure 4.14: DVCS raw beam-spin asymmetries $A_{LU,\,raw}$ as a function of ϕ for each (Q^2, x_B, t) bin. The fit function 4.40 is used. The statistical uncertainty $\Delta^{stat}_{LU,\,raw}$ is considered here, following the definitions from section 4.8.1.

of the two photons from the π^0 decay generally carries a very small amount of energy and is not detected, the π^0 event behaves like a DVCS event and cannot be identified from data. The π^0 events that are not identified and pass the DVCS selection are called "π^0 contamination" events and are estimated and subtracted using a simulation. The π^0 contamination correction is detailed in section 4.6.2.

4.6.1 Selection of exclusive π^0 electroproduction events

π^0 electroproduction events for which the two photons are correctly reconstructed can be identified using exclusivity cuts. The selection of the exclusive π^0 events in the data is done with the following exclusivity cuts (motivated below):

- π^0 cone angle:

$$\theta_{\pi^0\, cone} \;<\; 4.5^\circ \tag{4.43}$$

- π^0 invariant mass:

$$0.073\ GeV/c^2 \;<\; M_{\gamma\gamma} \;<\; 0.193\ GeV/c^2 \tag{4.44}$$

- squared missing mass in $ep \to ep\gamma\gamma X$:

$$-0.075\ GeV^2/c^4 \;<\; MM^2_{ep\to ep\gamma\gamma X} \;<\; 0.075\ GeV^2/c^4 \tag{4.45}$$

- missing energy in $ep \to ep\gamma\gamma X$:

$$-1\ GeV \;<\; ME_{ep\to ep\gamma\gamma X} \;<\; 1.8\ GeV \tag{4.46}$$

These cuts are based on a π^0 electroproduction simulation. With a π^0 simulation, the distribution for each exclusivity variable is fitted and cuts are positioned at about five standard deviations as shown on figure 4.15. The position of the cuts in the data is obtained by scaling the position of the cuts in the simulation by the ratio of resolutions.

The distribution of the number of events, identified as π^0 events, in the data, for a given (Q^2, x_B, t, ϕ) bin i, noted $n_{\pi^0,\, id}(i)$, is presented on figure 4.16. This number of π^0 events strongly depends on the kinematic variables, increasing with x_B and with $|t|$, to reach roughly ten times more events in bins 12 and 24 than in bins 1 and 13. These dependences are largely explained by the dependence of the π^0 electroproduction cross-section and the choice of binning made in this analysis (the bins are much larger at high x_B and high $|t|$).

As explained in section 4.4, to reduce the π^0 contamination, the events that pass the π^0 exclusivity cuts are removed from the DVCS candidates and are not considered in the DVCS selection.

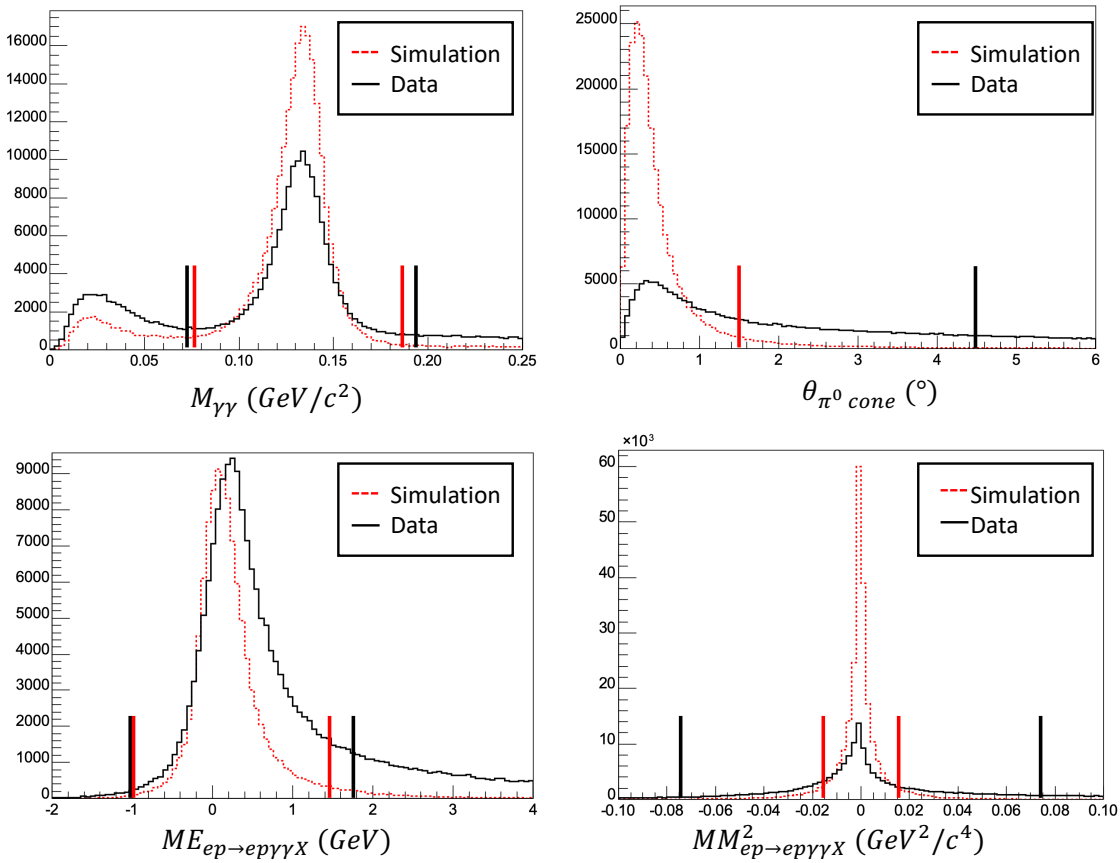

Figure 4.15: π^0 exclusivity variables and cuts for simulation and data (vertical bars represent the position of the cuts). Each variable is shown after applying all the other exclusivity variables. The simulation is normalized to have the same number of events as the data.

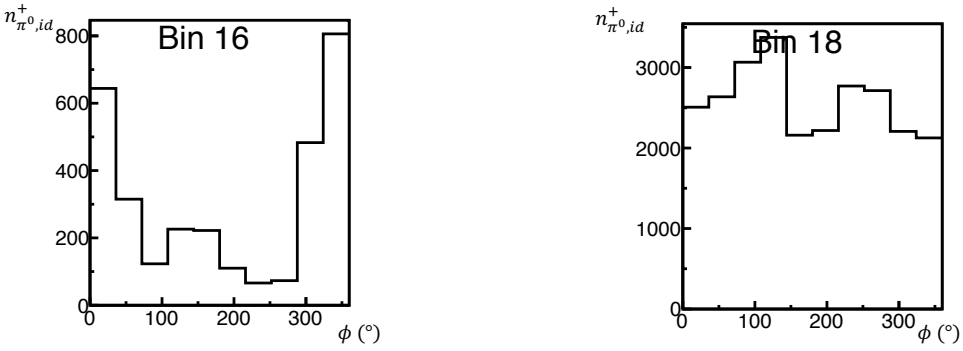

Figure 4.16: Distribution of the number of events with positive helicities that pass all the π^0 selection cuts $n^+_{\pi^0,\,id}(i)$ as a function of the angle ϕ for two typical kinematic bins. The other bins are presented in the appendix, on figure A.10.

4.6.2 Correction of the contamination from π^0 electroproduction events

Estimation of the π^0 contamination

For each (Q^2, x_B, t, ϕ) bin i, an estimation of the number of contamination events (π^0 events that pass the DVCS selection described in section 4.4), in the data, noted $n_{\pi^0,cont}(i)$ is performed. This estimation is based on the number of π^0 events identified by the π^0 selection (described in section 4.6.1), in the data, noted $n_{\pi^0,\,id}(i)$. The ratio between these two numbers is noted $r(i)$ such that:

$$n_{\pi^0,\,cont}(i) = r(i)\; n_{\pi^0,\,id}(i) \tag{4.47}$$

This ratio can be interpreted as the ratio between the "size" of the phase space for the π^0 decays that are selected as DVCS events and the "size" of the phase space for decays that are selected as π^0 events in the data. Since $n_{\pi^0,\,id}(i)$ has already been computed in section 4.6.1, on figure 4.16, an estimation of $r(i)$ directly provides access to an estimation of the π^0 contamination.

In this analysis, this ratio is assumed to be the same in the data and in the simulation:

$$r(i) = r^{simu}(i) \tag{4.48}$$

To estimate $r^{simu}(i)$, exclusive π^0 events are generated and injected in the simulation. After application of the pre-selection, described in section 4.2, the π^0 exclusivity cuts (using the position of the cuts adjusted for the simulation as explained in section 4.6.1) are applied and the number of events identied as π^0, noted $n^{simu}_{\pi^0,\,id}(i)$ is computed. In a similar way, to access the π^0 contamination, the DVCS exclusivity cuts are applied to the pre-selected events that are not identified by the π^0 exclusivity cuts, the number of π^0 contamination events is noted $n^{simu}_{\pi^0,\,cont}(i)$. The ratio $r(i)$ is then estimated as follows:

$$r(i) = r^{simu}(i) = \frac{n^{simu}_{\pi^0,\,cont}(i)}{n^{simu}_{\pi^0,\,id}(i)} \tag{4.49}$$

Results for $r^{simu}(i)$ from simulation are presented on figure 4.17. For most of the bins, the value of $r^{simu}(i)$ is between 0.05 and about 0.25.

Since $r(i)$ corresponds to a ratio of sizes of phase space for π^0 decays, this assumption could be inexact if inaccuracies in the simulation affect differently the phase space of identified π^0 decays and the phase space of π^0 contamination decays. This can be the case, for instance, if detector inefficiencies are not properly simulated. A systematic uncertainty, detailed in section 4.8.2 is therefore associated, in the final results, with the π^0 contamination correction.

The estimation of the π^0 contamination $n_{\pi^0,\,cont}(i)$, computed with the equation 4.47 and the results for $n_{\pi^0,\,id}(i)$ from figure 4.16 and for $r(i)$ from figure 4.17 is presented on figure 4.18. The contamination may vary significantly from one bin to another: increasing with x_B and with $|t|$. While the contamination fraction is almost null for low x_B and low $|t|$ bins (such as bins 1

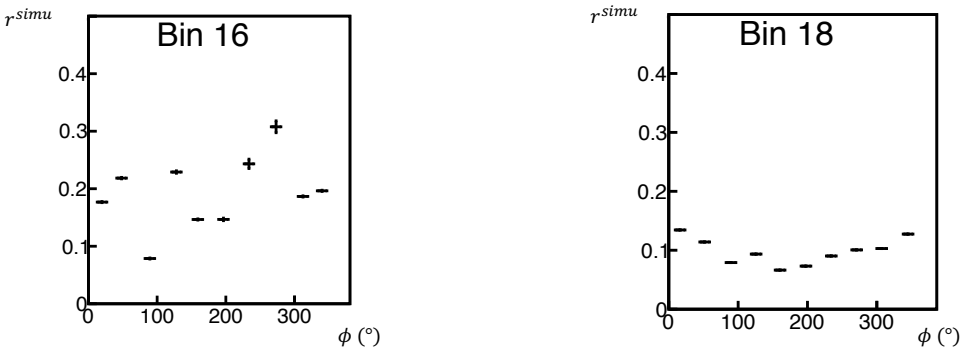

Figure 4.17: Ratio r^{simu} of the contamination from π^0 events divided by the number of identified π^0 events as a function of the angle ϕ for two typical kinematic bins, with statistical uncertainties (defined in section 4.8.1). The other bins are presented in the appendix, on figure A.11.

and 13), it can be higher than 50% for high x_B and high $|t|$ bins. The contamination also tends to decrease when Q^2 increases. Since the kinematic dependences of $r(i)$ (from figure 4.17) are small compared to the dependences of $n_{\pi^0,\,id}(i)$ (from figure 4.16), the contamination is largely driven by the number of identified π^0 events and therefore the π^0 cross-section.

Correction of the π^0 contamination

In order to correct for the contamination estimated above, the contamination is subtracted from the number of identified DVCS events. The beam-spin asymmetry corrected for π^0 contamination is computed from equation 4.39, with a redefinition of the number of events $N^{\pm}_{\pi^0\,corr}(i)$:

$$N^{\pm}_{\pi^0\,corr}(i) = \frac{n^{\pm}_{ep\gamma,\,id}(i) - n^{\pm}_{\pi^0,\,cont}(i)}{C^{\pm}} \tag{4.50}$$

The BSA $A_{LU,\,\pi^0\,corr}$, obtained after application of the π^0 contamination correction, is shown on figure 4.19 and a comparison with the raw BSA is shown on figure 4.20. The uncertainties are statistical only, and include the propagation of the statistical uncertainties associated with the π^0 contamination, as defined in section 4.8.1. As expected, the raw beam-spin asymmetries (see figure 4.14) for low x_B and low $|t|$ are barely affected by the π^0 contamination correction, while the impact is significant for high x_B and high $|t|$ regions. One can also notice that the statistical uncertainties of the corrected BSA are largely increased in the highly contaminated regions compared to the raw BSA. The ϕ dependence is fitted with the function from 4.40, note that the fit does not describe the data well in some of the highly contaminated bins (such as bins 11, 12), for ϕ angles between 90° and 270°.

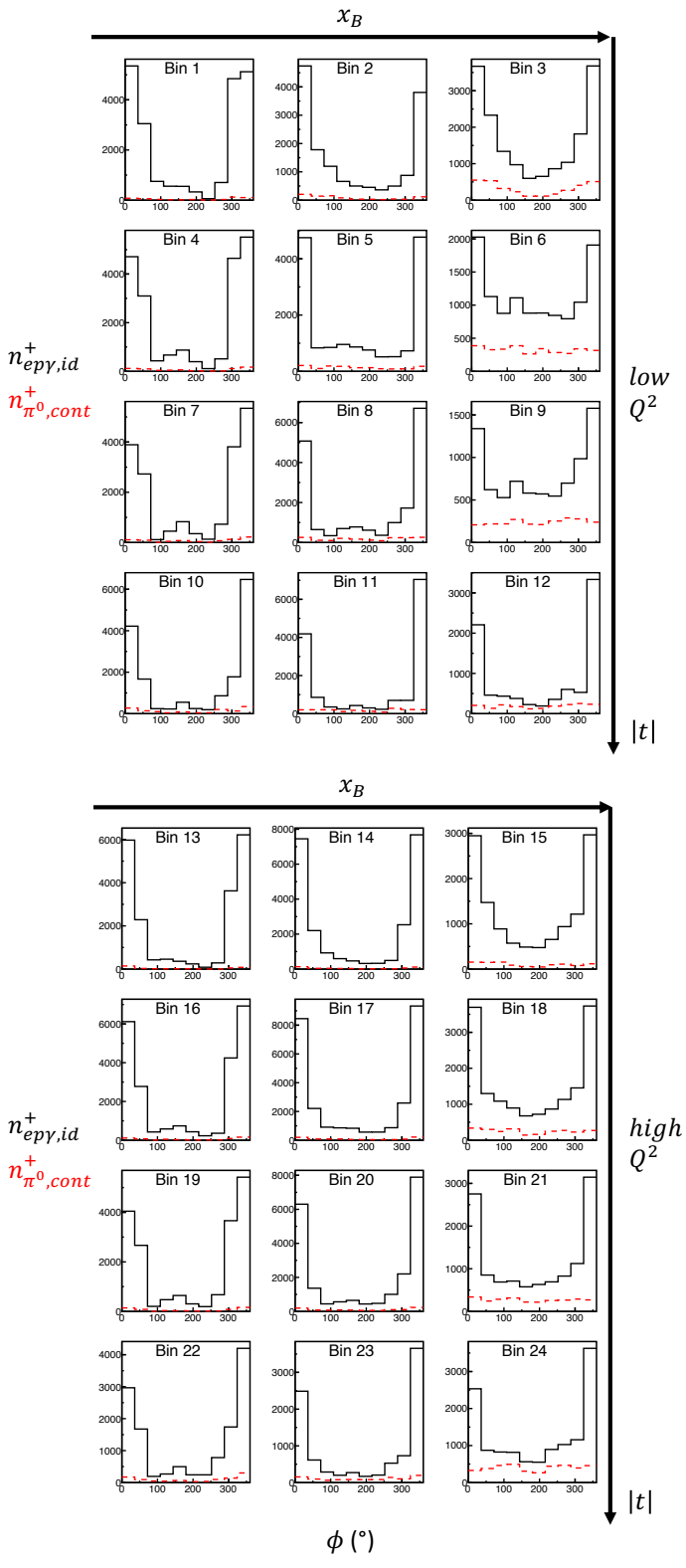

Figure 4.18: Estimated π^0 contamination among the DVCS selection for positive beam helicity. In continuous black, the number of events that pass the DVCS selection cuts $n^+_{ep\gamma,\,id}(i)$. In dashed red, the estimated contamination from π^0 events $n^+_{\pi^0,\,cont}(i)$.

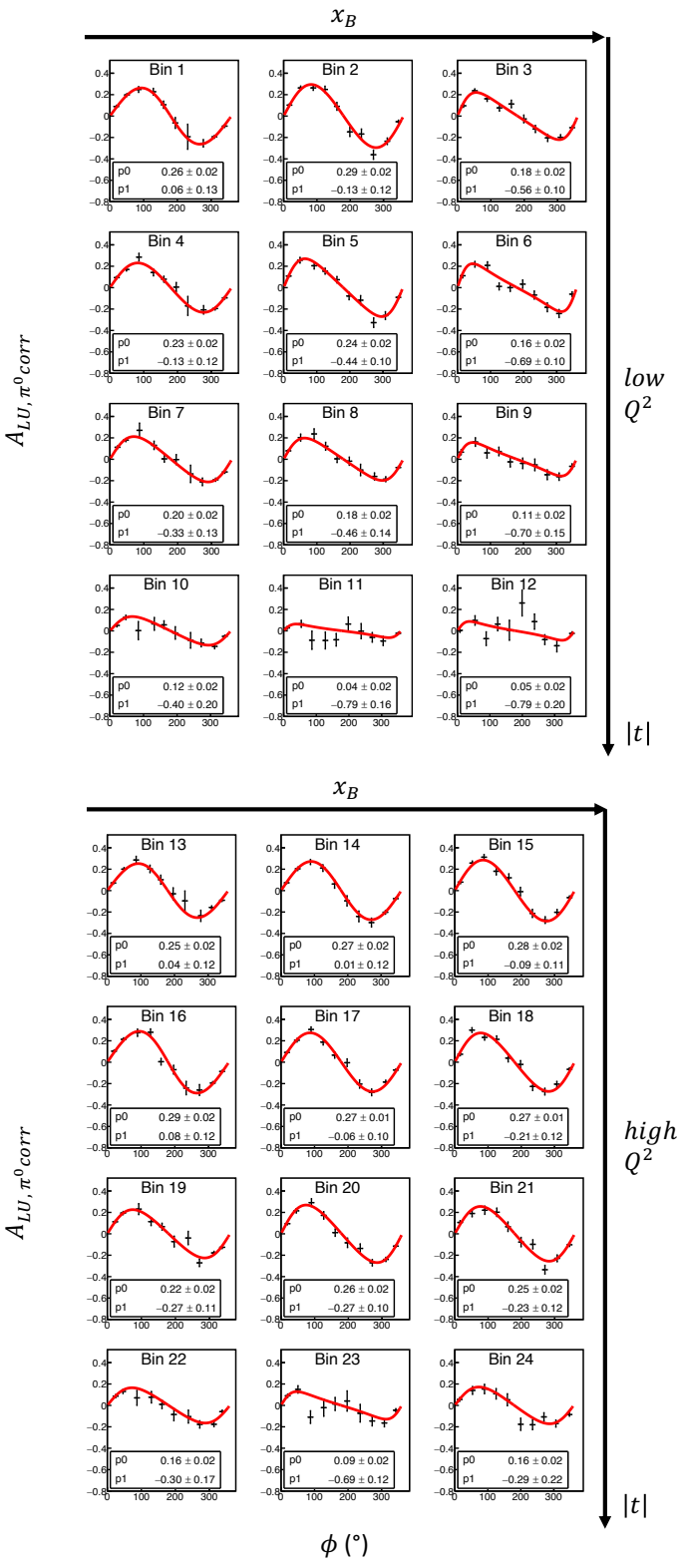

Figure 4.19: DVCS beam-spin asymmetry $A_{LU,\pi^0\,corr}$, corrected for π^0 contamination, as a function of ϕ for each (Q^2, x_B, t) bin. The fit function 4.40 is used. The statistical uncertainty $\Delta^{stat}_{LU,\pi^0\,corr}$ is considered here, including the contribution from the π^0 contamination correction, following the definitions from section 4.8.1.

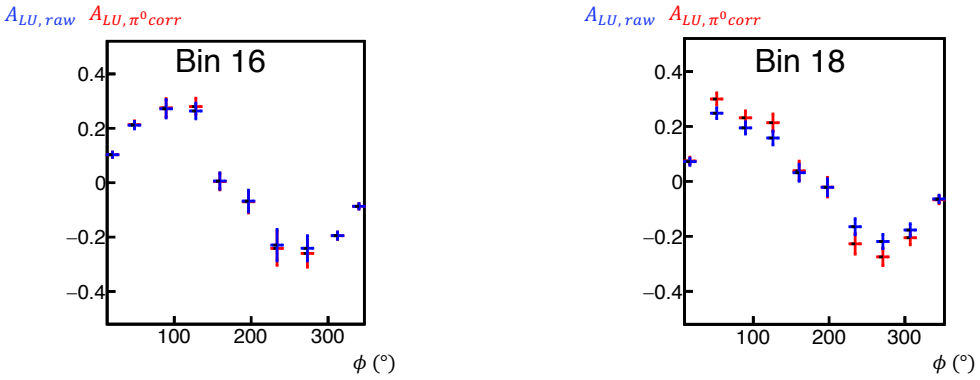

Figure 4.20: Comparison of the raw BSA (in blue) and the BSA after π^0 contamination correction (in red) for two typical kinematic bins, with statistical uncertainties (defined in section 4.8.1).The other bins are presented in the appendix, on figure A.12.

4.7 Bin migration

4.7.1 Description of the bin migration

Bin migration is the phenomenon in which events that physically correspond to a (Q^2, x_B, t, ϕ) bin j are reconstructed in another bin i. This migration is expected to come from energy losses or multiple scattering caused by the interactions of the particles with the CLAS12 spectrometer. Energy losses, for instance from radiative effects, where a photon is radiated by the electron, at the vertex or as it goes through matter in the detectors, can provoke shifts of the four-momentum reconstructed for the electron and, therefore, shifts of the kinematic variables and bin migration.

To estimate the migration of events from a bin j to another bin i, a DVCS simulation was used. For each event reconstructed in a bin i, the generated kinematic variables were used to identify the initial bin. A migration matrix, noted $M_{j\to i}$, is therefore obtained, containing for any bin i and j, the number of events that were generated in the bin j and are reconstructed in the bin i. The distributions for two typical bins are shown in the appendix, on figures A.13 and A.14.

This estimation can, at least partially, take into account the energy losses and the multiple scattering since these effects are included in the simulation. A systematic uncertainty, defined in section 4.8.2, is associated with the bin migration matrix elements to include the remaining sources of bin migration (such as the internal radiative effects).

4.7.2 Correction of the bin migration

To derive a correction for the bin migration, the BSA is first decomposed into the following form:

$$A_{LU,\,\pi^0\,corr}(i) = m_{i\to i}\, A_{LU,\,corr}(i\to i) + \sum_{bin\ j\neq i} m_{j\to i}\, A_{LU,\,corr}(j\to i) \tag{4.51}$$

with:

- $A_{LU,\,\pi^0\,corr}(i)$ is the BSA of all the events that are reconstructed in the bin i, including the π^0 contamination, and including events coming from bin migration (this is the BSA measured in section 4.6.2).
- $A_{LU,\,corr}(j \to i)$ is the BSA of the events from the bin j that are reconstructed in the bin i
- $m_{j\to i}$ is the fraction of events reconstructed in the bin i that are coming from the bin j (note that $m_{j\to i} = 1 - \sum_{bin\ k\neq j} m_{k\to i}$)

The goal of the bin migration correction is to obtain an estimation of $A_{LU,\,corr}(i \to i)$, which is the BSA corrected for π^0 contamination and bin migration. To simplify the notation, we note $A_{LU,\,corr}(i)$ instead of $A_{LU,\,corr}(i \to i)$ and we omit the subscript "LU". From equation 4.51, $A_{corr}(i)$ can be written as:

$$A_{corr}(i) = \frac{A_{\pi^0\,corr}(i) - \sum_{bin\ j\neq i}\ m_{j\to i}\, A_{corr}(j \to i)}{m_{i\to i}} \tag{4.52}$$

The variable $A_{\pi^0\,corr}(i)$ has already been computed: the results from figure 4.19 are used, to include the π^0 contamination subtraction. $A_{corr}(j \to i)$ cannot be directly measured from the data since it is not possible to isolate among the events reconstructed in bin i, the ones that are coming from the bin j. Since these events are mainly coming from the edge of the bins, a first order approximation, which should be valid for directly neighboring bins, is given by taking the averaged asymmetry between the bin i and the bin j:

$$A_{corr}(j \to i) \simeq \frac{A_{\pi^0\,corr}(i) + A_{\pi^0\,corr}(j)}{2} \tag{4.53}$$

Finally, the migration fractions are given by the migration matrix obtained by a DVCS Monte-Carlo simulation, defined in section 4.7.1:

$$m_{j\to i} = \frac{M_{j\to i}}{\sum_{bin\ k} M_{k\to i}} \tag{4.54}$$

Note that the use of a DVCS simulation without π^0 contamination is consistent with the use of the beam-spin asymmetries $A_{\pi^0\,corr}(i)$, after correction for the π^0 contamination.

The BSA $A_{LU,\,corr}(i)$, after application of the bin migration correction (and including the π^0 contamination correction), is shown on figure 4.21. Only the statistical uncertainty $\Delta^{stat}_{LU,\pi^0\,corr}$ is shown here, as defined in section 4.8.1. Overall the impact of the bin migration correction is small, smaller than the impact of the π^0 contamination correction, the change is well below 1% (absolute change) for most of the bins and up to a few percent for a few bins.

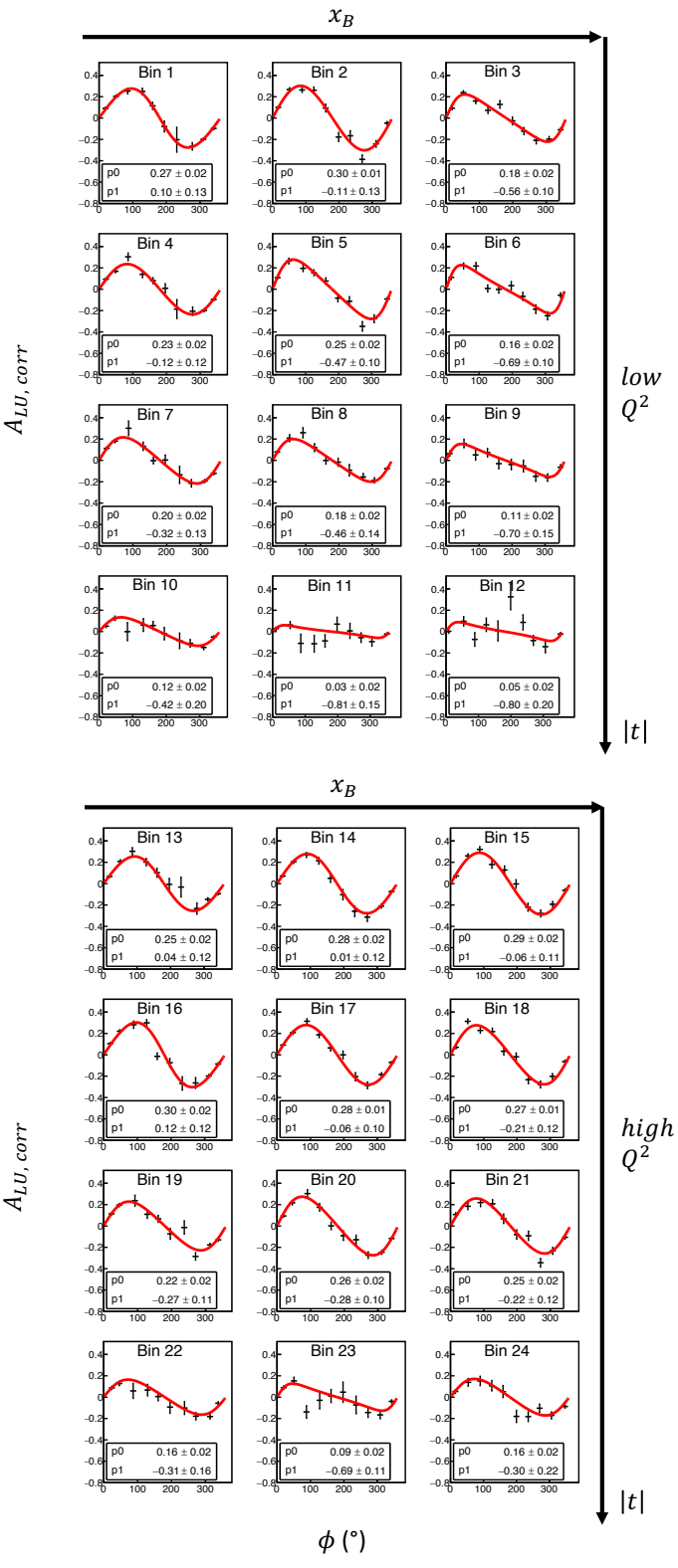

Figure 4.21: DVCS beam-spin asymmetry $A_{LU,\,corr}(i)$ corrected for π^0 contamination and bin migration, as a function of ϕ for each (Q^2, x_B, t) bin. The fit function 4.40 is used. Only the statistical uncertainty $\Delta^{stat}_{LU,\pi^0\,corr}$ is considered here, following the definitions from section 4.8.1.

4.8 Evaluation of uncertainties

4.8.1 Statistical uncertainties

Raw statistical uncertainties

The beam-spin asymmetry statistical uncertainties are computed by propagation of uncertainties from equation 4.39. The uncertainties associated with the beam polarization are considered as purely systematic uncertainties (see details in section 4.8.2). The statistical uncertainty for a given bin i is therefore:

$$\Delta A^{stat}_{LU,\,raw}(i) = \frac{2}{P}\,\frac{\sqrt{\left[N^{-}_{raw}(i)\;\Delta N^{+}_{raw}(i)\right]^2 + \left[N^{+}_{raw}(i)\;\Delta N^{-}_{raw}(i)\right]^2}}{\left[N^{+}_{raw}(i) + N^{-}_{raw}(i)\right]^2} \tag{4.55}$$

with

$$\Delta N^{\pm}_{raw}(i) = \frac{1}{C^{\pm}}\sqrt{n^{\pm}_{ep\gamma,\,id}(i)} \tag{4.56}$$

Statistical uncertainties after the π^0 correction

To propagate the statistical uncertainties with the π^0 contamination correction, the same equation 4.57 is used but with a number of events corrected for the π^0 contamination.

$$\Delta A^{stat}_{LU,\,\pi^0\,corr}(i) = \frac{2}{P}\,\frac{\sqrt{\left[N^{-}_{\pi^0\,corr}(i)\;\Delta N^{+}_{\pi^0\,corr}(i)\right]^2 + \left[N^{+}_{\pi^0\,corr}(i)\;\Delta N^{-}_{\pi^0\,corr}(i)\right]^2}}{\left[N^{+}_{\pi^0\,corr}(i) + N^{-}_{\pi^0\,corr}(i)\right]^2} \tag{4.57}$$

In this case:

$$\begin{aligned} N^{\pm}_{\pi^0\,corr}(i) &= \frac{1}{C^{\pm}}\left[n^{\pm}_{ep\gamma,\,id}(i) - n^{\pm}_{\pi^0,\,cont}(i)\right] \\ &= \frac{1}{C^{\pm}}\left[n^{\pm}_{ep\gamma,\,id}(i) - r(i)\;n^{\pm}_{\pi^0,\,id}(i)\right] \end{aligned} \tag{4.58}$$

with $r(i)$ defined in section 4.6.2 and therefore, after propagation of the statistical uncertainty from $n^{\pm}_{ep\gamma,\,id}(i)$, $r(i)$ and $n^{\pm}_{\pi^0,\,id}(i)$:

$$\Delta N^{\pm}(i) = \frac{1}{C^{\pm}}\left[\sqrt{n^{\pm}_{ep\gamma,\,id}(i) + r(i)^2\;n^{\pm}_{\pi^0,\,id}(i) + \left[n^{\pm}_{\pi^0,\,id}(i)\;\Delta r(i)\right]^2}\right] \tag{4.59}$$

with

$$\Delta r(i) = \sqrt{\frac{r(i) + r(i)^2}{n^{simu}_{\pi^0,\,id}(i)}} \tag{4.60}$$

Comparison of statistical uncertainties

A comparison of the statistical uncertainties for the raw BSA and after the π^0 contamination correction is shown on figure 4.22. The raw statistical uncertainty is roughly between 1 and 5%, with the minimum for $\phi \simeq 0^\circ$ and the maximum around $\phi \simeq 180^\circ$. Overall, the impact of the π^0 contamination corrections is relatively limited (less than 1% for most of the bins) compared to the statistical uncertainties initially obtained from the raw BSA. However, as expected from the π^0 contamination fractions, in the high x_B and high $|t|$ region, the statistical uncertainty increases significantly after the π^0 contamination correction (roughly 1 to 5% more than the initial uncertainty).

4.8.2 Systematic uncertainties

Systematic uncertainty associated with the beam polarization

In this analysis, the uncertainties associated with the polarization are considered as systematic uncertainties since they do not depend on the amount of physics data analysed.

The value of the polarization, provided by polarization measurements as explained in section 2.2.1, is $P = 0.863$ with an uncertainty $\Delta P = 0.037$, which is the sum of the statistical uncertainty and the estimated systematic uncertainty on the polarization measurement (given by the calibration uncertainty of the Møller polarimeter). The measurement of the polarization and the estimation of its uncertainty was not part of the work done for this thesis. The propagation of the polarization uncertainty to the beam-spin asymmetry is:

$$\Delta A_{LU\ corr}^{syst\ P}(i) = \frac{A_{LU\ corr}}{P}\Delta P \tag{4.61}$$

Systematic uncertainty associated with the π^0 background

The π^0 contamination estimation is based on the assumption that the ratio r is the same in the simulation and in data. However, it is possible that this assumption is inexact, a systematic uncertainty is therefore associated with the π^0 contamination correction. This systematic uncertainty takes into account, in particular, the following sources of uncertainties:

- uncertainties associated with the selection of DVCS and π^0 exclusive events (selection detailed in section 4.4 and 4.6.1). Since r is related to the size of the phase space for decays identified as π^0 and decays identified as DVCS events, the selection of DVCS and π^0 has to be consistent in the simulation and in data. This effect is, at the first order, taken into account by using the resolutions to adjust the exclusivity cuts in the data with respect to the simulation (see section 4.4.3) but this systematic uncertainty accounts for the potential imprecisions of this method.

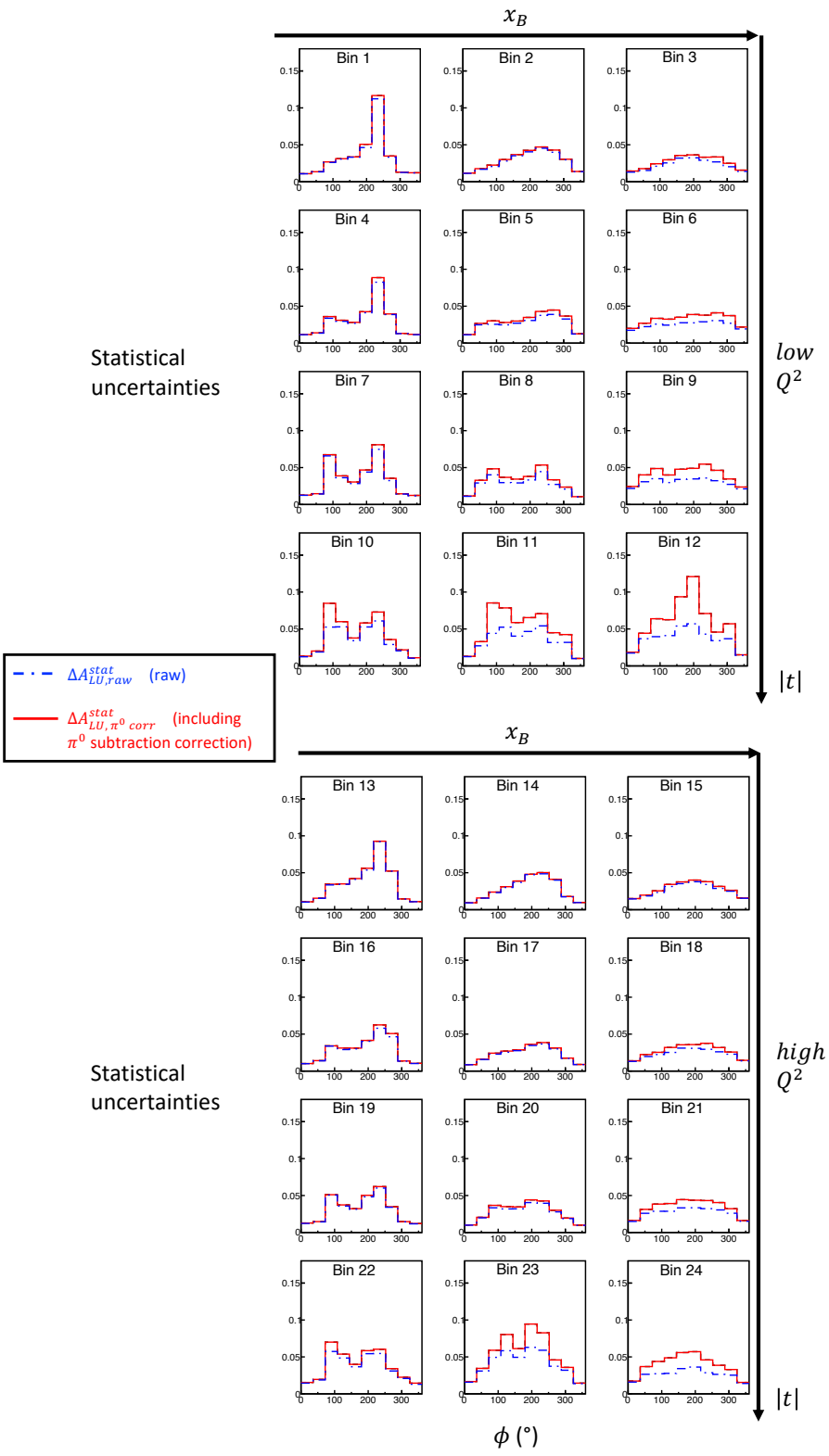

Figure 4.22: BSA statistical uncertainties. In blue with dot-dashed lines, $\Delta A^{stat}_{LU,\,raw}$ without applying any correction. In red with continuous line, $\Delta A^{stat}_{LU,\,\pi^0\,corr}$ after applying the π^0 contamination correction.

- uncertainties associated with the inaccuracies of the simulation. This account for the fact that the simulation may not accurately reproduce experimental data, for instance if inefficiencies of the detectors are not simulated properly.

A systematic uncertainty is therefore associated with the contamination fraction to account for these limitations. In a (Q^2, x_B, t, ϕ) bin i, the contamination fraction, noted $f(i)$, is defined as the amount of π^0 contamination $n_{\pi^0,\,cont}(i)$ divided by the total number of events identified as DVCS $n_{ep\gamma,\,id}(i)$:

$$f(i) = \frac{n_{\pi^0,\,cont}(i)}{n_{ep\gamma,\,id}(i)} \tag{4.62}$$

The raw BSA measured can then be decomposed into a contribution that arises from π^0 contamination events $A_{LU,\,\pi^0,\,cont}(i)$ and the contribution from "real" DVCS events $A_{LU,\,\pi^0\,corr}(i)$, corrected for π^0 subtraction:

$$A_{LU,\,raw}(i) = \left[1 - f(i)\right] A_{LU,\,\pi^0\,corr}(i) + f(i)\, A_{LU,\,\pi^0,\,cont}(i) \tag{4.63}$$

which can be re-written:

$$A_{LU,\,\pi^0\,corr}(i) = \frac{A_{LU,\,raw}(i) - f(i)\, A_{LU,\,\pi^0,\,cont}(i)}{1 - f(i)} \tag{4.64}$$

An error on the contamination fraction $\Delta f(i)$ propagates to the DVCS BSA as follows:

$$\Delta A^{syst\ \pi^0}_{LU,\,\pi^0\,corr}(i) = \frac{A_{LU,\,raw}(i) - f(i)\, A_{LU,\,\pi^0\,cont}}{\left[1 - f(i)\right]^2} \Delta f(i) \tag{4.65}$$

A relative uncertainty on the contamination fraction of 30% is used in this analysis, for all kinematic bins: $\Delta f(i) = 0.3\ f(i)$. The BSA coming from π^0 contamination events $A_{LU,\,\pi^0\,cont}$ is estimated from the BSA of $n_{\pi^0,\,id}(i)$,the π^0 events selected by the π^0 selection cuts.

Uncertainties associated with the binning

A systematic is finally associated with the bin migration correction. This accounts, in particular, for the following effects:

- shifts in the reconstruction of the kinematic variables. This can come, for instance, from geometry shifts in the simulation, or if the magnet position is not well known.

- radiative Bremsstrahlung effects that are not simulated. As mentionned in section 4.7.1, the bin migration correction takes into account the external Bremsstrahlung since this effect is included in the simulation. This systematic uncertainty considers the internal radiative effects which are not simulated.

- approximation of $A_{LU,\,corr}(j \to i)$ made to estimate the bin migration correction (see section 4.52.

Systematic uncertainties are therefore associated, in equation 4.52 to $A_{LU,\,corr}(j \to i)$ and $m_{j\to i}$ and are propagated as follows (we omit the subscript "LU"'):

$$\Delta A^{\textit{syst bin migration}}_{\textit{LU corr:}}(i) = \sqrt{\sum_{j\neq i}\left[\left(\frac{-m_{i\to i}A_{corr}(j\to i) + A_{\pi^0\,corr}(i) - \sum_{j\neq i} m_{j\to i}A_{corr}(j\to i)}{m^2_{i\to i}}\Delta m_{j\to i}\right)^2 + \left(\frac{-m_{j\to i}}{m_{i\to i}}\Delta A_{corr}(j\to i)\right)^2\right]}$$

A 10% relative uncertainty is associated with $\Delta m_{j\to i}$ and an uncertainty equal to half of the difference between $A_{LU,\,\pi^0\,corr}(i)$ and $A_{LU,\,\pi^0\,corr}(j)$ is associated with $\Delta A_{corr}(j\to i)$:

$$\begin{aligned} \Delta m_{j\to i} &= 0.1\; m_{j\to i} \\ \Delta A_{LU,\,corr}(j\to i) &= \frac{|A_{LU,\,\pi^0\,corr}(i) - A_{LU,\,\pi^0\,corr}(j)|}{2} \end{aligned} \tag{4.66}$$

Comparison of systematic uncertainties

The systematic uncertainties from the polarisation, the π^0 contamination correction and the bin migration correction are shown on figure 4.23, compared with statistical uncertainty.

Overall, the statistical uncertainties dominate the systematic uncertainties. The systematic uncertainty associated with the beam polarisation is estimated between 0.1 and 2% (absolute uncertainties on the BSA, see table 4.5) and is small compared to the statistical uncertainty. The systematic uncertainty from the bin migration can reach 1 to 2% in some of the bins, however, overall, it is the smallest source of systematic uncertainty and it is very small compared to the statistical uncertainty. As expected, the systematic associated with the π^0 contamination correction is almost negligible (well below 1%) in low x_B and low $|t|$ bins. However, in the high x_B and high t region, this systematic becomes significant and sometimes comparable to the statistical uncertainty (roughly 1 to 7 %).

Uncertainties	Range
Statistical uncertainty	$\simeq$ 1 to 10 %
Polarisation systematic uncertainty	$\simeq$ 0.1 to 2 %
Bin migration systematic uncertainty	$\simeq$ 0.1 to 2 %
π^0 contamination systematic uncertainty	$\simeq$ 0.1 to 7 %

Table 4.5: List of uncertainties and their approximate range of variation (absolute uncertainties on the BSA)

4.9 Final beam-spin asymmetry results

The final results for the beam-spin asymmetry extraction are presented on figure 4.24. They include the statistical and all the systematic uncertainties described in section 4.8, assumed to be independent and summed quadratically.

$$\Delta A_{LU\ corr} = \sqrt{\left(\Delta A^{stat}_{LU,\pi^0\ corr}\right)^2 + \left(\Delta A^{syst\ P}_{LU\ corr}\right)^2 + \left(\Delta A^{syst\ \pi^0}_{LU\ corr}\right)^2 + \left(\Delta A^{syst\ bin\ migration}_{LU\ corr}\right)^2} \quad (4.67)$$

The fit function 4.40 is used and the dependences of the amplitude p_0 are summarized on figure 4.25. The amplitude of the BSA varies with t, decreasing as $|t|$ increases. A higher amplitude is obtained for the high Q^2 bins compared to the low Q^2 bins. No overall x_B dependence is found: the x_B dependence in the raw BSA, discussed in section 4.5, is largely removed by the π^0 contamination correction. Note however, that this comparison does not show the average x_B and Q^2, which are different for each point. The fit parameters, fit parameters uncertainties and average kinematic variables for each bins are presented in table A.1.

4.10 Conclusion

In this analysis, the photon electroproduction beam-spin asymmetry has been extracted over a large kinematic range. The effects of π^0 electroproduction contamination and bin migration have been corrected. Overall the statistical uncertainty dominates, but the systematic uncertainty associated with the π^0 contamination becomes comparable to the statistical uncertainty in the high x_B and high $|t|$ region. The results are fitted with a fit function based on the expected first order coefficients, which, overall, describes the distributions well. The decrease of the beam-spin asymmetry amplitude with $|t|$ is highlighted, as expected from previous DVCS results (for instance [42]).

To refine this analysis, the emphasis should be put on the π^0 contamination correction. A better understanding of the photon reconstruction in the data and the simulation, as well as a comparison of the π^0 contamination results obtained with other methods could help improve the precision of the π^0 contamination subtraction.

In addition to the refinement of the analysis itself, further improvements of the reconstruction and calibration procedures are expected before the final results are published.

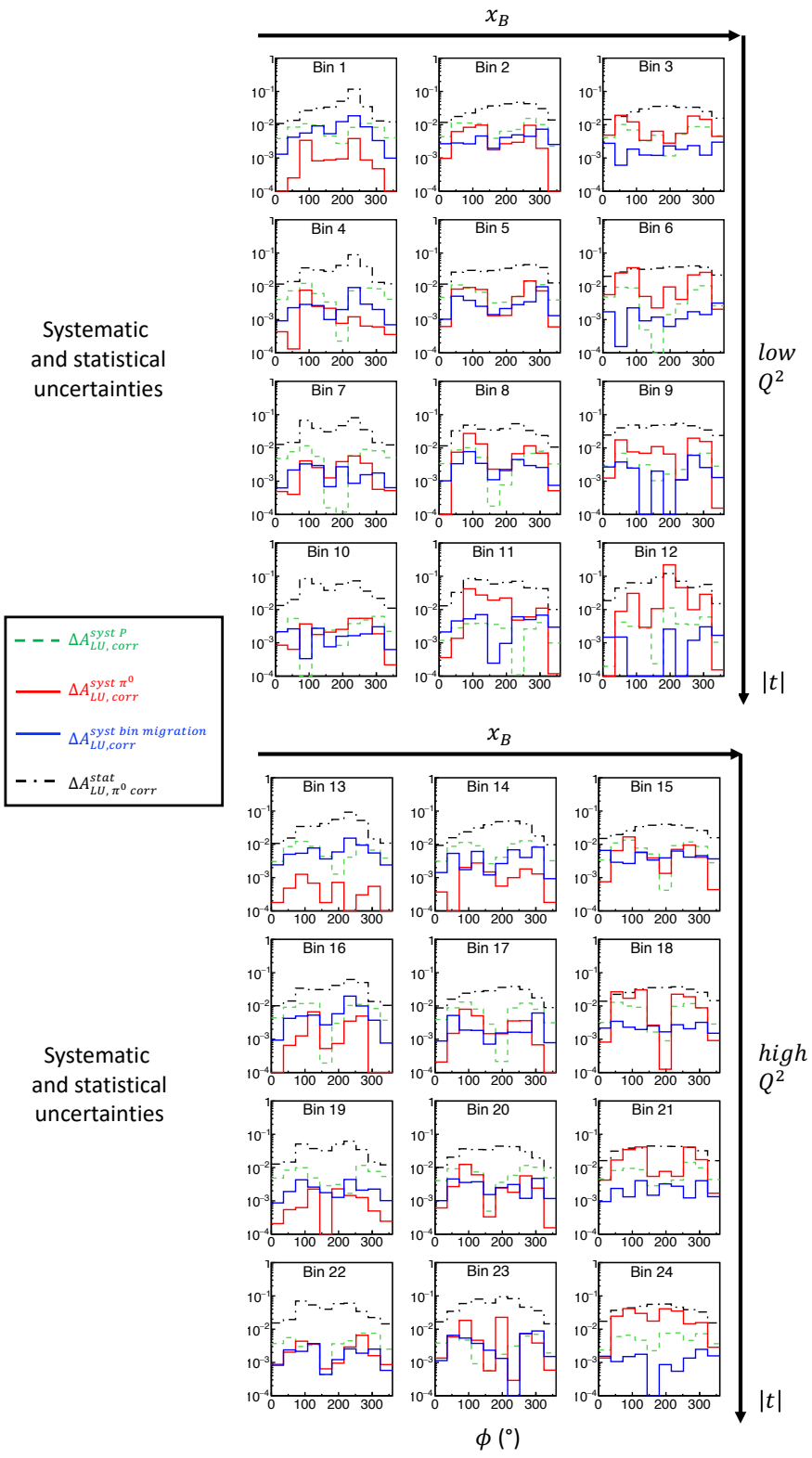

Figure 4.23: BSA systematic and statistical uncertainties. In green with dashed lines, $\Delta A_{LU,\,corr}^{syst\ P}$ the beam polarisation systematic uncertainty. In blue with continuous line, $\Delta A_{LU,\,corr}^{syst\ bin\ migration}$ the bin migration systematic uncertainty . In red with continuous line, $\Delta A_{LU,\,corr}^{syst\ \pi^0}$ the π^0 contamination systematic uncertainty. In black with dot-dashed line, $\Delta A_{LU,\,\pi^0\,corr}^{stat}$ the total statistical uncertainty (including the π^0 contamination and bin migration corrections)

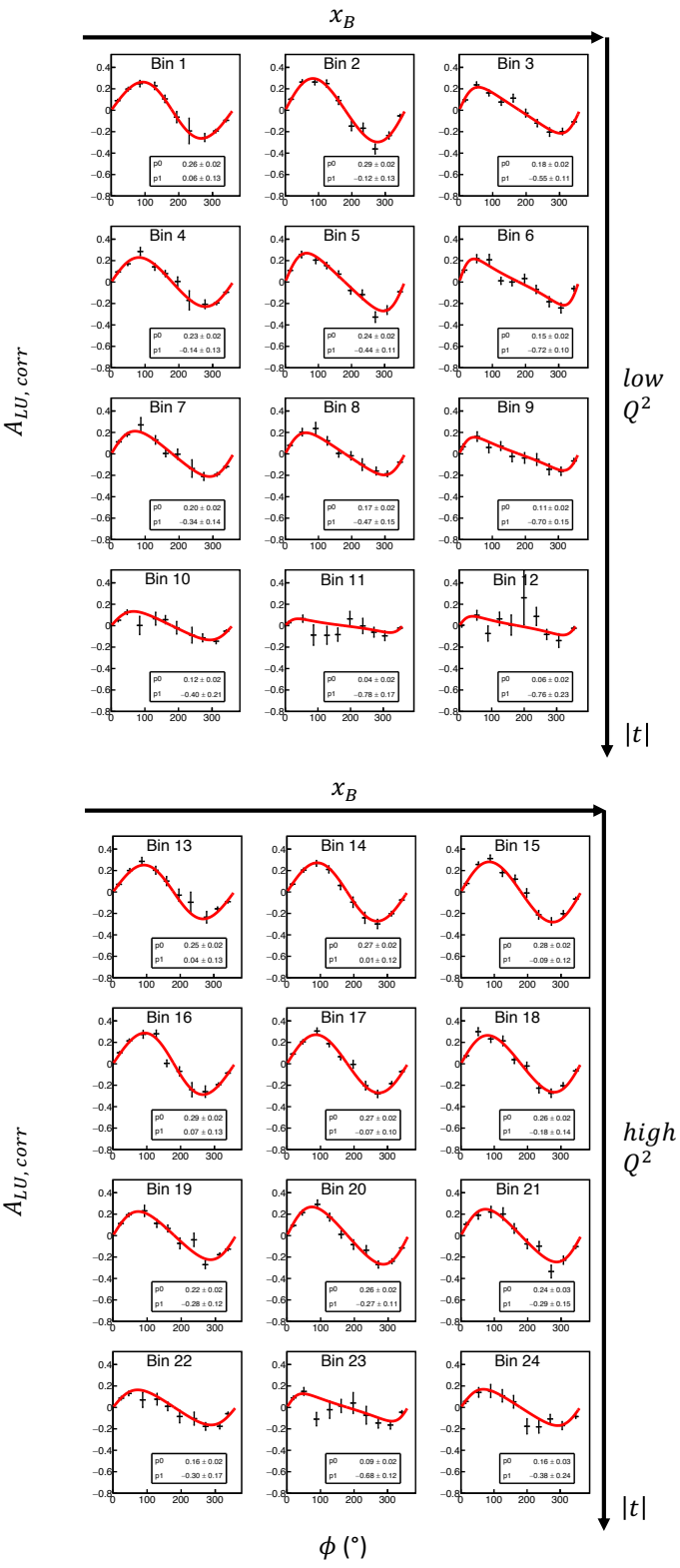

Figure 4.24: Final DVCS beam-spin asymmetries, corrected for π^0 contamination and bin migration, as a function of ϕ for each (Q^2, x_B, t) bin. The uncertainty $\Delta A_{LU\,corr}$ includes the statistial and all the systematic uncertanties. The fit function 4.40 is used.

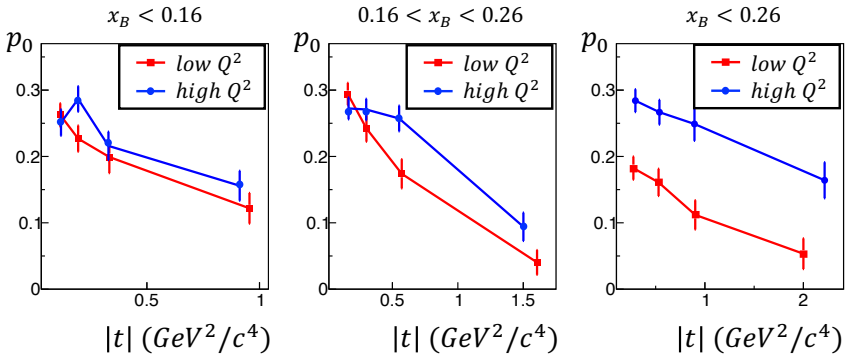

Figure 4.25: Amplitude of the BSA fit p_0 as a function of $|t|$ for each (Q^2, x_B, t) kinematic bin.

Conclusion

In this thesis, the DVCS reaction off the proton was analysed and the beam-spin asymmetry observable was extracted from 10.6 GeV electron beam data taken with the CLAS12 spectrometer at Jefferson Laboratory and an unpolarized liquid hydrogen target.

Micromegas detectors were successfully installed to improve the tracking resolutions in the central region of CLAS12. The Micromegas detectors have been systematically tested with cosmic rays at CEA Saclay before shipment to Jefferson Lab. The MVT was assembled in summer 2017 and integrated with the silicon vertex tracker shortly after. After the integration of the gas system and software, the CVT took a large amount of cosmic ray data. The CVT was mounted within the CLAS12 spectrometer at the end of 2017. After commissioning with electron beam data, CLAS12 Micromegas detectors took their first physics data in spring 2018.

The DVCS beam-spin asymmetry was extracted from the data taken by the CLAS12 spectrometer. A pre-selection method was developed to carry out an initial selection of data. The exclusivity of the measurement was used to select the DVCS signal. This selection was optimised to provide the most efficient selection of DVCS signal while removing background. The emphasis was made to provide an estimation of the background contamination from π^0 electroproduction and a correction of this contamination was applied. A Monte-Carlo generator was implemented to provide a simulation of combined photon and π^0 electroproduction events. The beam-spin asymmetry results are given over a large kinematic range, binned in 24 (Q^2, x_B, t) bins with 10 ϕ bins each. A bin migration correction was included. Statistical uncertainties were computed and main sources of systematic uncertainties were estimated.

This analysis provides DVCS BSA measurements in an unprecedented kinematic domain. Overall the uncertainties are dominated by statistics but the systematic uncertainty associated with the π^0 electroproduction contamination becomes comparable to the statistical uncertainty for some of the high-x_B bins. Roughly 12% of the data that will be collected by CLAS12 on unpolarized proton target is presented in this thesis. The binning used in this analysis could therefore be refined to provide more data points, in particular in the high Q^2 region which could not be explored by previous experiments.

To expand this work, it would be interesting to study with more details the choice of binning and to refine the π^0 electroproduction background and the estimation of the uncertainties. The main difficulty with this analysis is the subtraction of the π^0 electroproduction background, a

second method to estimate this background, based on the use of π^0 electroproduction events detected in data as a π^0 generator for the simulation, is currently being studied. A better understanding of the reconstruction of photons in data and in the simulation is also needed to reduce the uncertainty associated with the π^0 correction.

This analysis was performed in parallel with another approach that uses machine learning algorithms at different stages of the analysis [80] [81]. The comparison of the results obtained from the two methods will provide insights on the improvements than can be made to this analysis.

The BSA results from this analysis, associated with the analysis of other observables as well as previous and future results (such as the future Electron-Ion Collider) will provide a very large set of points that can be used to extract the contribution of the different CFFs. Phenomenological frameworks have already been developed [82] to perform these fits, including higher-order effects that become necessary to reproduce the measurements. The extraction of GPDs and the construction of GPD models from these constraints is a very complex problem. The involvement of both experimentalists and phenomenologists is therefore needed to provide a better understanding of nucleon structure.

Appendix A

A.1 General notations and conventions

In this document, the following notations are used:

- four-vectors are noted as: $x(x^t, x^x, x^y, x^z) = x(x^t, \vec{x})$ with x^t the time coordinate and $\vec{x}(x^x, x^y, x^z)$ the Euclidian part
- the Minkovsky tensor is defined in such a way that the associated 4x4 matrix is:

$$\eta = \begin{pmatrix} 1 & 0 & 0 & 0 \\ 0 & -1 & 0 & 0 \\ 0 & 0 & -1 & 0 \\ 0 & 0 & 0 & -1 \end{pmatrix} \tag{A.1}$$

  the product of two four-vectors x and y is therefore defined as:

$$xy = x^t y^t - x^x y^x - x^y y^y - x^z y^z \tag{A.2}$$

- Dirac matrices are noted as γ^0, γ^1, γ^2 and γ^3. The tensor $\sigma^{\mu,\nu}$ is defined from Dirac matrices as follows:

$$\sigma^{\mu\nu} = \frac{i}{2}(\gamma^\mu \gamma^\nu - \gamma^\nu \gamma^\mu) \tag{A.3}$$

  The matrix γ^5 is defined as the product of Dirac matrices:

$$\gamma^5 = i\gamma^0\gamma^1\gamma^2\gamma^3 \tag{A.4}$$

- for a given four-vector $x = (x^t, x^x, x^y, x^z)$, the light-cone notation for this four-vector is

$x = (x^+, x^x, x^y, x^-)$ with x^+ and x^- defined as:

$$\begin{aligned} x^+ &= \frac{x^t + x^z}{\sqrt{2}} \\ x^- &= \frac{x^t - x^z}{\sqrt{2}} \end{aligned} \tag{A.5}$$

The transverse vector $\vec{x}_\perp$ is formed of the remaining coordinates x^x and x^y.

- the delta function δ is defined with the usual convention:

$$\begin{aligned} \delta(x) &= \begin{cases} 0 & \text{if } x \neq 0 \\ \infty & \text{if } x = 0 \end{cases} \\ \int_{-\infty}^{\infty} dx\, \delta(x) &= 1 \end{aligned} \tag{A.6}$$

A.2 Coordinate system

The notations used to describe particles are defined in figure A.1. Note in particular that the z-axis is defined along the direction of the beamline and the angle θ is the angle between the particle and the z-axis (polar angle).

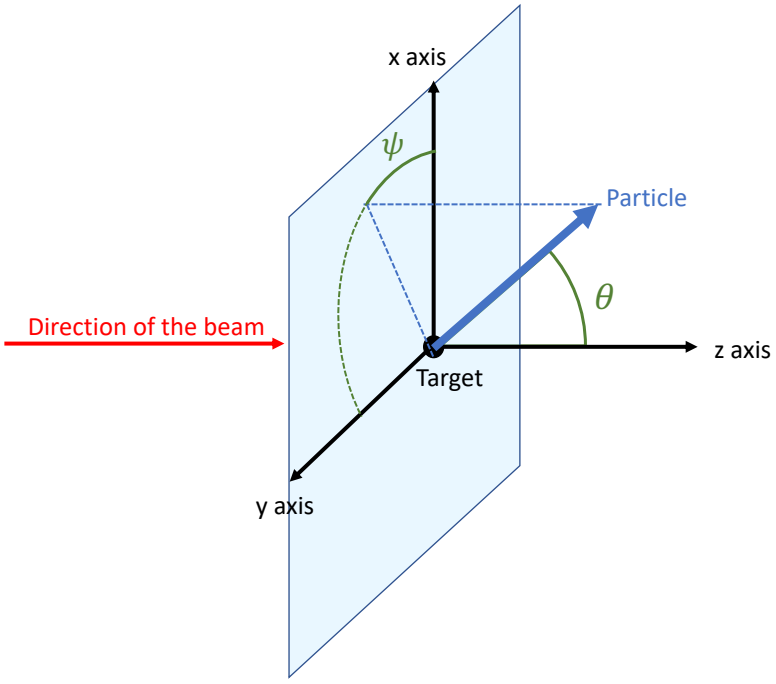

Figure A.1: Definition of the axis and angles used to describe the particles.

A.3 Some details about particle detection

A.3.1 Silicon detectors

Silicon detectors are semiconductor detectors using doped silicon, based on the detection of charge carriers created by ionization along the path of an incoming ionizing particle in the material. Silicon detectors are based on the interfacing of oppositely doped silicon materials, called p-n junctions: the p-side is doped to contain an excess of holes while the n-side is doped to contain an excess of electrons. These p-n junctions form a depletion zone between them, in which no mobile charge carriers are left. When voltage is applied to a p-n junction, an electric field is formed in the depletion region and the thickness of the depletion zone increases with the voltage applied (this sis used to turn almost the entire volume of silicon into depletion zone and maximize the active volume). When an incoming charged particle produces an ionization in the depletion region, electron-hole pairs are created (proportionally to the energy deposited in the material). The electrons and the hole drift because of the electric field and are collected creating a small ionization current.

Silicon detectors provide very good resolution, are very compact (since they have a high density compared, for instance, to gaseous detectors) and can sustain a high flux of particle (due to their fast charge collection). However they are very expensive and can suffer radiation degradation over time. They are generally used very close to the target to minimize the surface area.

A.3.2 Drift chambers

Drift chambers are gaseous trackers based on wire electrodes, they use the detection of ionization from incoming charged particles to reconstruct their trajectory (see figure A.2). Wires are arranged inside a chamber filled with a gas mixture (the choice of the gas is generally a tradeoff between gain, drift velocity and price). A potential difference is formed between the anode wires (sense wires) and cathode wires (field wires). Ionization in the gas from an incoming particle creates a electron-ion pair that drifts towards the wires. Once the electron reaches the vicinity of the sense wire, the electric field is such that an avalanche effect occur: electrons liberated by collision of the initial electron with molecules of the gas themselves acquire enough energy to create further impact ionizations, and so on. These electrons are collected by the wires, creating an electric current that can be measured. The time needed to collect the charges is directly related to the distance between the place where the ionization takes place and the wires. By combining the information collected by all the wires, the trajectory of the incoming particle can be reconstructed.

Drift chambers are generally relatively inexpensive compared to other modern tracking technologies and are often used when tracking is needed over a very large volume.

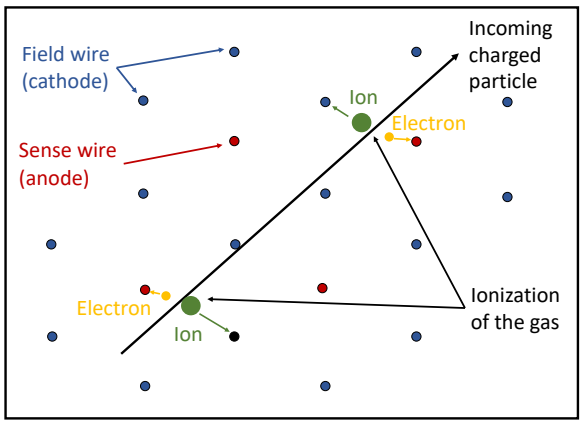

Figure A.2: Diagram of a drift chamber showing how electrons and ions are collected by the field and sense wires when the gas is ionized by an incoming charged particle. Wire are arranged with an hexagonal cell structure, each sense wire is surrounded by 6 field wires.

A.3.3 Scintilation detectors

Scintillation counters are detectors based on the association of a scintillator material and a light sensor (the most common being a photomultiplier tube).

Scintillators are transparent materials that are capable of scintillation: excitated atomic or molecular states are created by absorption of the energy deposited from an incoming particle followed by a rapid de-excitation in the form of light. Scintillators can be made of different types, for instance organic, plastic, inorganic, and have different physics processes responsible of scintillation (excitation of molecular or atomic states for instance).

A.3.4 Cherenkov detectors

A Cherenkov detector is based on the Cherenkov effect: light is emitted when a charged particle goes through a material at a velocity greater than the velocity of light in that same medium. Cherenkov detectors are based on the association of a material that can produce Cherenkov light and a light sensor (such as a photomultiplier tube).

The Cherenkov light produced by the Cherenkov effect is emitted in a cone centered on the particle direction (see figure A.3). The angle of the emission cone is directly related to the particle velocity. Threshold Cherenkov detectors generally use the presence or absence of Cherenkov radiation to separate light from heavy particles. Ring-imaging Cherenkov detectors (RICHs) directly measure the emission angle to access the particle velocity. Used in combination with a tracking system, Cherenkov detectors can be used to identify incoming particles.

A.3.5 Photomultiplier tubes

A photomultiplier tube (PMT) is a vacuum tube that can convert light to an electrical signal using a photocathode and several dynodes (see figure A.4). The photocathode is first used to create

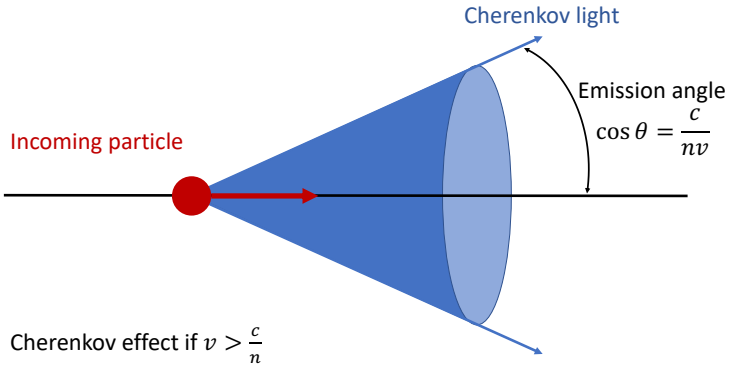

Figure A.3: Diagram of a the Cherenkov effect, n is the refractive index, c the speed of light in vacuum and v the velocity of the particle in the medium.

a small number of electrons from the incoming photons by photoelectric effect. Electrons are then multiplied by several electrodes, called dynodes, at an increasing electric potential which produce several electrons for each incoming electron and therefore amplify the signal.

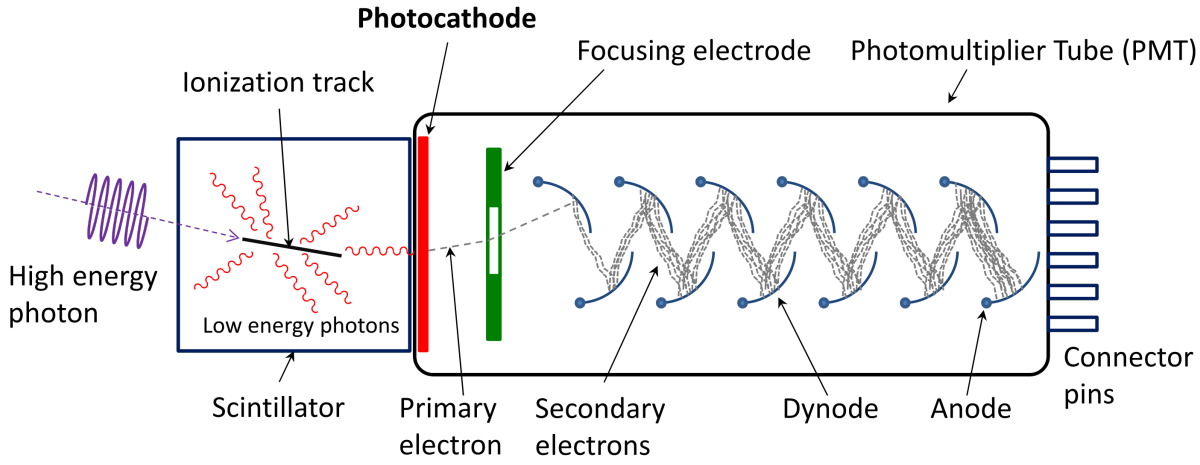

Figure A.4: Diagram of a scintillation counter, made of a photomultiplier tube attached to a scintillator [83].

A.3.6 Time-of-flight technique

A time-of-flight measurement is a measurement of the time taken by a particle to travel a known distance, giving information about its velocity. This measurement is done by measuring the time at two different positions on the particle trajectory. The measurement of velocity with the time-of-flight technique, when combined with the information on the particle momentum and charge provided by a tracking system, gives access to its mass and therefore identify the particle.

A.4 Detailed contributions to the Micromegas detectors

The main contributions from the author of this thesis, performed with the help of a CEA Saclay Micromegas team and Jefferson Lab staff, are described below:

- tests of all the Micromegas detectors with the cosmic ray test bench at CEA Saclay (see section 3.3.1)
- assembly and integration of the BMT and FMT with the SVT (section 3.2.1)
- integration of the gas system (see section 3.2.2).
- software integration of the Micromegas detectors (see section 3.2.3) and in particular: design of the slow controls and interlocks, implementation of the monitoring tools.
- cosmic ray commissioning of the Micromegas detectors with the SVT and the CTOF (section 3.3.2)
- commissioning and operation with the electron beam (see section 3.3.3), in particular, noise studies, synchronization of the detectors with the CLAS12 trigger, optimization of the voltages
- on-call expert for the Micromegas detector.

A.5 Additional analysis figures

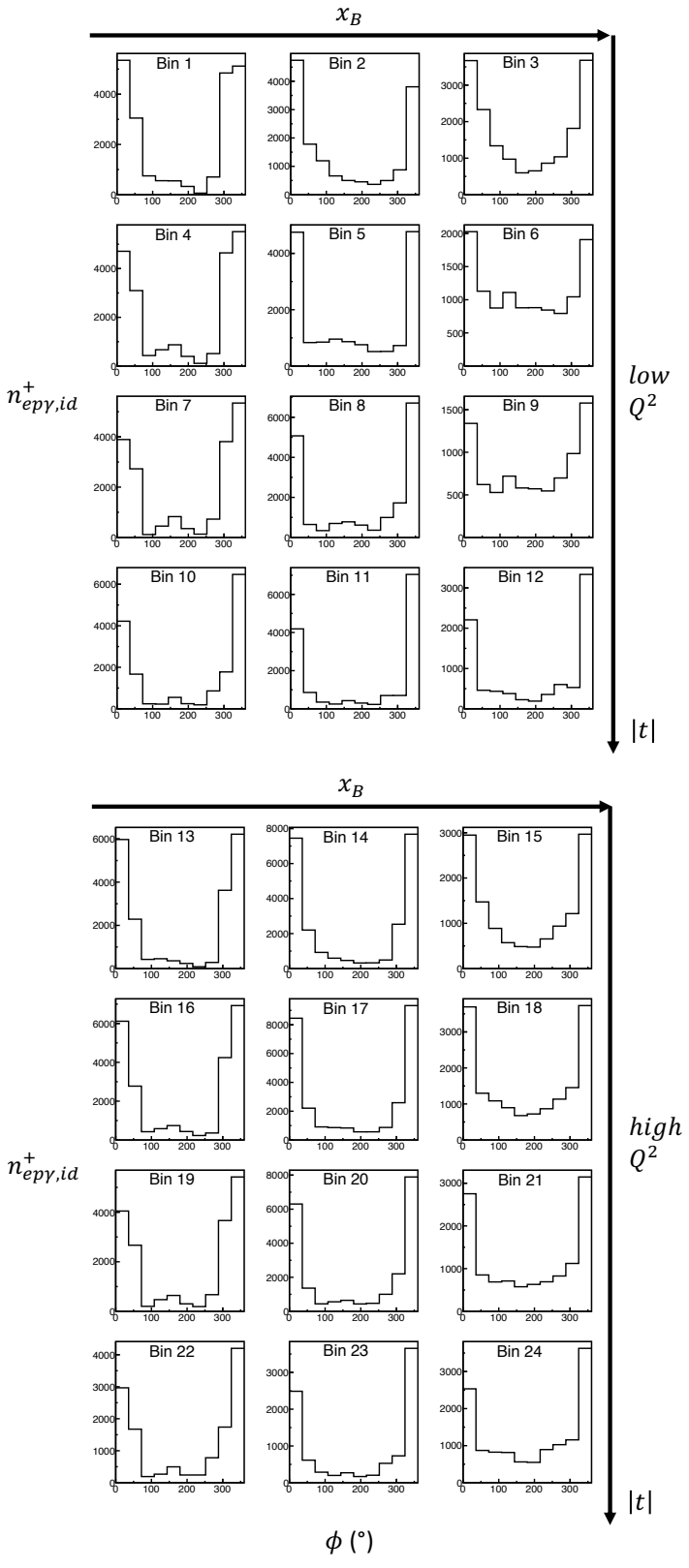

Figure A.5: Distribution of the number of events with positive helicities that pass all the DVCS selection cuts $n^+_{ep\gamma,\,id}(i)$, as a function of the angle ϕ, for all kinematic bins.

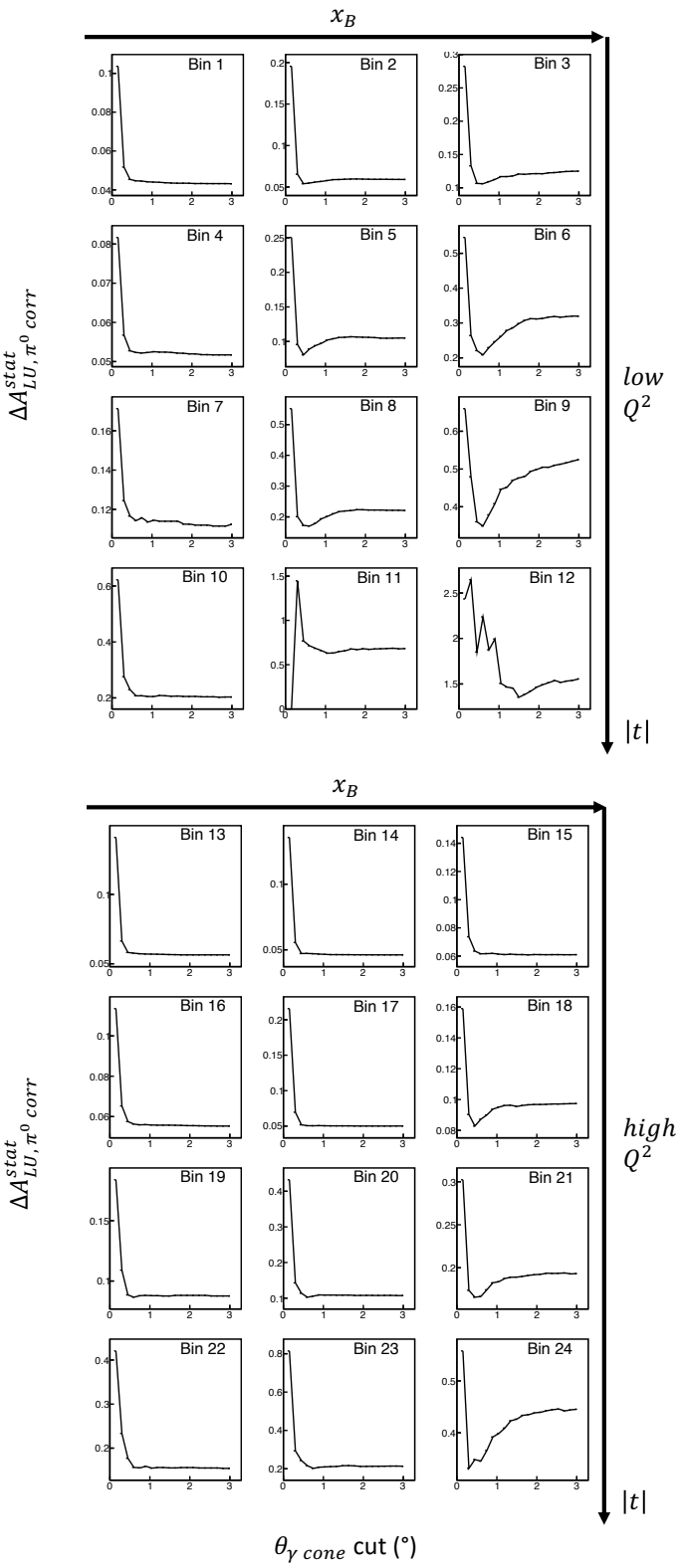

Figure A.6: Beam-spin asymmetry statistical uncertainty $\Delta^{stat}_{LU,\,\pi^0\,corr}$ around $\phi = 90^\circ$ as a function of the position of the photon cone angle cut for all the kinematic bins from simulation. Wide exclusivity cuts are used for all the other exclusivity variables.

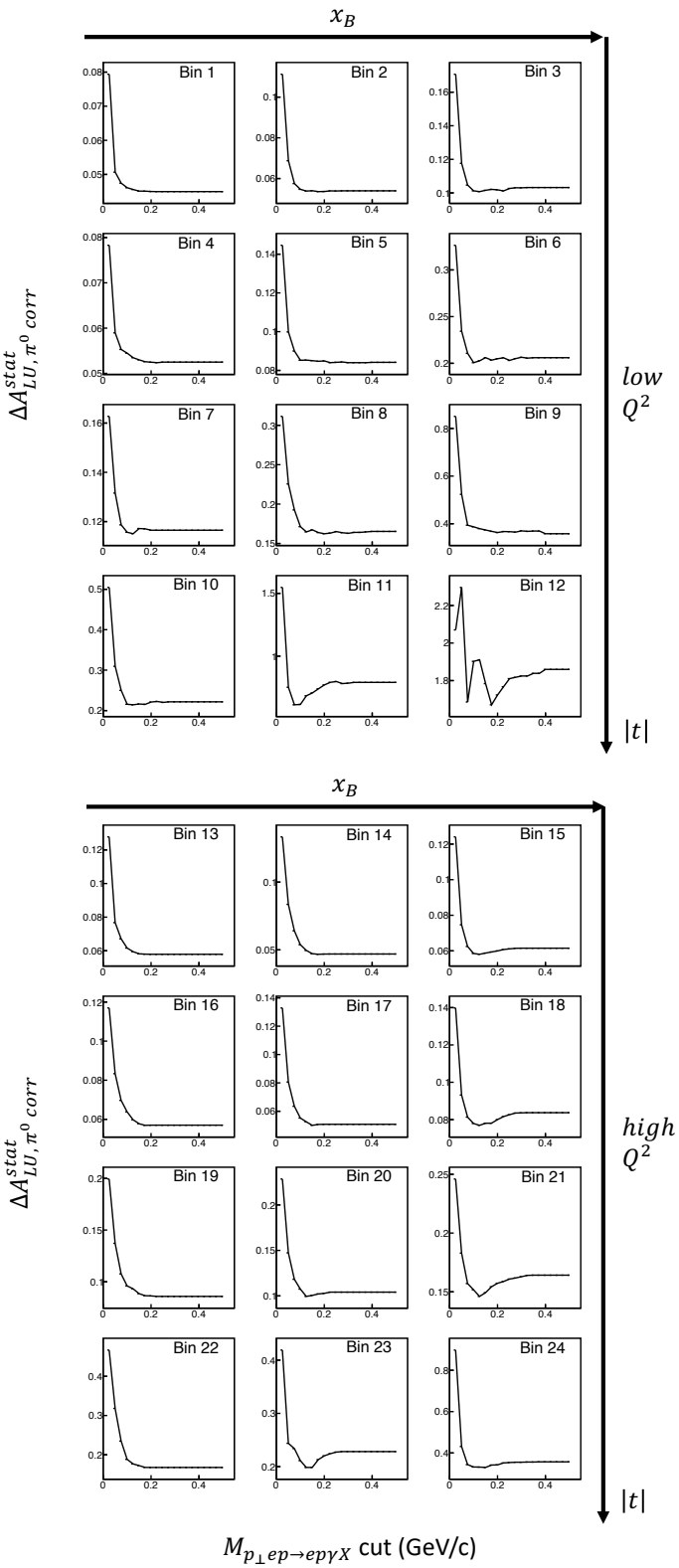

Figure A.7: Beam-spin asymmetry statistical uncertainty $\Delta^{stat}_{LU,\,\pi^0\,corr}$ at $\phi = 90^\circ$ as a function of the position of the missing transverse momentum in $ep \to ep\gamma X$ cut for all the kinematic bins. The photon cone angle cut position is optimised and wide exclusivity cuts are used on all the other exclusivity variables.

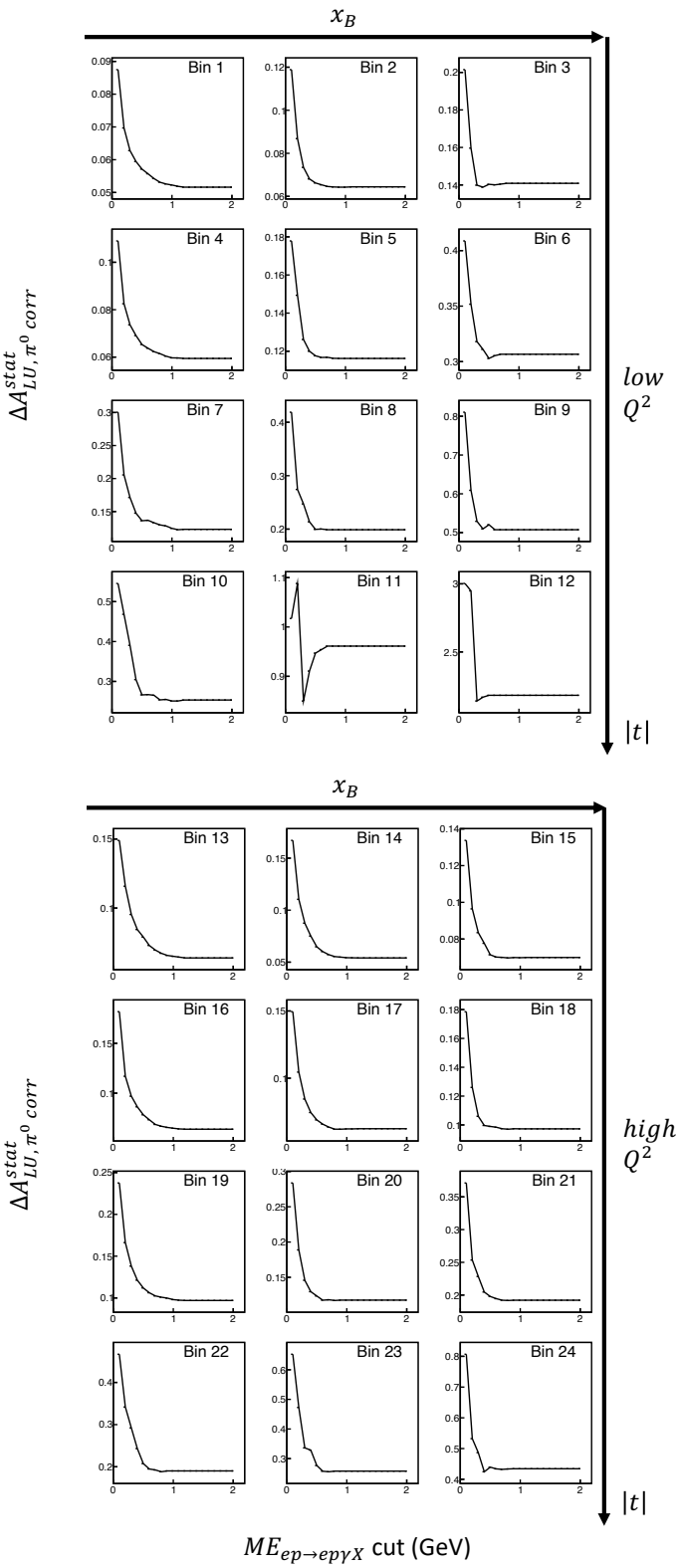

Figure A.8: Beam-spin asymmetry statistical uncertainty $\Delta^{stat}_{LU,\,\pi^0\,corr}$ around $\phi = 90^\circ$ as a function of the position of the missing energy in $ep \to ep\gamma X$ cut for all the kinematic bins from simulation. The photon cone angle and missing transverse momentum cut positions are optimised and wide exclusivity cuts are used on the other exclusivity variables.

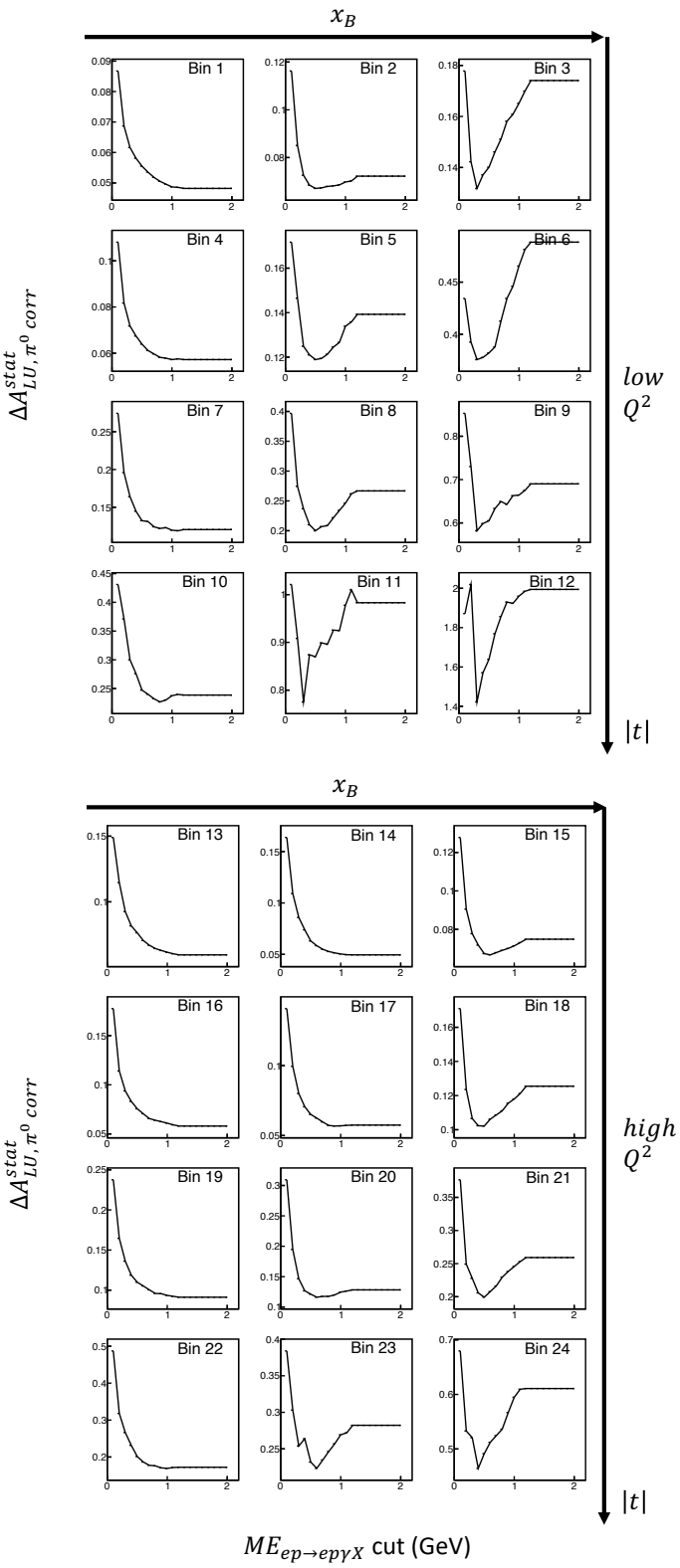

Figure A.9: Beam-spin asymmetry statistical uncertainty $\Delta^{stat}_{LU,\,\pi^0\,corr}$ around $\phi = 90^\circ$ as a function of the position of the missing energy in $ep \to ep\gamma X$ cut for all the kinematic bins from simulation. Wide exclusivity cuts are used for all the other exclusivity variables (without optimised values).

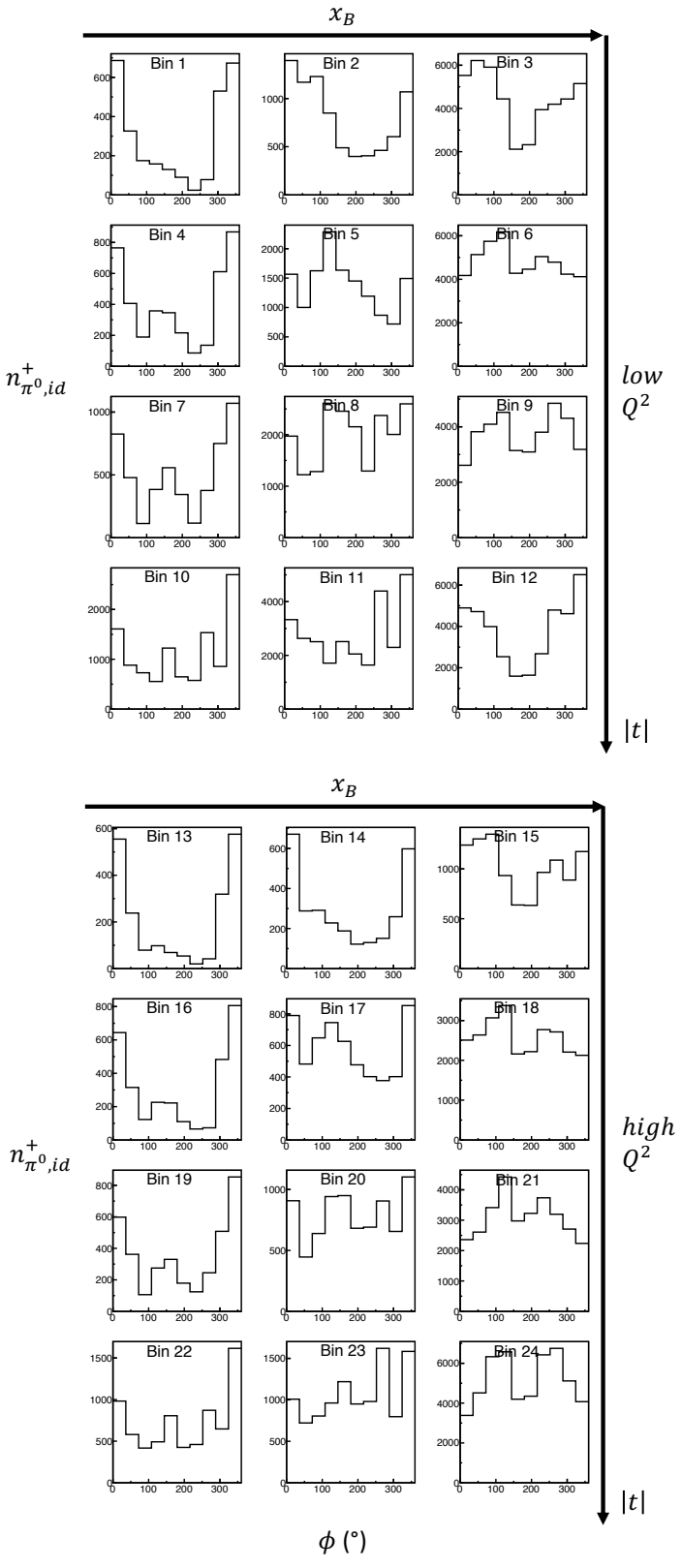

Figure A.10: Distribution of the number of events with positive helicities that pass all the π^0 selection cuts $n^+_{\pi^0,\,id}(i)$, as a function of the angle ϕ, for all kinematic bins.

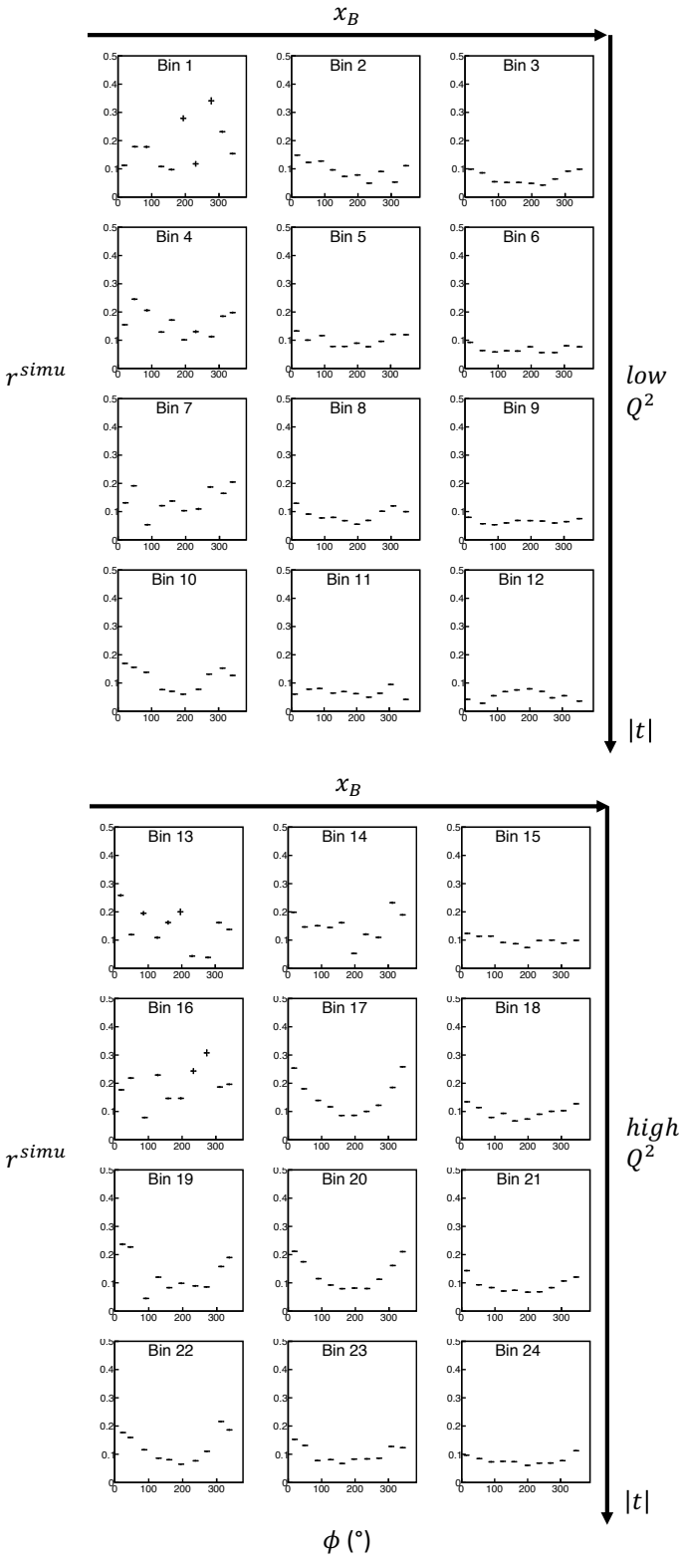

Figure A.11: Ratio r^{simu} of the contamination from π^0 events divided by the number of identified π^0 events, as a function of the angle ϕ, for all kinematic bins, with statistical uncertainties (defined in section 4.8.1).

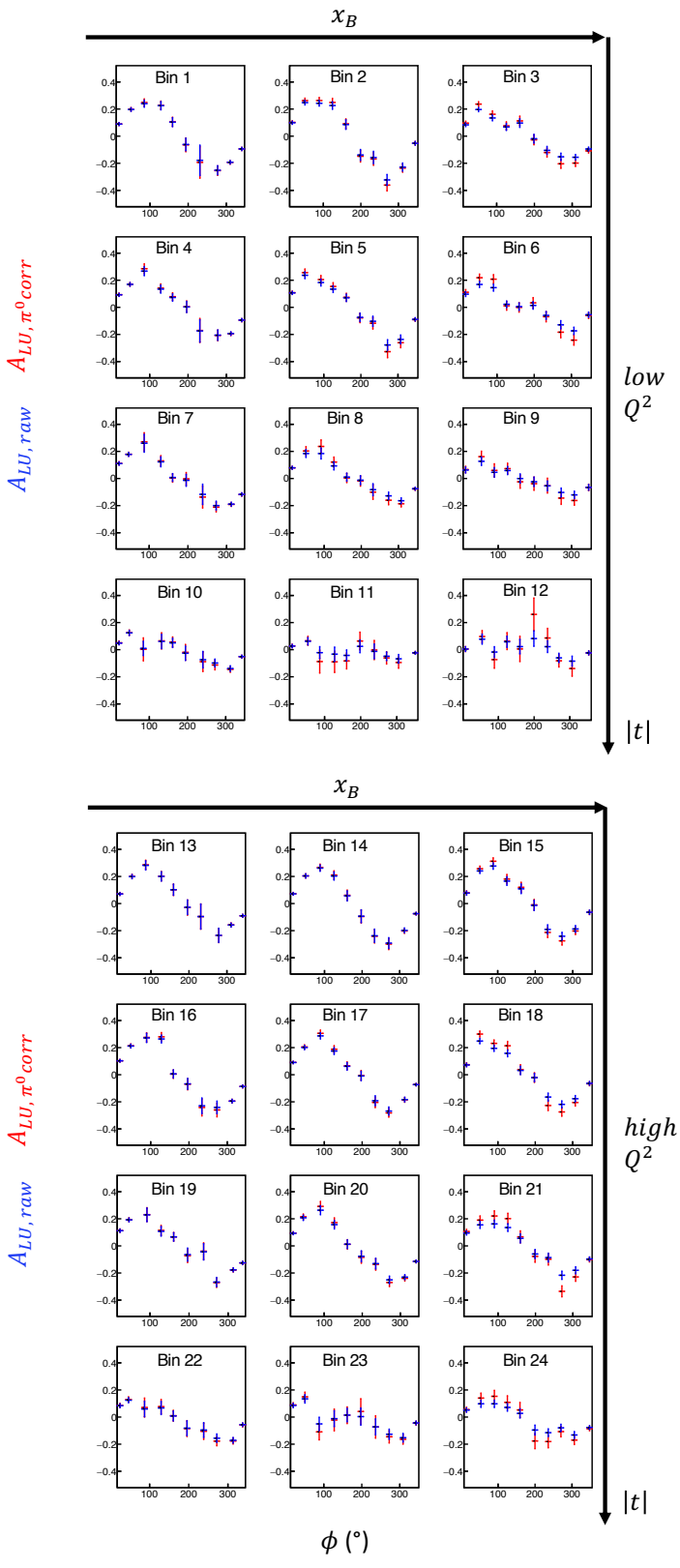

Figure A.12: Comparison of the raw BSA (in blue) and the BSA after π^0 contamination correction (in red) for all kinematic bins, with statistical uncertainties (defined in section 4.8.1).

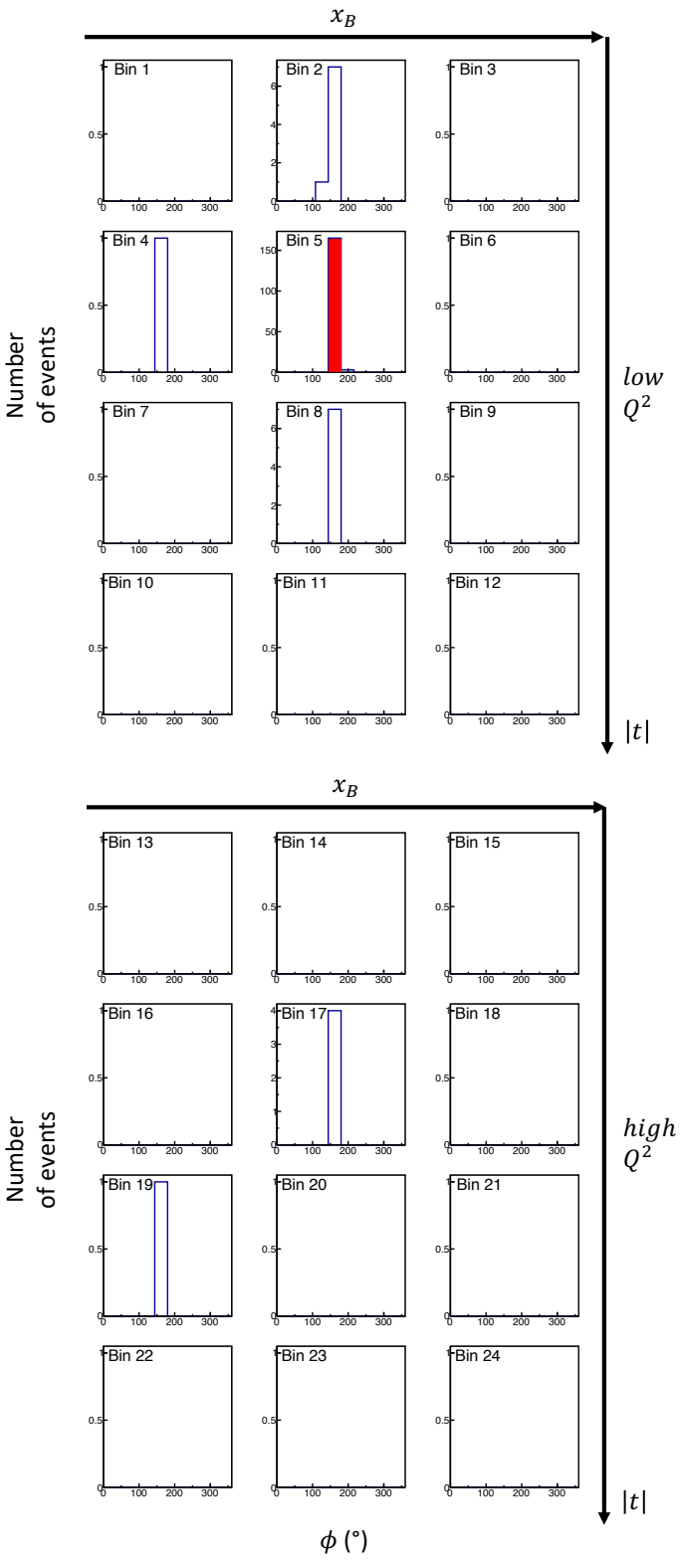

Figure A.13: Distributions, with respect to their generated kinematic variables, of all the events that are reconstructed in the fifth ϕ bin of bin 5 (highlighted in red) for simulated DVCS and π^0 contamination events.

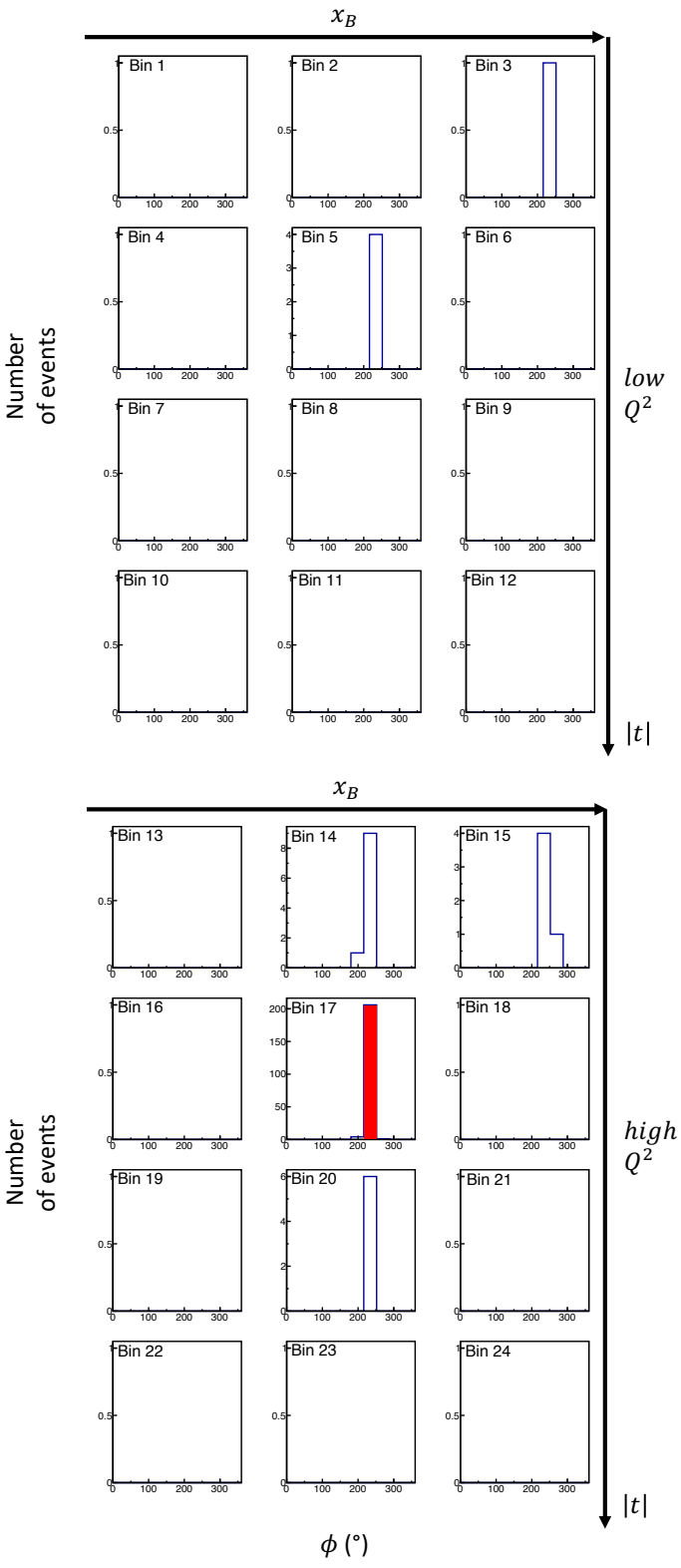

Figure A.14: Distribution, with respect to their generated kinematic variables, of all the events that are reconstructed in the seventh ϕ bin of bin 17 (highlighted in red) for simulated DVCS and π^0 contamination events.

A.6 BSA fit parameters

Bin	$< Q^2 >$	$< x_B >$	$< t >$	p_0	Δp_0	p_1	Δp_1
1	1.516	0.108	-0.115	0.263	0.018	0.056	0.134
2	1.997	0.194	-0.159	0.294	0.017	-0.122	0.126
3	2.418	0.317	-0.274	0.180	0.017	-0.546	0.111
4	1.529	0.113	-0.195	0.227	0.020	-0.143	0.126
5	2.035	0.193	-0.301	0.242	0.020	-0.441	0.111
6	2.494	0.342	-0.529	0.151	0.020	-0.715	0.099
7	1.529	0.118	-0.333	0.199	0.024	-0.339	0.136
8	1.974	0.194	-0.571	0.174	0.022	-0.469	0.151
9	2.484	0.334	-0.902	0.110	0.022	-0.701	0.148
10	1.514	0.119	-0.955	0.122	0.023	-0.402	0.205
11	1.868	0.206	-1.605	0.040	0.019	-0.779	0.169
12	2.461	0.323	-2.000	0.057	0.023	-0.756	0.234
13	2.031	0.137	-0.119	0.251	0.020	0.035	0.130
14	2.866	0.198	-0.165	0.272	0.016	0.005	0.121
15	4.227	0.338	-0.294	0.280	0.017	-0.094	0.119
16	2.033	0.140	-0.195	0.287	0.019	0.071	0.127
17	2.964	0.207	-0.300	0.271	0.016	-0.066	0.104
18	4.509	0.375	-0.538	0.261	0.019	-0.177	0.144
19	2.020	0.141	-0.329	0.216	0.021	-0.276	0.117
20	2.969	0.214	-0.551	0.257	0.019	-0.275	0.108
21	4.690	0.403	-0.894	0.236	0.025	-0.286	0.146
22	2.012	0.141	-0.912	0.156	0.023	-0.304	0.170
23	2.909	0.219	-1.501	0.094	0.021	-0.680	0.123
24	5.003	0.444	-2.215	0.157	0.027	-0.380	0.236

Table A.1: BSA fit parameters, fit parameters uncertainties and average kinematic variables for each kinematic bin (Q^2 and t are expressed in $\mathrm{GeV}^2/\mathrm{c}^4$).

Bibliography

[1] E. Rutherford. Collision of α particles with light atoms. IV. An anomalous effect in nitrogen. *Phil. Mag. Ser. 6*, 37:581–587, 1919. doi:10.1080/14786431003659230.

[2] E. Rutherford. The scattering of alpha and beta particles by matter and the structure of the atom. *Phil. Mag. Ser. 6*, 21:669–688, 1911. doi:10.1080/14786440508637080.

[3] R. Hofstadter, H. R. Fechter, and J. A. McIntyre. High-Energy Electron Scattering and Nuclear Structure Determinations. *Phys. Rev.*, 92(4):978, 1953. doi:10.1103/PhysRev.92.978.

[4] R. W. Mcallister and R. Hofstadter. Elastic Scattering of 188-{MeV} Electrons From the Proton and the α Particle. *Phys. Rev.*, 102:851–856, 1956. doi:10.1103/PhysRev.102.851.

[5] R. Hofstadter. Electron scattering and nuclear structure. *Rev. Mod. Phys.*, 28:214–254, 1956. doi:10.1103/RevModPhys.28.214.

[6] M. N. Rosenbluth. High Energy Elastic Scattering of Electrons on Protons. *Phys. Rev.*, 79:615–619, 1950. doi:10.1103/PhysRev.79.615.

[7] W. Xiong, A. Gasparian, H. Gao, et al. A small proton charge radius from an electron–proton scattering experiment. *Nature*, 575:147–150, 2019. doi:10.1038/s41586-019-1721-2.

[8] M. Burkardt. Impact parameter dependent parton distributions and off forward parton distributions for zeta —> 0. *Phys. Rev. D*, 62:071503, 2000, `arXiv:hep-ph/0005108`. doi:10.1103/PhysRevD.62.071503. [Erratum: Phys.Rev.D 66, 119903 (2002)].

[9] J. A. Rinehimer and G. A. Miller. Connecting the Breit Frame to the Infinite Momentum Light Front Frame: How G(E) turns into F(1). *Phys. Rev. C*, 80:015201, 2009, `arXiv:0902.4286 [nucl-th]`. doi:10.1103/PhysRevC.80.015201.

[10] E. D. Bloom et al. High-Energy Inelastic e p Scattering at 6-Degrees and 10-Degrees. *Phys. Rev. Lett.*, 23:930–934, 1969. doi:10.1103/PhysRevLett.23.930.

[11] M. Breidenbach, et al. Observed behavior of highly inelastic electron-proton scattering. *Phys. Rev. Lett.*, 23:935–939, 1969. doi:10.1103/PhysRevLett.23.935.

[12] J. D. Bjorken. Asymptotic Sum Rules at Infinite Momentum. *Phys. Rev.*, 179:1547–1553, 1969. doi:10.1103/PhysRev.179.1547.

[13] H. Abramowicz et al. Combination of measurements of inclusive deep inelastic $e^{\pm}p$ scattering cross sections and QCD analysis of HERA data. *Eur. Phys. J. C*, 75(12):580, 2015, arXiv:1506.06042 [hep-ex]. doi:10.1140/epjc/s10052-015-3710-4.

[14] C. G. Callan and D. J. Gross. Crucial Test of a Theory of Currents. *Phys. Rev. Lett.*, 21:311–313, 1968. doi:10.1103/PhysRevLett.21.311.

[15] R. P. Feynman. The behavior of hadron collisions at extreme energies. *Conf. Proc. C*, 690905:237–258, 1969.

[16] G. Altarelli and G. Parisi. Asymptotic Freedom in Parton Language. *Nucl. Phys. B*, 126:298–318, 1977. doi:10.1016/0550-3213(77)90384-4.

[17] V. N. Gribov and L. N. Lipatov. Deep inelastic e p scattering in perturbation theory. *Sov. J. Nucl. Phys.*, 15:438–450, 1972.

[18] Y. L. Dokshitzer. Calculation of the Structure Functions for Deep Inelastic Scattering and e+ e- Annihilation by Perturbation Theory in Quantum Chromodynamics. *Sov. Phys. JETP*, 46:641–653, 1977.

[19] G. Zweig. *An SU(3) model for strong interaction symmetry and its breaking. Version 2*, pages 22–101. 2 1964.

[20] M. Gell-Mann. A Schematic Model of Baryons and Mesons. *Phys. Lett.*, 8:214–215, 1964. doi:10.1016/S0031-9163(64)92001-3.

[21] E. P. Wigner. On the quantum correction for thermodynamic equilibrium. *Phys. Rev.*, 40:749–760, 1932. doi:10.1103/PhysRev.40.749.

[22] X.-d. Ji. Viewing the proton through 'color' filters. *Phys. Rev. Lett.*, 91:062001, 2003, arXiv:hep-ph/0304037. doi:10.1103/PhysRevLett.91.062001.

[23] A. V. Belitsky, X.-d. Ji, and F. Yuan. Quark imaging in the proton via quantum phase space distributions. *Phys. Rev. D*, 69:074014, 2004, arXiv:hep-ph/0307383. doi:10.1103/PhysRevD.69.074014.

[24] A. V. Belitsky and A. V. Radyushkin. Unraveling hadron structure with generalized parton distributions. *Phys. Rept.*, 418:1–387, 2005, arXiv:hep-ph/0504030. doi:10.1016/j.physrep.2005.06.002.

[25] S. Meissner, A. Metz, and M. Schlegel. Generalized parton correlation functions for a spin-1/2 hadron. *JHEP*, 08:056, 2009, arXiv:0906.5323 [hep-ph]. doi:10.1088/1126-6708/2009/08/056.

[26] G. P. Lepage and S. J. Brodsky. Exclusive Processes in Perturbative Quantum Chromodynamics. *Phys. Rev. D*, 22:2157, 1980. doi:10.1103/PhysRevD.22.2157.

[27] A. V. Efremov and A. V. Radyushkin. Factorization and Asymptotical Behavior of Pion Form-Factor in QCD. *Phys. Lett. B*, 94:245–250, 1980. doi:10.1016/0370-2693(80)90869-2.

[28] M. Diehl. Generalized parton distributions in impact parameter space. *Eur. Phys. J. C*, 25:223–232, 2002, arXiv:hep-ph/0205208. doi:10.1007/s10052-002-1016-9. [Erratum: Eur.Phys.J.C 31, 277–278 (2003)].

[29] X.-D. Ji. Gauge-Invariant Decomposition of Nucleon Spin. *Phys. Rev. Lett.*, 78:610–613, 1997, arXiv:hep-ph/9603249. doi:10.1103/PhysRevLett.78.610.

[30] X.-D. Ji. Deeply virtual Compton scattering. *Phys. Rev. D*, 55:7114–7125, 1997, arXiv:hep-ph/9609381. doi:10.1103/PhysRevD.55.7114.

[31] J. C. Collins and A. Freund. Proof of factorization for deeply virtual Compton scattering in QCD. *Phys. Rev. D*, 59:074009, 1999, arXiv:hep-ph/9801262. doi:10.1103/PhysRevD.59.074009.

[32] A. Bacchetta, U. D'Alesio, M. Diehl, and C. A. Miller. Single-spin asymmetries: The Trento conventions. *Phys. Rev. D*, 70:117504, 2004, arXiv:hep-ph/0410050. doi:10.1103/PhysRevD.70.117504.

[33] A. V. Belitsky, D. Mueller, and A. Kirchner. Theory of deeply virtual Compton scattering on the nucleon. *Nucl. Phys. B*, 629:323–392, 2002, arXiv:hep-ph/0112108. doi:10.1016/S0550-3213(02)00144-X.

[34] N. d'Hose, S. Niccolai, and A. Rostomyan. Experimental overview of Deeply Virtual Compton Scattering. *Eur. Phys. J. A*, 52(6):151, 2016. doi:10.1140/epja/i2016-16151-9.

[35] L. Favart, M. Guidal, T. Horn, and P. Kroll. Deeply Virtual Meson Production on the nucleon. *Eur. Phys. J. A*, 52(6):158, 2016, arXiv:1511.04535 [hep-ph]. doi:10.1140/epja/i2016-16158-2.

[36] A. Accardi et al. Electron Ion Collider: The Next QCD Frontier: Understanding the glue that binds us all. *Eur. Phys. J. A*, 52(9):268, 2016, arXiv:1212.1701 [nucl-ex]. doi:10.1140/epja/i2016-16268-9.

[37] S. Chekanov et al. Measurement of deeply virtual Compton scattering at HERA. *Phys. Lett. B*, 573:46–62, 2003, arXiv:hep-ex/0305028. doi:10.1016/j.physletb.2003.08.048.

[38] A. Aktas et al. Measurement of deeply virtual compton scattering at HERA. *Eur. Phys. J. C*, 44:1–11, 2005, arXiv:hep-ex/0505061. doi:10.1140/epjc/s2005-02345-3.

[39] F. D. Aaron et al. Deeply Virtual Compton Scattering and its Beam Charge Asymmetry in e+- Collisions at HERA. *Phys. Lett. B*, 681:391–399, 2009, arXiv:0907.5289 [hep-ex]. doi:10.1016/j.physletb.2009.10.035.

[40] A. Airapetian et al. Beam-helicity asymmetry arising from deeply virtual Compton scattering measured with kinematically complete event reconstruction. *JHEP*, 10:042, 2012, arXiv:1206.5683 [hep-ex]. doi:10.1007/JHEP10(2012)042.

[41] A. Ferrero. GPD physics with polarized muon beams at COMPASS-II. *AIP Conf. Proc.*, 1523(1):75–78, 2013, arXiv:2001.02594 [hep-ex]. doi:10.1063/1.4802120.

[42] F. X. Girod et al. Measurement of Deeply virtual Compton scattering beam-spin asymmetries. *Phys. Rev. Lett.*, 100:162002, 2008, arXiv:0711.4805 [hep-ex]. doi:10.1103/PhysRevLett.100.162002.

[43] G. Gavalian et al. Beam spin asymmetries in deeply virtual Compton scattering (DVCS) with CLAS at 4.8 GeV. *Phys. Rev. C*, 80:035206, 2009, arXiv:0812.2950 [hep-ex]. doi:10.1103/PhysRevC.80.035206.

[44] E. Seder et al. Longitudinal target-spin asymmetries for deeply virtual Compton scattering. *Phys. Rev. Lett.*, 114(3):032001, 2015, arXiv:1410.6615 [hep-ex]. doi:10.1103/PhysRevLett.114.032001. [Addendum: Phys.Rev.Lett. 114, 089901 (2015)].

[45] H. S. Jo et al. Cross sections for the exclusive photon electroproduction on the proton and Generalized Parton Distributions. *Phys. Rev. Lett.*, 115(21):212003, 2015, arXiv:1504.02009 [hep-ex]. doi:10.1103/PhysRevLett.115.212003.

[46] S. Pisano et al. Single and double spin asymmetries for deeply virtual Compton scattering measured with CLAS and a longitudinally polarized proton target. *Phys. Rev. D*, 91(5):052014, 2015, arXiv:1501.07052 [hep-ex]. doi:10.1103/PhysRevD.91.052014.

[47] M. Defurne et al. E00-110 experiment at Jefferson Lab Hall A: Deeply virtual Compton scattering off the proton at 6 GeV. *Phys. Rev. C*, 92(5):055202, 2015, arXiv:1504.05453 [nucl-ex]. doi:10.1103/PhysRevC.92.055202.

[48] M. Defurne, A. Jiménez-Argüello, Z. Ahmed, and al. A glimpse of gluons through deeply virtual compton scattering on the proton. *Nat Commun*, 8:1408, 2017. doi:10.1038/s41467-017-01819-3.

[49] A. Afanasev et al. Physics with Positron Beams at Jefferson Lab 12 GeV. 6 2019, arXiv:1906.09419 [nucl-ex].

[50] V. D. Burkert. Jefferson Lab at 12 GeV: The Science Program. *Ann. Rev. Nucl. Part. Sci.*, 68:405–428, 2018. doi:10.1146/annurev-nucl-101917-021129.

[51] L. S. Cardman and L. Harwood. The JLab 12-GeV Energy Upgrade of CEBAF for QCD and Hadronic Physics. pages 58–62, 2007. doi:10.1109/PAC.2007.4440339.

[52] R. Kazimi, et al. Four Beam Generation for Simultaneous Four-Hall Operation at CEBAF. In *7th International Particle Accelerator Conference*, page THPOY060, 2016. doi:10.18429/JACoW-IPAC2016-THPOY060.

[53] P. A. Adderley, et al. Load-locked dc high voltage GaAs photogun with an inverted-geometry ceramic insulator. *Phys. Rev. ST Accel. Beams*, 13:010101, 2010. doi:10.1103/PhysRevSTAB.13.010101.

[54] Y. Wang, A. Hofler, and R. Kazimi. Commissioning of the 123 MeV Injector for 12 GeV CEBAF. In *6th International Particle Accelerator Conference*, page TUPMA037, 2015. doi:10.18429/JACoW-IPAC2015-TUPMA037.

[55] V. D. Burkert et al. The CLAS12 Spectrometer at Jefferson Laboratory. *Nucl. Instrum. Meth. A*, 959:163419, 2020. doi:10.1016/j.nima.2020.163419.

[56] N. Baltzell et al. The CLAS12 beamline and its performance. *Nucl. Instrum. Meth. A*, 959:163421, 2020. doi:10.1016/j.nima.2020.163421.

[57] M. McCaughan, M. Tiefenback, and D. Turner. Improvements to Existing Jefferson Lab Wire Scanners. In *4th International Particle Accelerator Conference*, page MOPWA076, 2013.

[58] R. Ursic, M. Piller, R. Flood, E. Strong, and L. Turlington. 1 nA Beam Position Monitoring System. *Conf. Proc. C*, 970512:2131, 1997.

[59] B. A. Mecking et al. The CEBAF Large Acceptance Spectrometer (CLAS). *Nucl. Instrum. Meth. A*, 503:513–553, 2003. doi:10.1016/S0168-9002(03)01001-5.

[60] M. A. Antonioli et al. The CLAS12 Silicon Vertex Tracker. *Nucl. Instrum. Meth. A*, 962:163701, 2020. doi:10.1016/j.nima.2020.163701.

[61] A. Acker et al. The CLAS12 Micromegas Vertex Tracker. *Nucl. Instrum. Meth. A*, 957:163423, 2020. doi:10.1016/j.nima.2020.163423.

[62] D. S. Carman, et al. The CLAS12 Central Time-of-Flight system. *Nucl. Instrum. Meth. A*, 960:163626, 2020. doi:10.1016/j.nima.2020.163626.

[63] P. Chatagnon et al. The CLAS12 Central Neutron Detector. *Nucl. Instrum. Meth. A*, 959:163441, 2020. doi:10.1016/j.nima.2020.163441.

[64] M. D. Mestayer et al. The CLAS12 drift chamber system. *Nucl. Instrum. Meth. A*, 959:163518, 2020. doi:10.1016/j.nima.2020.163518.

[65] Y. G. Sharabian et al. The CLAS12 high threshold Cherenkov counter. *Nucl. Instrum. Meth. A*, 968:163824, 2020. doi:10.1016/j.nima.2020.163824.

[66] M. Ungaro et al. The CLAS12 Low Threshold Cherenkov detector. *Nucl. Instrum. Meth. A*, 957:163420, 2020. doi:10.1016/j.nima.2020.163420.

[67] D. S. Carman et al. The CLAS12 Forward Time-of-Flight system. *Nucl. Instrum. Meth. A*, 960:163629, 2020. doi:10.1016/j.nima.2020.163629.

[68] G. Asryan et al. The CLAS12 forward electromagnetic calorimeter. *Nucl. Instrum. Meth. A*, 959:163425, 2020. doi:10.1016/j.nima.2020.163425.

[69] A. Acker et al. The CLAS12 Forward Tagger. *Nucl. Instrum. Meth. A*, 959:163475, 2020. doi:10.1016/j.nima.2020.163475.

[70] B. Raydo, et al. The CLAS12 Trigger System. *Nucl. Instrum. Meth. A*, 960:163529, 2020. doi:10.1016/j.nima.2020.163529.

[71] V. Ziegler et al. The CLAS12 software framework and event reconstruction. *Nucl. Instrum. Meth. A*, 959:163472, 2020. doi:10.1016/j.nima.2020.163472.

[72] S. Agostinelli et al. GEANT4–a simulation toolkit. *Nucl. Instrum. Meth. A*, 506:250–303, 2003. doi:10.1016/S0168-9002(03)01368-8.

[73] Y. Giomataris, P. Rebourgeard, J. P. Robert, and G. Charpak. MICROMEGAS: A High granularity position sensitive gaseous detector for high particle flux environments. *Nucl. Instrum. Meth. A*, 376:29–35, 1996. doi:10.1016/0168-9002(96)00175-1.

[74] I. Giomataris, et al. Micromegas in a bulk. *Nucl. Instrum. Meth. A*, 560:405–408, 2006, `arXiv:physics/0501003`. doi:10.1016/j.nima.2005.12.222.

[75] T. Alexopoulos, et al. A spark-resistant bulk-micromegas chamber for high-rate applications. *Nucl. Instrum. Meth. A*, 640:110–118, 2011. doi:10.1016/j.nima.2011.03.025.

[76] B. Stelzer. The New Small Wheel Upgrade Project of the ATLAS Experiment. *Nucl. Part. Phys. Proc.*, 273-275:1160–1165, 2016. doi:10.1016/j.nuclphysbps.2015.09.182.

[77] N. Metropolis, A. W. Rosenbluth, M. N. Rosenbluth, A. H. Teller, and E. Teller. Equation of state calculations by fast computing machines. *J. Chem. Phys.*, 21:1087–1092, 1953. doi:10.1063/1.1699114.

[78] W. K. Hastings. Monte Carlo Sampling Methods Using Markov Chains and Their Applications. *Biometrika*, 57:97–109, 1970. doi:10.1093/biomet/57.1.97.

[79] V. D. Burkert, L. Elouadrhiri, and F. X. Girod. The pressure distribution inside the proton. *Nature*, 557(7705):396–399, 2018. doi:10.1038/s41586-018-0060-z.

[80] N. Cherrier, J. Poli, M. Defurne, and F. Sabatié. Consistent feature construction with constrained genetic programming for experimental physics. In *2019 IEEE Congress on Evolutionary Computation (CEC)*, pages 1650–1658, 2019. doi:10.1109/CEC.2019.8789937.

[81] N. Cherrier, M. Mayo, J.-P. Poli, M. Defurne, and F. Sabatié. Interpretable machine learning with bitonic generalized additive models and automatic feature construction. In A. Appice, G. Tsoumakas, Y. Manolopoulos, and S. Matwin, editors, *Discovery Science*, pages 386–402, Cham, 2020. Springer International Publishing. doi:10.1007/978-3-030-61527-$7_2$6.

[82] B. Berthou et al. PARTONS: PARtonic Tomography Of Nucleon Software: A computing framework for the phenomenology of Generalized Parton Distributions. *Eur. Phys. J. C*, 78(6):478, 2018, `arXiv:1512.06174 [hep-ph]`. doi:10.1140/epjc/s10052-018-5948-0.

[83] W. Commons. File:photomultipliertubeandscintillator.svg — wikimedia commons, the free media repository, 2020. url `https://commons.wikimedia.org/w/index.php?title=File:PhotoMultiplierTubeAndScintillator.svg&oldid=512910876`. [Online; accessed 25-February-2021].